Steady-state, Simultaneous Two-phase Flow in Porous Media

Ken Tore Tallakstad

Acknowledgements

After two years as a master student at the Complex group, I would like to take this opportunity and thank some of the people that have made these years enjoyable.

First and foremost I want to thank my supervisor prof. Knut Jørgen Måløy for accepting me as a student and for all his comments and suggestions during this project. His philosophy on allowing students to encounter real research instead of reviewing established results, has been greatly appreciated.

Grunde Løvoll deserves thanks for all his help along the way. I am truly impressed by his skills as an experimental physicist. Our common interest in fly-fishing, the only proper way, has led to colloquiums also outside the lab.

I want to thank Henning Arendt Knudsen for his eagerness to discuss the many physical problems I encountered and for explaining to me the basics of flow in porous media. His proofreading has also been valuable.

My good friend and fellow student Marius Lysebo deserves thanks for all the hours he put into proofreading this thesis. I have been fortunate with having his help on physical issues over the last five years.

Last but not least: Olav, Mihailo, Stephane, Michael, Øystein, Jan Ludvig and all the other guys deserve thanks for creating such a good environment.

Besides physics I would like to mention the coffee machine in the lunchroom, Andreas Lie and our common friend Leif Kempke.

Ken Tore Tallakstad
Blindern, July 2007

Contents

Chapter 1

Introduction

One method of extracting oil from undersea reservoirs is to pump it out with seawater. In the petroleum industry this is achieved through injection wells, where water is pumped into the reservoir, and production wells where the oil is pumped up to sealevel. The amount of oil extracted depends, among other things, on the rate at which water is pumped. It is of great economical importance to extract as much oil as possible, and surprising that we are not able to recover more than roughly 40%. Why is this percentage so low? It has to do with the complex geometry inside the reservoir. Flowing seawater and oil behave very differently in a reservoir than in an ordinary pipeline. To increase the amount of recovered oil, petroleum engineering are on the constant search for new and improved methods. This can only be achieved by considering the physics of the processes inside the reservoirs.

The special field of physics that deals with these topics is called flow in porous media and it is part of a broader field known as complex systems. Apart from oil recovery, the study of flow in porous media is important also in other fields of science and engineering. Examples are hydrology, soil sciences, biomedical- and agricultural engineering. In particular, two-phase displacements in porous porous media have been studied frequently over the last decades. The main reason is the great variety of structures observed when changing fluid parameters like viscosity, surface tension, displacement rate and wettability. To understand how these structures form and develop, may have direct implications for the oil industry.

At the Complex group there is a long standing tradition for both experimental and numerical work in this field [1, 3] [29] [43] [45]. Experimentally, flow of multiple phases are studied in model porous media. The most common model used is a one-layer porous stratum made by distributing small glass beads randomly between transparent plates. The randomness creates an environment similar to that of real porous media, with pores and throats of varying size. These quasi two-dimensional models are mainly used due to the good transparency, and hence the possibility to visually observe the displacement structures. It is quite often found, that results obtained in two-dimensions can be generalized to higher dimensions.

Traditionally, experiments or simulations are devised so that one fluid is used to displace a second fluid, hence the terms invading and defending fluid. The resulting classical regimes from this kind of displacement have been studied by several authors independently, and are considered well understood. As an extension of previous studies, the main focus of this project has been to perform experiments where two phases are injected into a porous medium simultaneously. These boundary conditions should also be more similar to what happens deep inside an oil reservoir, and thus take the analogy to real reservoir flow a step further. We have mainly focused on the steady-state regime of the experiments. We attempt to answer new questions in a field little explored. Simultaneous two-phase flow is nothing new, it is commonly used to measure relative permeabilities. However, large three dimensional core samples are often used, and the experiments does not seek to address the underlaying physics of the complex structures inside. Some numerical work considering steady-state flow have been carried out [8] [25] [38], but very few experimental studies can be found [17] [18]. More precise we seek to answer how

pressure and fluid flow relate to dynamics and observed structures. Both the transient and steady regime have been considered in a large quasi two-dimensional laboratory model.

This thesis is organized as follows. Chapter 2 introduces the basic geometrical and physical parameters of multi-phase flow in porous media. We then consider the equations describing such flows. A review of the classical regimes is provided, before the main topic of simultaneous flow is discussed towards the end.

In Chapter 3 we turn to a description of the experimental setup and how the experiments were conducted. Instrumentation has been an important part of this project, and is also reviewed. At the end we discuss how to extract relevant properties from raw images.

Our experimental findings are presented and discussed in Chapter 4. Appendix A includes some theory on probability distributions, and the Matlab scripts used for image analysis and simulations are listed in Appendix B.

Chapter 2

Multi-phase flow in porous media
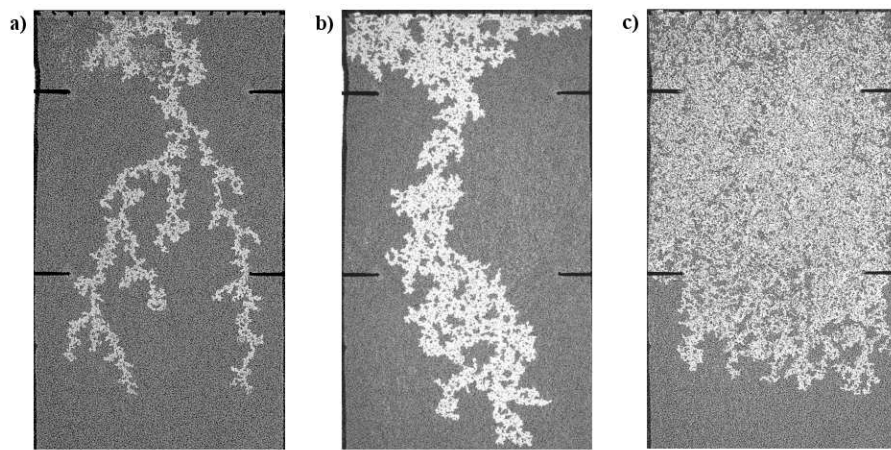
Figure 2.1: *Three experimental images of multi-phase flow in two-dimensional porous media. The flow direction is from top to bottom, and air (white) displaces a water/glycerol mixture (black) in all cases. In* **a)** *air is injected at a high flow-rate. In* **b)** *air is injected at an intermediate flow-rate. In* **c)** *both air and glycerol/water are injected simultaneously.*

The oil reservoir described in the introduction is an example of a porous medium. When fluids flow in such media, a great diversity of structures are displayed due to the complex geometry. Three different flow structures from laboratory experiments are shown in figure 2.1. In this chapter we will discuss the underlaying physics of these systems.

2.1   Basic parameters

This section is meant as a brief introduction to those unfamiliar with flow in porous media. First, basic concepts of the porous media itself are given, before the properties of fluids are discussed. Those familiar with fluid mechanics and porous media can omit this section without loss of continuity.

3

2.1.1 Porous media

A real porous medium is a solid permeated by interconnected voids of various sizes. The voids are called *pores*, and the pore network constitutes what is called the *pore space*. Typical examples of real porous media are: sandstone, limestone, cement, sponge and so on. A characteristic property of porous media is the *porosity φ*, defined as:

$$\phi = \frac{\text{Volume of pore space}}{\text{Total sample volume}}, \quad \text{where} \quad \phi \in [0,1] \tag{2.1}$$

Typical porosities in oil production are in the range of $(0.05, 0.4)$, [16]. It is important to note that the porosity has to be averaged over many pores for a given sample, and the considered volume must be larger than the size of one pore.

In oil recovery, the porous medium is the embedding geometry in which different flow processes take place. When a sample is saturated with flowing oil, we have a so called *one-phase flow* through the medium. If e.g a gas is displacing oil, the process is called *two-phase-* or *multi-phase flow*. Different flow processes in porous media have been studied from the early 19th century, and are still of interest. To study flow in porous media experimentally, simplified artificial models are made. In this thesis we use a monolayer of glass beads randomly distributed between two parallel plates. This model is an example of a porous Hele-Shaw cell. A regular Hele-Shaw cell consists of two parallel plates, separated by a small distance. Due to the small separation of the plates, a Hele-Shaw cell is considered to be a quasi two-dimensional medium. Different network models etched in glass, [17, 18], are other examples of model porous media.

Figure 2.2 shows a fluid displacement process in a small version of our porous medium. Fluid
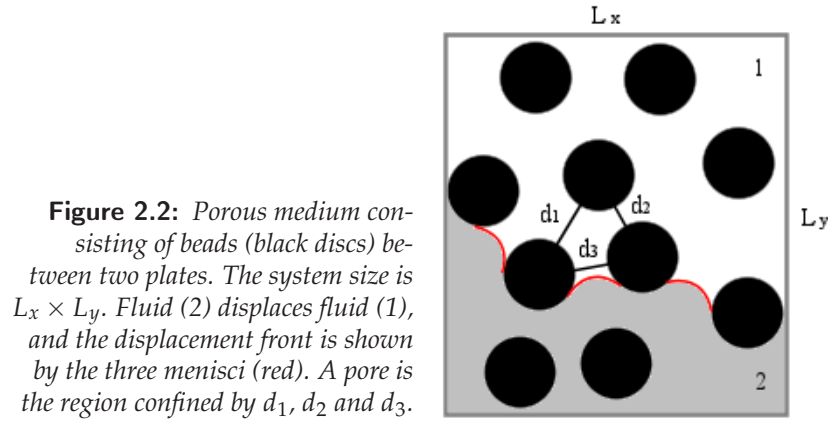
Figure 2.2: *Porous medium consisting of beads (black discs) between two plates. The system size is $L_x \times L_y$. Fluid (2) displaces fluid (1), and the displacement front is shown by the three menisci (red). A pore is the region confined by d_1, d_2 and d_3.*

2 displaces fluid 1, and the *displacement front* consists of the three menisci. The region confined by d_1, d_2 and d_3 is called a *pore*. The thinner channels characterized by the lengths d_1, d_2 and d_3 are called *pore-throats*, and they play an important role for the displacement structure. It is customary to introduce the saturation of the fluids present in the porous medium:

$$S_1 = \frac{V_1}{V\phi} \tag{2.2}$$

$$S_2 = \frac{V_2}{V\phi} \tag{2.3}$$

where V is the total sample volume. V_1 and V_2 are the volume of fluid 1 and 2 respectively. From eq. 2.2 and 2.3 it follows that,

$$S_1 + S_2 = 1, \tag{2.4}$$

meaning that the sum of fluid volumes always equals the pore space volume.

We see that the beads in figure 2.2 are placed randomly. Randomness is important in the study of porous media, and is almost always present in real systems. If we measure, for all of the beads, the distance from the center to all of its neighbors centers (d_1, d_2, d_3, ..., d_N), and take double counting into account, we get the *pore-throat distribution*. The randomness of the porous medium is reflected in this distribution. For a single layer of mono-disperse beads packed regularly, the pore throat distribution equals the delta function. If the packing is such that the distribution is flat between an upper and a lower limit, the randomness is at a maximum. Both the delta function and the flat distribution are of course limiting cases, and normally the distribution is found somewhere in between.

In addition to porosity, the *permeability K*, is a geometrical property of the porous medium. It describes a fluids ability to flow through the porous medium. The permeability is analog to the conductance in electrical circuits. A high value makes it easier to flow and vice versa. When dealing with multi-phase flow the parameter K is called the *absolute - or one-phase permeability*. Permeability in multi-phase flow will be considered in section 2.2.3. A commonly used unit of permeability is *darcy*, after Henry Darcy, where 1 darcy $= 9.87 \cdot 10^{-9}$ cm^2 $\simeq 1 (\mu m)^2$.

In porous media there are two important length scales. First we have the microscopic or the *pore scale*. The length of a "measuring stick" at the pore scale, is set by the typical size of a pore in the sample. As an example, a typical pore length in our porous medium is 1 mm. The second length scale is the *macroscopic scale*, where a "measuring stick" typically is at the length of the sample. In our case the system size is of the order ~ 1 m.

2.1.2 Viscosity

Viscosity is a fluid property, and can be viewed as a measure of the resistance to flow. As an example, it is easier to squeeze water through a capillary tube than oil, hence water has the lowest viscosity. When it comes to flow in porous media, the viscosity is an essential parameter, as will become apparent. Since viscosity is a topic in almost every book of fluid mechanics, e.g [14], only a brief quantitative treatment will be given. Consider two large parallel plates separated by a
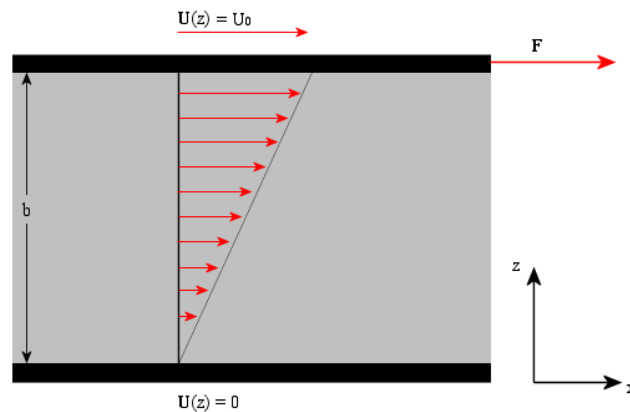
Figure 2.3: *A force **F** is applied to the upper plate, which moves at a constant speed U_0. The bottom plate is fixed. The arrows indicate the linear velocity gradient in the z-direction. It can be shown that the shearing stress caused by **F** is proportional to the fluid velocity gradient. This proportionality constant is called the viscosity of the fluid.*

.

fluid layer, as shown in figure 2.3. The bottom plate is fixed, whereas a force **F** is applied to the top plate which moves at a constant speed U_0. This is an example of laminar flow, meaning that the fluid moves in infinitesimal layers with different velocities. The fluid velocity is 0 and U_0 close to the lower and upper plate respectively. When the fluid has the same speed as its solid

boundaries, we have so called *no-slip boundary conditions*. Experimentally, the fluid velocity in this case is found to vary linearly in the z direction:

$$U(z) = \frac{U_0}{b}z, \tag{2.5}$$

$$|\nabla U| = \frac{U_0}{b}. \tag{2.6}$$

It can be shown [14] that the shearing stress τ is proportional to the velocity gradient,

$$\tau = \frac{F}{A} \propto |\nabla U| \tag{2.7}$$

$$\tau = \mu|\nabla U|, \tag{2.8}$$

where A is the area of the plate and μ is called the *dynamic viscosity*, or just the viscosity of the fluid. Viscosity has units of $Ns/m^2 = Pa\ s = 10^{-3}cP$, where P is the *cgs* unit Poise. We also need to introduce the *kinematic viscosity*,

$$\nu = \frac{\mu}{\rho} \tag{2.9}$$

where ρ is the density of the fluid. Fluids where the proportionality of eq. 2.7 holds are designated as *Newtonian fluids*. Otherwise the fluids are called *non-Newtonian*, and are in general much more complex. Fortunately most of our common fluids are Newtonian. The viscosity parameter is also highly dependent upon temperature, as shown in figure 3.9.

In a two phase flow system, the viscosity of the fluids are important and it is customary to define a *viscosity ratio*:

$$M = \frac{\mu_{nw}}{\mu_w}, \tag{2.10}$$

where the subscripts nw and w describes a non-wetting and wetting fluid respectively. The concept of wetting will be discussed in section 2.1.4.

2.1.3 Surface tension

The reason why a needle can float on a water surface, can not be explained by Archimedes' law of buoyancy. The forces keeping the needle afloat is due to a fundamental property between fluid interfaces, called the surface or interfacial tension. To understand the origin of these forces we must look at the molecular level of the surface. Without going into too much detail, the basic principles are the following. Between identical molecules in the bulk of one fluid there exist attraction forces, or so called *cohesive* forces. Near the surface, e.g. in an oil droplet embedded in water, there are also weaker forces between water and oil molecules, called *adhesive* forces. A fundamental property of any system, in this case the oil droplet, is to reduce the free energy as much as possible while maximizing the entropy. The adhesive forces contributes less to reducing potential energy than the cohesive ones, and it is thus favorable for the oil droplet to minimize its surface. The geometrical shape of the droplet in equilibrium is spherical, since this gives the largest volume pr. surface ratio.

Since the surface of the droplet in equilibrium has its smallest value, work must be done to increase the surface (i.e. move molecules from the bulk to the surface). Surface tension can then be defined as the amount of work needed pr. unit surface increase,

$$\gamma = \frac{dW}{dA}. \tag{2.11}$$

When work is done, the process is assumed to be isothermal, since any temperature variations can affect fluid properties. Unit analysis of eq. 2.11 gives [*N/m*] or [*J/m^2*], hence surface tension

can be viewed as either force pr. unit length or energy pr. unit area. In the former view, the force pr. unit length is always tangential to the interface. A high value of the surface tension means that a large force must be applied to increase the surface. Since a needle can float on water, the surface tension must be high enough to oppose its weight. If detergent is added to the water, the surface tension decreases and the needle sinks instantly.

The existence of surface tension gives rise to a condition for mechanical equilibrium of a surface between two fluids. This condition is called the *Young-Laplace* equation and we will derive it here, following [13]. It is of considerable importance in the physics of multi-phase flow in porous media.

Consider a point N on the cap of a smooth surface between two fluids, as shown in figure 2.4. The distance along the boundary of the cap to N is called ρ, and is constant. We want to find the condition for equilibrium as ρ tends to zero.
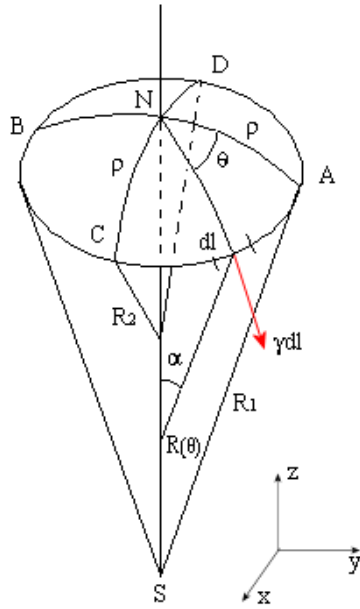
Figure 2.4: *The cap of a fluid-fluid interface. The boundary goes through the points A, B, C and D. Every point along the boundary is a distance ρ from the center point N. Two arbitrary orthogonal lines, AB and CD, is drawn with principal radii of curvature R_1 and R_2 respectively. The force, due to surface tension γ, that acts on a small element dl of the boundary is also indicated. The radius of curvature at dl is $R(\theta)$.*

In figure 2.4 two orthogonal lines have been drawn from A to B and from C to D, with principal radii of curvature R_1 and R_2 respectively. From eq.2.11 it follows that an element dl at an arbitrary position along the boundary of the cap is subjected to an infinitesimal force $dF = \gamma dl$. In the xy-plane, equilibrium is always obtained, whereas in the z-direction, the projection of dF parallel to NS, dF_z, must be considered:

$$dF_z = \sin \alpha \gamma dl = \alpha \gamma dl = \frac{\rho}{R(\theta)} \gamma dl, \tag{2.12}$$

where $R(\theta)$ is the radius of curvature at an angle θ from A. The equality holds because α becomes very small as ρ approaches zero. Eulers curvature formula states that:

$$\frac{1}{R(\theta)} = \frac{\cos^2 \theta}{R_1} + \frac{\sin^2 \theta}{R_2}, \tag{2.13}$$

which gives upon insertion in eq. 2.12,

$$dF_z = \rho \gamma \left(\frac{\cos^2 \theta}{R_1} + \frac{\sin^2 \theta}{R_2} \right) dl \tag{2.14}$$

The total force can be found by integrating around the circumference:

$$F_z = \int dF_z = \rho^2 \gamma \int_0^{2\pi} \left(\frac{\cos^2 \theta}{R_1} + \frac{\sin^2 \theta}{R_2} \right) d\theta, \tag{2.15}$$

where dl has been replaced with $\rho d\theta$. Integration yields,

$$F_z = \pi \rho^2 \gamma \left(\frac{1}{R_1} + \frac{1}{R_2} \right) \tag{2.16}$$

To obtain mechanical equilibrium in the z-direction, the pressure forces inside P_1 and outside P_0 of the fluid interface, must be balanced by eq. 2.16,

$$(P_1 - P_0)\pi\rho^2 = \pi\rho^2\gamma \left(\frac{1}{R_1} + \frac{1}{R_2} \right) \tag{2.17}$$

$$P_1 - P_0 = \gamma \left(\frac{1}{R_1} + \frac{1}{R_2} \right). \tag{2.18}$$

Eq. 2.18 is the Young-Laplace equation. It states that for a finite surface tension, there must be a pressure difference between a curved fluid interface, to obtain mechanical equilibrium.

2.1.4 Wetting

When a droplet is placed on a smooth plane surface, it can take various shapes, depending on the contact properties between the fluid and the surface. Two realizations are shown in figure 2.5. A gas is assumed to surround the droplet and the surface. The angle θ indicated in the figure is called the *contact-angle*[1].

Figure 2.5: a) *A non-wetting droplet placed on a plane solid surface. The solid and fluid are surrounded by wetting gas. The contact angle $\theta > 90°$.* **b)** *Same as in a), but the droplet of fluid now wets the solid. Also included are the surface tension vectors between the different phases, drawn from one of the contact points. $\theta < 90°$*

.

The term *wetting* is used to describe this contact angle:

$$0° < \theta < 90° \quad \Rightarrow \quad wetting$$
$$90° < \theta < 180° \quad \Rightarrow \quad non\text{-}wetting$$

The angle θ refers to the fluid inside the droplet. A wetting droplet implies a non-wetting surrounding gas. The droplet will have a tendency to "smear" out on the surface. In the other case, when the droplet is non-wetting, the gas smears out and the droplet tries to minimize its contact

---

[1]In the literature, the angle $\theta' = \pi - \theta$ is also frequently used as the contact angle, but this is just a matter of definition.

with the solid surface. Also drawn in figure 2.5 b) are the surface tension vectors at the gas/fluid/solid contact point. Equilibrium along the solid surface plane gives the following relation:

$$\gamma_{f,g} \cos \theta = \gamma_{s,g} - \gamma_{f,s} \tag{2.19}$$

$$\cos \theta = \frac{\gamma_{s,g} - \gamma_{f,s}}{\gamma_{f,g}}, \tag{2.20}$$

where subscripts f, g, s denotes fluid, gas and solid respectively. From eq. 2.20 it is clear that the wetting properties depends on the system at hand. Thus when θ is given for some fluid, it should also be made clear which gas and solid that are involved.

When $\theta = 90°$, we have the special case of *mixed wetting* conditions between the fluid and gas. From eq. 2.20, it follows that mixed wetting means equal surface tension between fluid/solid and gas/solid. When $\theta = 0°$, the fluid is said to be *perfect wetting*. The full range of the contact angle for a wetting fluid is summarized in figure 2.6. This is the "classical" situation encountered when a wetting fluid tries to displace a non-wetting fluid through a pore-throat. All
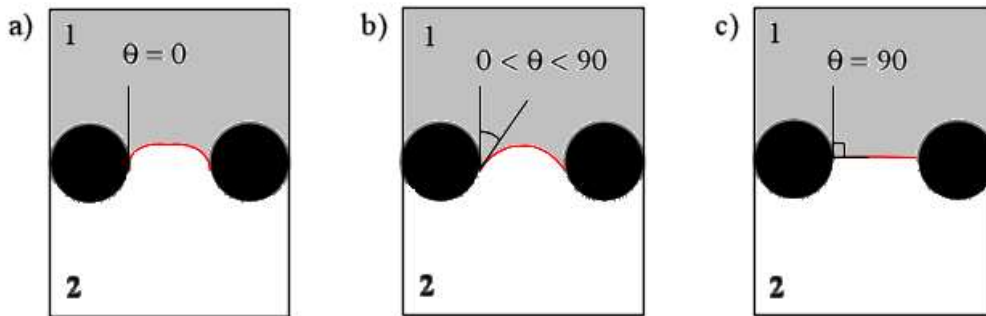

Figure 2.6: *A fluid (1) and gas (2) confined in a box between two solid beads. The red line indicates the meniscus between the phases. **a)** Perfect wetting, **b)** Normal wetting and **c)** Mixed wetting.*

of the above considerations were done for a gas/fluid/solid system, but applies equally well for a fluid/fluid/solid system.

In figure 2.5 e.g the system is static, hence the term *static contact angle* has been introduced. When two fluids displace each other in a porous media, the process is not static and a *dynamic contact angle* has been introduced. The dynamic contact angle differs from the static one and is also related to what is called *contact angle hysteresis*. It is found that the advancing angle, i.e the contact angle measured through the fluid that is displacing another fluid, is sometimes found to be different than the receding one (the receding angel being the angle measured through the same fluid when it is being displaced). Three explanations have been suggested for this hysteresis effect [15]. The first is contamination of either the fluid or solid. Second, surface roughness and third; surface immobility at a macromolecular scale. Due to the difference between static and dynamic contact angles, the wetting properties in a flow system can differ from eq. 2.20. However, measuring of the dynamic contact angle can be a tedious process, [13].

Wetting properties during two phase flow in porous media are of importance. Changing of these parameters can alter the displacement structure. We will return to this discussion later on.

2.2   Flow equations in porous media

In this section we look at the equations that govern flow in porous media. First the capillary pressure is introduced, and we look at the effect of the Young-Laplace equation. On the pore- and macroscopic scale, we introduce the Navier-Stokes equations and Darcy's law respectively. A discussion of fluid compressibility is presented towards the end.

2.2.1   Capillary pressure

The *capillary* pressure, P_{cap}, is defined as

$$P_{\text{cap}} = P_{nw} - P_w. \tag{2.21}$$

It gives the pressure difference over the non-wetting/wetting fluid interface. When neglecting gravity forces, the condition for mechanical equilibrium is given by the Young-Laplace equation (eq. 2.18),

$$P_{\text{cap}} = \gamma \left(\frac{1}{R_1} + \frac{1}{R_2} \right). \tag{2.22}$$

To move a meniscus into a narrower part of a pore-throat, one can either increase the non-wetting pressure or decrease the wetting pressure in eq. 2.21. From eq. 2.22 it then follows that the increase in capillary pressure must be accompanied by an increase in curvature. In this manner, the curvature of the interface is linked to its position in the pore-throat. A threshold or critical value of the capillary pressure P_c is associated with the narrowest part of the pore throat. Whenever P_{cap} exceeds P_c the meniscus becomes unstable, because the geometry of the pore-throat can no longer uphold mechanical equilibrium at this point. The instability of the meniscus causes it to spontaneously invade the pore in front. Hence the criterion for pore invasion is given by

$$P_{\text{cap}} > P_c. \tag{2.23}$$

Each pore-throat i in a porous medium has a critical capillary pressure $P_{c,i}$ associated with it. The distribution of pressure thresholds $N(P_c)$, plays a significant role when considering two phase flow in porous media. We discuss this further, when we describe different flow regimes.

2.2.2   Differential equations at the pore scale

The general approach to a complex problem, is to break it down and solve the smaller and simpler bits. The solution of the whole system is then found from the solution of one simple bit. In theory it is possible to start at the pore scale and integrate the Navier-Stokes equation [19] over the medium. We emphasize that this is only in theory. For incompressible Newtonian fluids, the Navier-Stokes equation reads

$$\rho \frac{\partial \mathbf{u}}{\partial t} + \rho \mathbf{u} \cdot \nabla \mathbf{u} = -\nabla P + \mu \nabla^2 \mathbf{u} + \rho \mathbf{g}, \tag{2.24}$$

where ρ is fluid density, μ viscosity, $\mathbf{u}(\mathbf{x}, t)$ is the fluid velocity field, $P(\mathbf{x}, t)$ is the pressure field and $\mathbf{g}$ the acceleration of gravity. The continuity equation is given by,

$$\frac{\partial \rho}{\partial t} + \nabla \cdot \rho \mathbf{u} = 0, \tag{2.25}$$

and expresses that mass is conserved in the system. For incompressible fluids, $\frac{\partial \rho}{\partial t} = 0$, and eq. 2.25 reduces to,

$$\nabla \cdot \mathbf{u} = 0. \tag{2.26}$$

The first term on the left hand side of eq. 2.24 is the force pr. unit fluid volume due to unsteady acceleration. As an example, this term would be zero for a steady flow of water through a hose pipe. Steady flow meaning that the volume of water flowing through a cross section of the hose pipe pr. unit time is constant. The second term on the left hand side describes the force pr. unit fluid volume due to *convective* acceleration of fluid particles. Convection refers to the internal current changes within fluids. If the hose pipe in the above example had a gradually decreasing cross section, the convective acceleration would be non-zero, since for a steady flow

the fluid particles would have to accelerate as they moved down the hose. This follows from mass conservation (eq. 2.26).

The right hand side of eq. 2.24 is the sum of body forces on a fluid volume. The first term represents forces due to pressure gradients in the fluid, the second term is the viscous force due to shear stresses and the third term is the effect of acceleration of gravity as mentioned. The following boundary conditions must be imposed for eq. 2.24 to hold:

- Fluid velocity at the solid surface must be zero (no-slip).

- At the fluid/fluid interface, the velocities must be equal.

- Forces exerted by fluids on both sides of the interface must be balanced by capillary forces.

In addition to these boundary conditions, a lot more information about the flow regime itself is needed, as discussed in [13]. Due to the complex geometry of porous media, the flow regime inherits this complexity, and the equations described above will be very hard to solve. Evidently the situation gets even more complicated when using a compressible fluid, as is the case in our experiments. The difficulty of solving two-phase flow problems based on the Navier-Stokes equations at pore scale, has motivated the use of a direct phenomenological macroscopic description.

2.2.3   Phenomenological macroscopic description, the Darcy equation

In 1856 Henry Darcy found a relation between the fluid flow and pressure gradient of one-phase flow through porous media, later to be known as the Darcy equation. The experiment consisted in varying the flow of water through a sand filled cylinder. The measured pressure differences between the inlet and outlet were then compared to the flow-rates. Darcy's results are widely used in the study of single-phase flow through porous media. In fact the Darcy equation has also been generalized for multi-phase flow, although the applicability in this case is more questionable.

The differential form of Darcy's equation for single-phase flow is given as:

$$\mathbf{v} = -\frac{K}{\mu} \left(\nabla P - \rho \mathbf{g} \right),\tag{2.27}$$

where the volume flux $v = Q/A$, is called the *filtration-* or *Darcy-velocity*. Q is the volumetric flow-rate through the porous medium, and has units of $[m^3/s]$. A is the cross section of the porous media orthogonal to the flow, K is the permeability, μ the viscosity, ∇P the global pressure gradient and ρ the density. Note that the actual velocity u through the porous medium, differs from the Darcy velocity, since the porosity ϕ of the medium must be taken into account:

$$u = \frac{Q}{\phi A} \quad \Rightarrow \quad v = \phi u.\tag{2.28}$$

Thus the Darcy velocity is smaller than the actual velocity by a factor of ϕ.

The Darcy equivalent of the continuity equation, eq. 2.25, is given by [16]:

$$\frac{\partial \phi \rho}{\partial t} + \nabla \cdot \rho \mathbf{v} = 0.\tag{2.29}$$

When eq. 2.27 and 2.29 are combined, we obtain the dynamical equation,

$$\frac{\partial \phi \rho}{\partial t} = \nabla \cdot \left[\rho \frac{K}{\mu} \left(\nabla P - \rho \mathbf{g} \right) \right].\tag{2.30}$$

If we introduce the scalar potential $\psi = \rho \frac{K}{\mu} \left(P - \rho g z \right)$, then for incompressible fluids, eq. 2.30 can be written as:

$$\nabla^2 \psi = 0.\tag{2.31}$$

Eq. 2.31 is the Laplace equation, and it is found to apply in many fields of physics. Examples are electrostatics, elasticity theory, diffusion etc. The Laplace equation tells us that the potential gradient is constant, meaning that the potential changes linearly as a function of position.

Darcy's equation is phenomenological, meaning that it does not follow directly from the Navier Stokes equations. It is a proposed relation based on experimental measurements, found to be satisfied to an acceptable degree in most practical situations. However the literature also refers to experiments where the pressure gradient was found not to follow Darcy's law. This seems to be the case for very high flow rates as discussed in [20]. It should also be made clear that the Darcy velocity is an average measure of the velocity through many pores, and thus a macroscopic quantity.

For multi-phase flow, the following generalization of Darcy's law has been proposed under certain conditions

$$Q_w \mathbf{n} = -\frac{k_w^e A}{\mu_w}(\nabla P_w - \rho_w \mathbf{g}) \tag{2.32}$$

$$Q_{nw} \mathbf{n} = -\frac{k_{nw}^e A}{\mu_{nw}}(\nabla P_{nw} - \rho_{nw} \mathbf{g}), \tag{2.33}$$

for the wetting and non-wetting phase respectively. $\mathbf{n}$ is a unit vector in the direction of flow, and k^e is referred to as *effective permeability*. Contrary to the absolute permeability K, the effective permeability depends not only on the pore geometry, but also on several other flow parameters. Consider two phases flowing, either face "meets" larger resistance due to the presence of the other phase and $\{k_w^e, k_{nw}^e\} < K$. The effective permeability is dependent on saturation. If S_w increases, k_{nw}^e decreases, since there are less flow paths available for the non-wetting phase. It is custom to normalize the effective permeability by the absolute permeability,

$$k_i^r = \frac{k_i^e}{K} \quad (i \in w, nw), \tag{2.34}$$

where the dimensionless quantity k_i^r, is called the *relative permeability*.

In the context of multi-phase flow and relative permeabilities, it is common to introduce the *fractional flow* of the wetting and non-wetting phase as,

$$F_w = \frac{Q_w}{Q_{tot}} \tag{2.35}$$

$$F_{nw} = \frac{Q_{nw}}{Q_{tot}}, \tag{2.36}$$

where $Q_{tot} = Q_w + Q_{nw}$. F_i is a measure of i'th phase contribution to the total flow-rate. It is analog to saturation, where S_i is the i'th phase contribution to the total pore-space volume.

The generalized Darcy equations assume that the flow of both phases is hydrodynamically independent. This means that the flow of wetting fluid is uncoupled with that of the non-wetting. The non-wetting fluid appears as a "solid" to the wetting fluid and vice versa. Eq. 2.32-2.32 were originally considered to apply when the whole system reached steady-state. As a preliminary definition, steady-state means that Q_i, k_i^r and ∇P_i are constant. However, the generalization has been taken further by assuming that it also applies within blocks of a non-steady-state system [21]. The rationale behind applicability also for non-steady state systems, is that the blocks are small enough for steady-state conditions to apply within each block. The blocks must also be large enough for Darcy's law to apply in its macroscopic form. Two different steady-state realizations are shown in figure 2.7. These scenarios are idealizations, and very often the flow patterns are much more complex. The global time averaged saturation in a system may be constant but the interfaces between the phases may continuously change. As an example, consider figure 2.7 a). In addition to the connected pathways shown, there will in general also be smaller clusters of both phases. Some of these clusters are mobilized, and they can both get fragmented and coalesce as they move in the porous matrix. In this case the multi-phase flow can not be considered hydrodynamically independent.
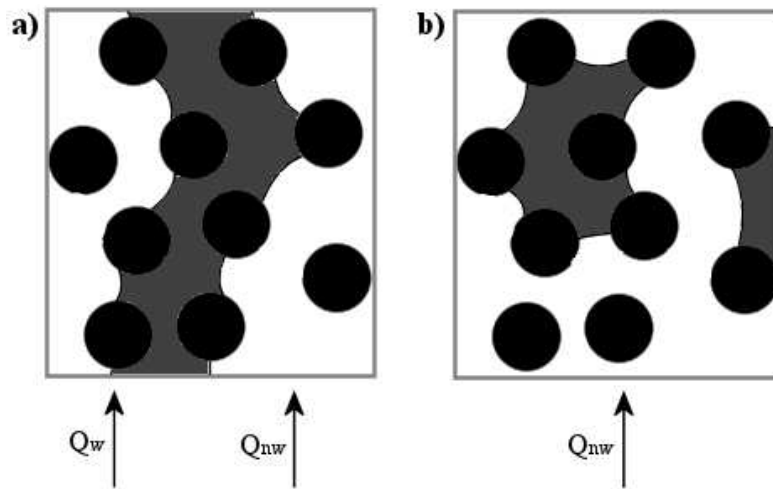
Figure 2.7: *Two different steady-state flows. In both a) and b) the porous media is initially saturated with a wetting fluid. Q_w and Q_{nw} are the constant flow-rates of the wetting and non-wetting fluid respectively. In **a)** a flow of both fluids is imposed on one side. After an initial transient of displacing wetting fluid, a steady-state is reached where the flow of each fluid is constrained to connected pathways through the porous medium. In **b)**, a flow of only the non-wetting fluid is imposed. After the initial transient, when no more wetting fluid is displaced from the system, steady-state is reached with the wetting fluid completely trapped. In this case only eq. 2.33 can be applied.*

Based on experiments and dimension analysis it follows [17] that the relative permeabilities in a given porous medium are in general functions of several variables:

$$k_i^r = k_i^r \left(S_w, Ca, Q_w, Q_{nw}, M, \theta, Bo \right) \qquad i \in w, nw, \tag{2.37}$$

where S_w is the wetting fluid saturation, Ca is the ratio of viscous and capillary forces, M is the viscosity ratio, θ is the wetting angle and Bo is the ratio of gravitational and capillary forces. Since the relative permeability of the wetting fluid depends on non-wetting fluid parameters and vice versa, coupling terms have been introduced to improve eq. 2.32-2.33. For a further discussion of the multi-variable dependence of relative permeabilities and coupling terms in the generalized Darcy law, see [13], [20] and [21].

Both Darcy's law and its generalization, lacks theoretical justification. It is however still frequently used, due to good experimental agreement.

2.2.4   Darcy's law for compressible fluids

In this subsection we present some of the implications of Darcy's law when fluids are compressible. This is relevant since air is used in our experiments to displace a mixture of glycerol/water through porous media. In this context, air will sometimes be refereed to as a fluid.

Steady-state flow is characterized by vanishing partial time derivatives. For a horizontal flow eq. 2.30 gives,

$$\nabla \cdot \left(\rho \frac{K}{\mu} \nabla P \right) = 0. \tag{2.38}$$

For an ideal gas[2], we assume an equation of state:

$$\frac{P}{\rho^\gamma} = c, \tag{2.39}$$

---

[2]We consider air as an ideal gas.

where c is a constant, and the exponent γ depends upon what kind of compression is in question (isotherm, adiabatic etc). The equation of state gives,

$$\nabla \cdot \left(\frac{K}{\mu c} P^{\frac{1}{\gamma}} \nabla P \right) = 0 \tag{2.40}$$

$$\nabla \cdot \left(P^{\frac{1}{\gamma}} \nabla P \right) = 0. \tag{2.41}$$

Using index notation we denote $\partial_i = \partial/\partial x_i$. It is then straight forward to show that,

$$\partial_i \partial_i \left(P^{1+\frac{1}{\gamma}} \right) = \left(1 + \frac{1}{\gamma} \right) \partial_i \left(P^{\frac{1}{\gamma}} \partial_i P \right) \tag{2.42}$$

$$\nabla \cdot \nabla P^{1+\frac{1}{\gamma}} = \left(1 + \frac{1}{\gamma} \right) \nabla \cdot P^{\frac{1}{\gamma}} \nabla P. \tag{2.43}$$

Eq. 2.41 then becomes the Laplace equation,

$$\frac{1}{1 + \frac{1}{\gamma}} \nabla \cdot \nabla P^{1+\frac{1}{\gamma}} = 0 \tag{2.44}$$

$$\nabla^2 P^{1+\frac{1}{\gamma}} = 0, \tag{2.45}$$

The Laplacian is the governing equation also for single-phase flow of an ideal gas through a porous medium. Thus, the potential $P^{1+\frac{1}{\gamma}}$ must have the following form in a one-dimensional case,

$$P^{1+\frac{1}{\gamma}} = ax + b, \tag{2.46}$$

where x is position, a and b are constants to be determined. If we impose boundary conditions of the form, $P(x = 0) = P_{\text{in}}$ and $P(x = L) = P_{\text{out}}$, where L is the length of the model, eq. 2.46 gives

$$P(x) = \left(\frac{P_{\text{out}}^{1+\frac{1}{\gamma}} - P_{\text{in}}^{1+\frac{1}{\gamma}}}{L} x + P_{\text{in}}^{1+\frac{1}{\gamma}} \right)^{\frac{\gamma}{1+\gamma}}. \tag{2.47}$$

Eq. 2.47 inserted into Darcy's law gives:

$$v(x) = -\frac{K}{\mu} \frac{\partial P}{\partial x} \tag{2.48}$$

$$v(x) = -\frac{K}{\mu} \frac{P_{\text{out}}^{1+\frac{1}{\gamma}} - P_{\text{in}}^{1+\frac{1}{\gamma}}}{L} \left(\frac{\gamma}{1+\gamma} \left[\frac{P_{\text{out}}^{1+\frac{1}{\gamma}} - P_{\text{in}}^{1+\frac{1}{\gamma}}}{L} x + P_{\text{in}}^{1+\frac{1}{\gamma}} \right]^{-\frac{1}{1+\gamma}} \right). \tag{2.49}$$

For an isothermal process, i.e constant temperature, $\gamma = 1$ and eq. 2.49 simplifies to

$$v(x) = -\frac{K}{\mu} \frac{P_{\text{out}}^2 - P_{\text{in}}^2}{2L} \left(\frac{P_{\text{out}}^2 - P_{\text{in}}^2}{L} x + P_{\text{in}}^2 \right)^{-\frac{1}{2}}. \tag{2.50}$$

Several interesting properties can be deduced from eq. 2.49-2.50. In the incompressible limit[3] when $\gamma \to \infty$, the Darcy velocity is constant (seen from eq. 2.49). With the assumption of low pressure difference we can show that a gas essentially behaves as an incompressible fluid, during single phase flow in a porous medium. Consider $P_{\text{out}} = P_0$, where P_0 is the atmospherical

---

[3]For an incompressible fluid, the equation of state, eq. 2.39, requires density to be constant, hence $\gamma \to \infty$.

pressure, and $P_{in} = P_0 + \delta P$, where δP is a small perturbation of the atmospherical pressure. If we rewrite eq. 2.50 to the form,

$$v(x) = -\frac{K}{\mu L} \underbrace{\frac{P_{out}^2 - P_{in}^2}{2P_{in}}}_{\star} \left(\underbrace{\frac{P_{out}^2 - P_{in}^2}{P_{in}^2} \frac{x}{L}}_{\square} + 1 \right)^{-\frac{1}{2}} , \tag{2.51}$$

and Taylor-expand $\delta P/P_0$ and $2\delta P/P_0$ around 0 in the $\star$- and $\square$-term respectively to first order,

$$v(x) = \frac{K}{\mu} \frac{\delta P}{L} \left(1 - \frac{\delta P}{2P_0} \right) \left(1 - \frac{2\delta P}{P_0} \frac{x}{L} \right)^{-\frac{1}{2}} . \tag{2.52}$$

Figure 2.8: *Darcy velocity as a function of position along the model during single phase flow. The constant line is Darcy's law for incompressible fluids, whereas the linear graph is found using eq. 2.50. v_0 and v_L can be used as error estimates in assuming that air is incompressible.*

If we further Taylor-expand, $f(u) = \frac{1}{\sqrt{1-u}} \approx 1 + \frac{1}{2}u + ...$, where $u = 2\delta Px/P_0L$, we get:

$$v(x) = \frac{K}{\mu} \frac{\delta P}{L} \left(1 - \frac{\delta P}{2P_0} \right) \left(1 + \frac{\delta P}{P_0} \frac{x}{L} \right) . \tag{2.53}$$

When inserting the limits $x = 0$ and $x = L$, eq. 2.53 gives:

$$v_{0,L} = \frac{K}{\mu} \frac{\delta P}{L} \left(1 \mp \frac{\delta P}{2P_0} \right) \quad \left\{ \begin{array}{ll} -, & x = 0 \\ +, & x = L \end{array} \right. . \tag{2.54}$$

Since $f(u)$ is monotonically increasing, it follows that

$$v(x) \in [v_0, v_L]. \tag{2.55}$$

These two points can be used as the error one is making by considering the air to be incompressible, under the assumption $P_{in} = P_0 + \delta P$. In figure 2.8 we have plotted eq. 2.27, eq. 2.50 and eq. 2.54 for typical flow parameters of air. From the figure it follows that we make an error of

± 1.5 [cm/s], if we consider the air to be incompressible, with a Darcy velocity of $v = 63$ [cm/s]. Further treatment of compressible single-phase flow in porous media can be found in [22].

With multi-phase flow, air can in general not be considered incompressible. Imagine a steady-state situation, with air and an incompressible fluid injected into a porous medium simultaneously. The effective permeability of air k_{air}^e is much lower than the absolute permeability of the medium. Thus, the air pressure drop is much higher than in the case of single-phase flow. If we assume that eq. 2.33 hold, we can substitute $K = k_{air}^e$ in eq. 2.50. In figure 2.9 we plotted eq. 2.50 with the same system length and viscosity as in figure 2.8, but with a low effective permeability and a high pressure drop. From the figure we see that the Darcy velocity increases towards
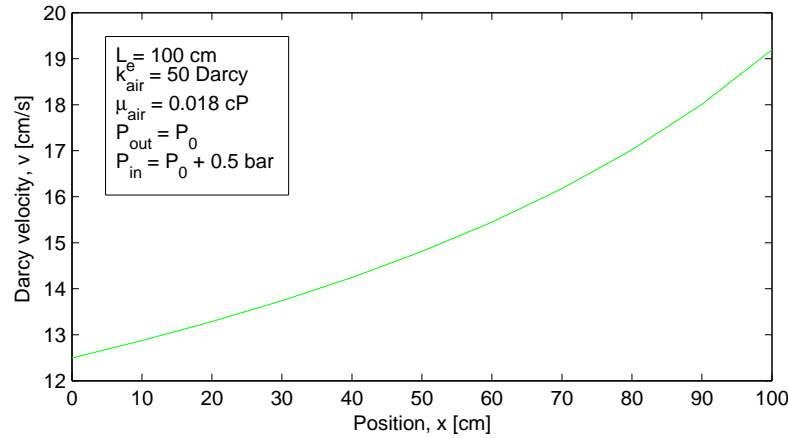

Figure 2.9: *Darcy velocity of air as a function of position during multi-phase flow. In this case we assume a low effective permeability and a high pressure drop over the model.*

the end of the model. In this case air cannot be considered incompressible. Since $v = Q/A$ the flow-rate is proportional to v. The flow-rate $Q = dV/dt$, can increase in two ways. Either the air expands so that a larger volume passes through the cross section A pr. unit time, or the volume stays constant but more of it passes through A pr. unit time. Figure 2.9 must be considered only as a rough estimate, since simultaneous two-phase flow is much more complex than single-phase flow. From the discussion in section 2.2.3, appliance of the generalized Darcy equation means that the flow of air and fluid is restricted to separate channels. The flow will in general consist of a mix of both phases, which introduces more capillary barriers. These barriers will contribute to an additional air pressure drop.

2.3   The competition between forces

Due to the complexity of displacement processes in porous media, it is impossible to give exact solutions based on the Navier-Stokes equations. Instead we try to identify dominating forces that can account for the observed structure. The most important are gravitational-, capillary- and viscous forces. It is common to introduce several dimensionless numbers, describing the competition of these forces on the pore scale. Flow regimes are characterized by different values of the dimensionless numbers.

The first dimensionless number we will look at is the *Reynolds*-number Re, well known from fluid mechanics. The Reynolds number describes the degree of turbulence in fluid flow, and is given as,

$$\text{Re} = \frac{ul}{\nu}, \tag{2.56}$$

where u is the fluid velocity, l is a characteristic length scale in the system and ν the kinematic viscosity. Low values of Re give non-turbulent flow, intermediate values give unstable flow with periodic patterns in the velocity field and high values give chaotic or turbulent flows. Most flows in porous media can be considered non-turbulent.

For non-horizontal flow in porous media, gravity effects can be important. The dimensionless number describing the effect of gravity is called the *Bond*-number, Bo. The Bond-number gives the ratio between gravitational pressure and capillary pressure over characteristic pores,

$$\text{Bo} = \frac{\Delta P_{\text{grav}}}{\Delta P_{\text{cap}}} = \frac{\Delta \rho g a^2}{\gamma}. \tag{2.57}$$

In the above equation, $\Delta P_{\text{grav}} = \Delta \rho g a$ is the gravitational or hydrostatic pressure drop over a pore of characteristic size a, $\Delta \rho = \rho_w - \rho_{nw}$ is the density difference between the wetting and non-wetting fluid respectively and g is the component of gravity in the direction of flow. The capillary pressure drop over a typical pore-throat is approximated by $\Delta P_{\text{cap}} \approx \frac{\gamma}{a}$, and so eq. 2.57 follows. Small values of the Bond number means that capillary forces dominate over the gravitational ones. Especially we notice that when **g** is perpendicular to the flow, as in horizontal models, Bo $= 0$.

If we look at the ratio of viscous to capillary forces, we get the *Capillary*-number, Ca. In experimental studies it is usually defined as [4], [23]:

$$\text{Ca} = \frac{\Delta P_{\text{visc}}}{\Delta P_{\text{cap}}} = \frac{\mu_w Q_{\text{tot}} a^2}{\gamma K A}. \tag{2.58}$$

The viscous pressure drop follows from Darcy's law over a pore of size a; $\Delta P_{\text{visc}} = \mu_w Q_{\text{tot}} a / KA$, where Q_{tot} is the global flow-rate in the system. In section 2.2 we emphasized that Darcy's law could only be applied over macroscopic regions, so how can it be applied here on the pore scale? The intention with the capillary number is not to determine the ratio with high accuracy. An estimate of the forces will do, and so the appliance of Darcy's law as a rough approximation is found to suffice. In network simulations of multi-phase flow, the capillary number is often taken as,

$$\text{Ca}^* = \frac{\mu_{\text{eff}} Q_{\text{tot}}}{\gamma A}. \tag{2.59}$$

In eq. 2.59 μ_{eff} is an effective viscosity. It is sometimes taken as the viscosity of the most viscous fluid, [8]. Another definition is, $\mu_{\text{eff}} = \mu_{nw} S_{nw} + \mu_w S_w$, [25]. Viscous forces are said to dominate the flow if Ca ~ 1. When Ca $\ll 1$, the capillary forces are the dominating ones. Since the capillary number is defined differently in the literature, care must be taken when comparing results from different studies.

2.4 Flow regimes

When two immiscible fluids flow in porous media many different structures can develop, dependent on pore geometry, fluid parameters and boundary conditions. In this section we discuss the most relevant regimes for this thesis. For treatment also of other regimes, the reader is referred to a description by Payatakes *et al.* [26]. Some of the flow regimes have been studied extensively and are considered well understood, whereas others have yet to be explored fully.

2.4.1 Drainage and imbibition

In a displacement process, the fluid being displaced is called the *defending* fluid, and the fluid displacing is referred to as the *invading* fluid. When a non-wetting fluid displaces a wetting fluid, the process is called *drainage*. In the opposite case, where a wetting fluid displaces a non-wetting fluid, the process is called *imbibition*.

Figure 2.10 serves to illustrate a main difference between these two flows. If we consider very slow displacements, viscous effects can be neglected, and the capillary forces dominate. In figure 2.10 a) we have a drainage process, and $P_{nw} > P_w$. The capillary threshold in two pore-throats are shown, $P_{c,1} < P_{c,2}$. Further we assume that $P_{c,1} < P_{cap} < P_{c,2}$. The equilibrium curve P_{eq}, shows the capillary pressure required for eq. 2.22 to hold. The meniscus will be stable and thus in equilibrium only when $P_{cap} = P_{eq}$. When the meniscus is in the position $x_0 + \delta x_0$, the interface is unstable and it will spontaneously start to invade the pore. Equilibrium can first be established at the position $x_1 - \delta x_1$.
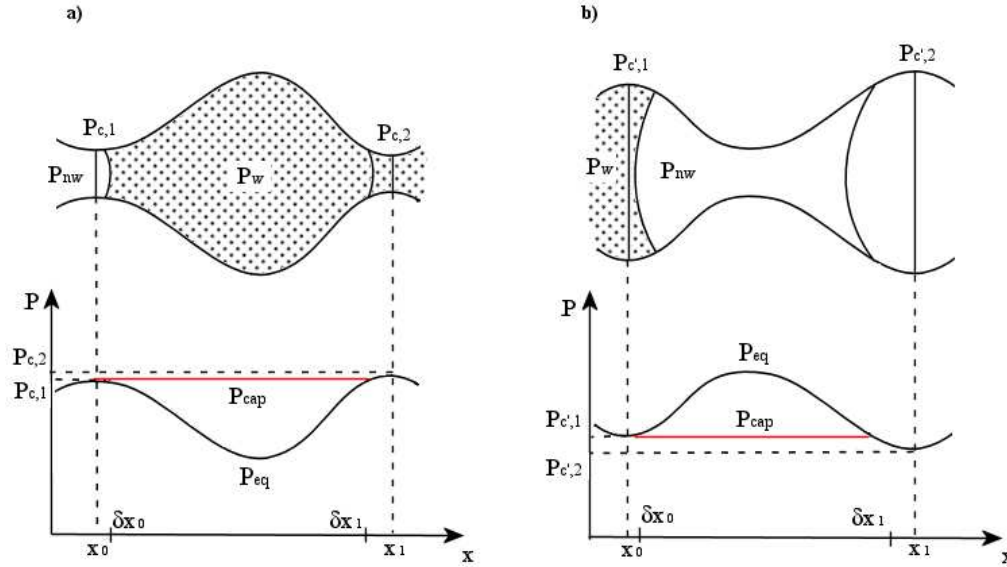

Figure 2.10: *Difference between drainage and imbibition. In both cases $P_{nw} > P_w$. The curve P_{eq}, is the capillary pressure required for equilibrium to be obtained.* **a)** *Drainage displacement. Two capillary thresholds are shown, $P_{c,1} < P_{c,2}$. Further the capillary pressure is given by $P_{c,1} < P_{cap} < P_{c,2}$. The meniscus stabilizes in the position $x_1 - \delta x_1$, since $P_{cap} < P_{c,2}$.* **b)** *Imbibition displacement. Two capillary thresholds are shown, $P_{c',1} > P_{c',2}$. The capillary pressure is given by $P_{c',1} > P_{cap} > P_{c',2}$. The meniscus stabilizes at the position $x_1 - \delta x_1$, since $P_{cap} > P_{c',2}$.*

Because the net force, caused by capillary pressure, exceeds the force of surface tension we get spontaneous invasion during drainage. When it comes to spontaneous invasion during imbibition, the exact opposite occurs. It is the curvature of the interface, hence the forces of surface tension that exceeds the capillary forces. The phenomenon is known as capillary suction. Non-wetting fluid will try to suck wetting fluid into narrow parts (pore-throats) of the embedding geometry. As a consequence, non-wetting fluid will resist displacement from wide parts (pores) of the geometry. During imbibition, a reduction in capillary pressure is required to move non-wetting fluid into wider parts of a pore. Analog to what is done for drainage, we define a minimum critical capillary pressure $P_{c'}$ associated with the widest part of a pore. To invade a pore-throat,

$$P_{cap} < P_{c'}, \quad \text{for imbibition.} \tag{2.60}$$

In figure 2.10 b) we have an imbibition process. The capillary threshold in two pores are shown, $P_{c',1} > P_{c',2}$. Also in this case we assume that the capillary pressure is between the two thresholds, $P_{c,1} > P_{cap} > P_{c,2}$. When the meniscus is in the position $x_0 + \delta x_0$, the interface is unstable and it will spontaneously start to invade the pore-throat. Equilibrium can first be established at the position $x_1 - \delta x_1$. To imbibe the next pore-throat the capillary pressure must be further decreased. This implies an increase in the driving pressure P_w if P_{nw} is constant.

A detailed treatment of drainage and imbibition is found in the much quoted study of Lenormand *et al.* [27].

2.4.2 Capillary fingering

When the capillary forces completely dominate viscous forces, the capillary number Ca will be low. For a drainage process this means that a non-wetting fluid displaces a wetting fluid at a very low flow-rate in a porous medium. The pressure inside each fluid is everywhere the same and the pressure difference between the non-wetting and wetting fluid is given by the capillary pressure, eq. 2.21. Imagine a two-dimensional porous medium saturated with wetting fluid, except for a channel at the inlet connected to a non-wetting fluid reservoir. If non-wetting fluid is pumped into the porous medium at a very slow rate, P_{nw} will start to increase. At first this is a stable situation. The front is located along a line at the inlet, trying to overcome the capillary barriers presented by the pore-throats. It is here that the randomness of the porous media comes into play. The widest pore-throat along the front will have the smallest capillary threshold, $P_{c,i}$. Since P_w is constant, an increase in P_{nw} will increase P_{cap} and whenever $P_{cap} > P_{c,i}$, the front becomes unstable and invades the pore in front of the widest pore-throat. The spontaneous invasion of pores are called *bursts*, and they take place over a much smaller timescale than the advancing of the front in the pore-throats. The number of pores invaded in a burst depends on the capillary pressure, because the front will not stabilize until it finds a new configuration in which all capillary thresholds are greater than the current capillary pressure. Måløy *et al.* [2] [29] studied how the capillary pressure varied under slow drainage experiments. It was found that a sudden drop in capillary pressure accompanied every burst. They also observed that the volume of displaced defending fluid during a burst, did not leave the model, but was redistributed over the front making the menisci retract. This capacitive volume effect was found to be the reason for the sudden pressure drops. After a burst, equilibrium is obtained and P_{nw} must be increased to continue invasion. In this manner, the wetting fluid is displaced from the porous media, until the non-wetting fluid percolates the model for the first time. When it does, we have *breakthrough*.

Figure 2.11 a) shows the resultant structure from a displacement in the capillary fingering regime at breakthrough. Trapped clusters of wetting fluid appear in all sizes, and their distribution is fractal. The size of the smallest clusters are bound by the pore size, whereas the system size sets an upper limit of the largest clusters. These characteristic length scales, are referred to as the upper and lower cutoff lengths of the system. The same cutoff lengths are also found in ordinary percolation theory. In 1983, Wilkinson and Willemsen introduced the *invasion percolation* (IP) algorithm motivated by the statistical similarity between capillary fingering and percolation. It is based on the mapping of capillary pressure thresholds to occupation probabilities in regular lattice sites. A short description follows:

Invasion Percolation, IP

1. Every site in a $L_x \times L_y$ lattice is assigned a random number in the unit interval.

2. In the first time step, the bottom row is occupied by invading fluid (lattice sites equal to one), and the rest of the lattice is saturated with defending fluid (lattice sites equal to zero).

3. The front between zeros and ones are identified, and the front site with the lowest random number (the lowest capillary threshold) is set to one (invaded).

4. For each time step the front is updated, and 3. is repeated.

5. If the so called *trapping* rule is included; all regions completely surrounded by invading fluid (trapped regions) must be removed from the list of possible invading sites.

6. The process is stopped when one of the sites at L_y has been invaded (breakthrough).
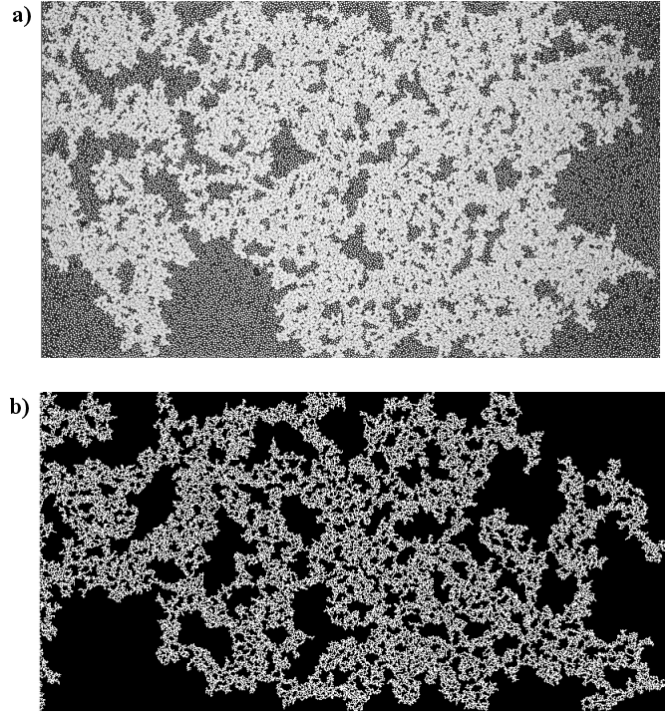
Figure 2.11: *a) Air (white) displacing a water/glycerol mixture (black) in a porous Hele-Shaw cell, performed by M. Jankov at the Complex group (2006). System size of ~ 44100 pores, $Ca \sim 10^{-4}$. b) IP-simulation with trapping in a 400×800 lattice. The fractal dimension was calculated to, $D_{trap} = 1.81 \pm 0.03$. The similarity between a) and b) is evident.*

Wilkinson and Willemsen also found that the mass of the invasion cluster without trapping, scales with the size of the lattice

$$M(L) = AL^{D_{IP}}, \tag{2.61}$$

where L is the system size in a quadratic lattice, A is a constant and D_{IP} is the fractal[4] dimension of the invading cluster. Simulations have verified that $D_{IP} = D_P = 1.89$, where D_P is the fractal dimension of the ordinary percolation cluster at the critical occupation probability. If trapping is included eq. 2.61 is also valid, but the fractal dimension is lower, $D_{\text{trap}} \simeq 1.82$. In 1985 Lenormand and Zarcone investigated the displacement of glycerol by air in the capillary regime, [35]. They found that eq. 2.61 was satisfied with $1.80 < D_{\text{trap}} < 1.83$, in good correspondence with the predicted value.

Motivated by the similarity of IP to real experiments, we implemented the algorithm with trapping in Matlab. The Matlab script can be found in Appendix B.3. In figure 2.11 b), we can se the resulting invasion cluster at breakthrough. When compared to a real experiment (figure 2.11 a)) the similarity is evident. To calculate the fractal dimension D_{trap} of our simulation, we counted the number of invaded sites in a square of side L, in the central region of figure 2.11 b). A fit was made to the data-points according to eq. 2.61, as shown in figure 2.12. We found a fractal dimension $D_{\text{trap}} = 1.81 \pm 0.03$, in good agreement with the predicted value of ~ 1.82.

Even though the statistical properties of a capillary fingering experiment and invasion percolation are very similar, the dynamics represented in the algorithm are far too simple. As an

---

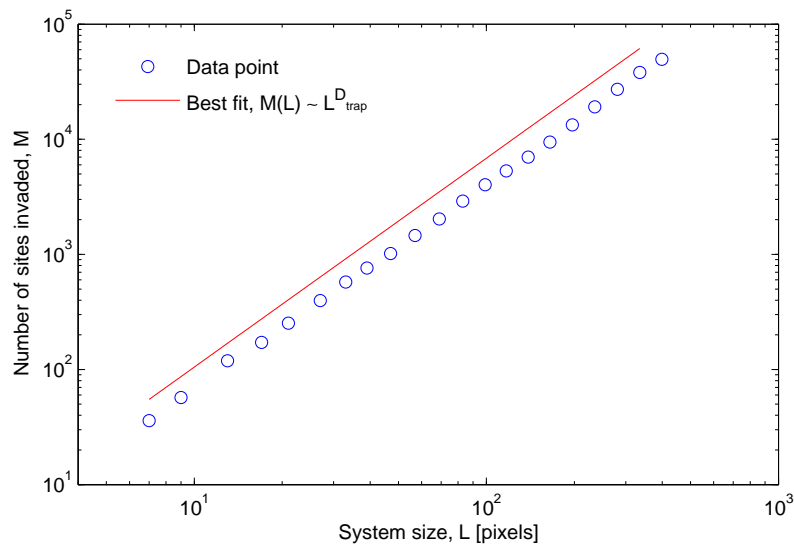[4]The unfamiliar reader is referred to the book by Feder [32].

Figure 2.12: *Mass of the invasion cluster inside a square of side L. The fractal dimension was found to be $D_{trap} = 1.81 \pm 0.03$.*

example it does not handle bursts, since only one pore is invaded at each time step. Måløy *et al.*, [2], [29], proposed a new modified invasion percolation algorithm, including burst dynamics. The simulation results were in good correspondence with experiments.

Note that the displacement structure will depend on the wetting angle. We have here assumed favorable wetting conditions. That is, a contact angle of the invading fluid around $180°$. Robbins *et al.* [40, 41, 42], studied how ordinary IP structures changed with the wetting properties of the system. They found that below a critical contact angle θ_c, dependent on the porosity, the invasion structure was no longer fractal but flooded the system. When the contact angle approaches the mixed wetting limit, the distribution of capillary thresholds will be drastically altered. Due to the wetting, equilibrium menisci can exist also outside of the pore-throat exit. This means that neighboring menisci can intersect and coalesce. The dynamics of the displacement is in this case altered.

2.4.3 Viscous fingering

When a low-viscous fluid displaces a high-viscous fluid at a large injection rate, we are in the viscous fingering regime. In this case the viscosity ratio $M \ll 1$, and Ca ~ 1. The term *fingering* reflects the finger like structures generated in such a process, as seen in figure 2.1 a). This regime is characterized by fingers of invading fluid, propagating faster through the medium than the rest of the front. Due to this finger development, the front is said to be unstable. Imagine at a stage in the displacement, that some parts of the front get ahead of the rest. Due to the low-viscosity in the invading fluid, the pressure drop is negligible. It then follows from Darcy's law, that the parts of the front closest to the outlet, will experience the highest pressure gradients in the high-viscous defending fluid. This means that the tips of the fingers will propagate at a higher Darcy velocity through the porous medium than the rest of the front. In linear models, one or two fingers usually dominate the growth. By dominate, we mean that the growth of these fingers suppress the growth of smaller fingers further behind. This is also referred to as a screening effect of smaller fingers. In [23] Løvoll *et al.* studied this screening effect. They introduced an active growth sone, located within a characteristic distance from the tip of the most advanced finger.

Viscous fingering was first studied by Saffmann & Taylor (1958) in non-porous Hele-Shaw
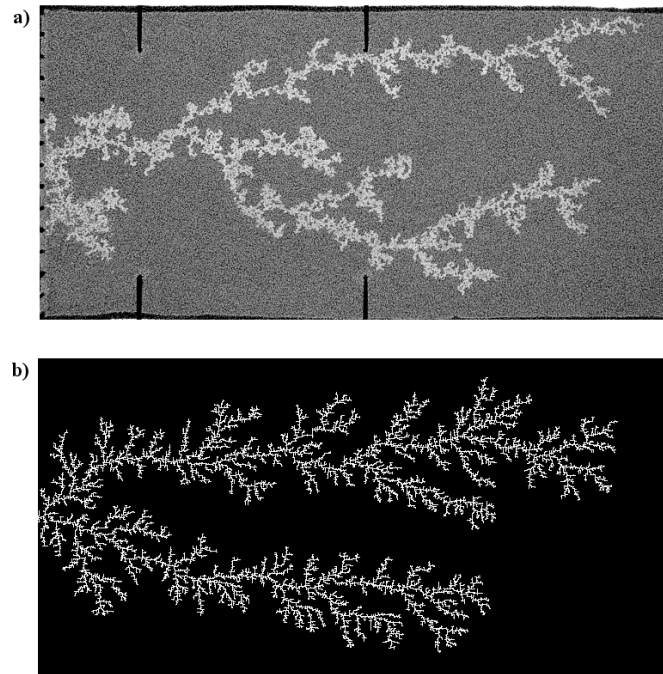
Figure 2.13: *a) Viscous fingering experiment in a rectangular porous Hele-Shaw cell, performed in the Complex lab (2007). Air displaces glycerol from a single inlet node at a high flow-rate. System size of ~ 213600 pores, $M \sim 10^{-4}$ and $Ca = 0.16$. The finger-like structure observed is characteristic for this flow regime. b) DLA-simulation in a 400×800 lattice. The aggregate is grown from a single lattice site, to have the same boundary conditions as the experiment in a). Also in this case, two fingers dominate the growth, although they are thinner and more branched compared to the experiment.*

cells [30]. They found that if an initial flat fluid/fluid interface was perturbed above a critical wavelength, viscous fingers would develop. This is known as the Saffmann-Taylor instability.

For viscous fingering in porous Hele-Shaw cells, Paterson demonstrated in 1984 [31] the similarity with *Diffusion Limited Aggregation* (DLA). One form of DLA is the process where random particles are left to wander randomly until they collide with the initial seed or already fixed particles. In this way an aggregate is formed as more and more particles stick to the growing structure. A simple version of the DLA algorithm can be formulated as follows:

Diffusion Limited Aggregation, DLA

1. In an empty (all sites equal zero) $L_x \times L_y$ lattice, plant the initial seed(s) (sites are set equal to one) according to the wanted boundary condition.

2. Release a random-walker at a random position along the top row of the lattice. Whenever the walker attempts to jump at the boundaries of the lattice, it is reflected. When the walker hits one of the seed neighboring sites, it sticks (the site is invaded and set equal to one). Another walker is then released from the top row.

3. The point above is repeated until the aggregate reaches the top row (breakthrough).

For the analogy between viscous fingering and DLA to hold, the viscosity of the non-wetting fluid must be very low, the flow-rate must be high and the pore-throat distribution must be truly random. It can be shown [32] that in the continuum limit DLA is described by the diffusion equation, and further that it obeys the Laplace equation. In viscous fingering the flow is also governed

by the Laplacian through Darcy's law. However there is a different type of disorder in the two processes. In DLA, disorder is displayed by the random-walkers, so called annealed disorder. In viscous fingering, the disorder is quenched in the porous medium, so called quenched disorder. Due to this difference, there is no simple one-to-one correspondence between viscous fingering in porous media and DLA.
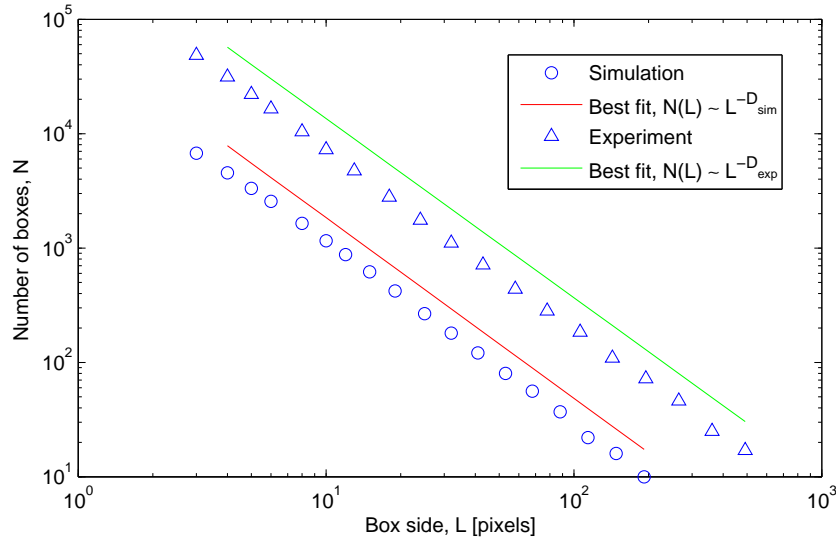

Figure 2.14: *Box-counting method for the experiment and DLA-simulation shown in figure 2.13. The fractal dimensions were found to be $D_{exp} = 1.57 \pm 0.04$ and $D_{sim} = 1.58 \pm 0.03$ for the experiment and simulation respectively.*

The resulting structure of both DLA and viscous fingering is found to be fractal. In [1], Måløy *et al.* confirms the analogy between DLA and viscous fingering. They study the structure resulting from injecting air at the center point in a radial porous Hele-Shaw cell, saturated with freshly mixed epoxy. The fractal dimension of the experiment was found to be $D = 1.62 \pm 0.04$, whereas the DLA value quoted in [1] was $D = 1.68 \pm 0.05$. The fractal dimension in viscous fingering is less than that of invasion percolation. This is to be expected since viscous fingers fills less space than the invasion percolation cluster.

We also implemented the DLA-algorithm in Matlab. The script can be found in Appendix B.4. To simulate fluid injection from a point, the aggregate was grown from a single initial seed. In figure 2.13 we have a comparison of the DLA-simulation with a viscous fingering experiment. The DLA-cluster is shown right before breakthrough, and we can see that two fractal fingers dominate the growth. In the experiment, air is injected at a inlet node and displaces a water/glycerol mixture. Similar to the DLA-simulation, two fingers grows faster than the rest of the front. However the experimental fingers are more compact, with less sub-branching than the DLA fingers. We expect this to be a capillary effect, resulting from insufficient flow-rate. To estimate the fractal dimension of the experiment and simulation, we used the box-counting method. The number of boxes of side L needed to cover the fractal in each case was measured, as shown in figure 2.14. We found the fractal dimensions to be, $D_{sim} = 1.58 \pm 0.03$ and $D_{exp} = 1.57 \pm 0.04$, for the simulation and experiment respectively. These values are a good indication of an analogy between DLA and viscous fingering.

2.4.4   Stable displacement

The third flow regime we will look at is stable displacement. It is obtained when a high-viscous fluid displaces a low-viscous fluid, opposite to that of viscous fingering, but still at high flow-rate so that Ca ~ 1 and $M \ll 1$. The displacement front is in this case almost flat. A small roughness is observed and it is due to the disorder of the porous media. Since the front is flat, there are little trapping of defending fluid. Only small trapped clusters are observed for lower flow-rates, and the maximum cluster size is bound by the roughness of the front. The reason for stabilization in
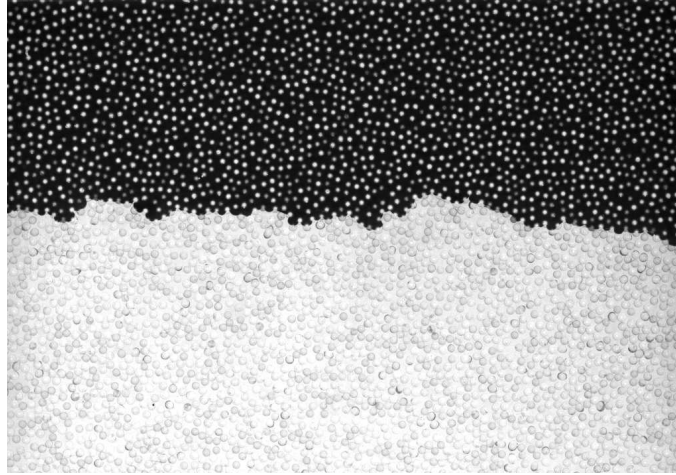

Figure 2.15: *Stable displacement imbibition experiment in a porous Hele-Shaw cell, by S. Santucci at the Complex group (2006). A viscous water/glycerol mixture (black) displaces low-viscous air (white) at a flow-rate of $Q_{tot} \approx 69$ ml/min. The front is flat, without any trapping of air clusters. Size of cropped section: 85×59 mm.*

this case, is that advanced parts of the front will experience lower pressure gradients than parts further behind. Thus the pores closest to the inlet will always be considered for invasion before any of the advanced pores.

In 1984, Paterson also observed [31], in addition to his work on DLA and viscous fingering, that there was a connection between stable displacement and the so called *anti-DLA* process. In anti-DLA there is initially a compact aggregate of defending sites. Random-walkers are in this case introduced as "eaters" of the aggregate. The algorithm can be formulated as follows:

Anti-DLA

1. Initialize a filled (all sites equal to one) $L_x \times L_y$ lattice.

2. Release a random walker from a random position along the inlet line or a point at the inlet, according to the desirable boundary conditions. If the walker hits the "walls" of the lattice, it is reflected.

3. When the walker hits an occupied site, the site is invaded (set equal to zero). Step 2. is then repeated.

4. Step 3. is repeated until breakthrough.

During anti-DLA, the aggregate gets eaten away, and a flat front is observed. Just as with DLA and viscous fingering, no simple one-to-one correspondence is found between anti-DLA and stable displacement. However a correspondence has been established by Lenormand *et al.*, [33]. Figure 2.15 shows a cropped section from a stable displacement experiment.

Stable displacement, capillary fingering and viscous fingering have been studied extensively over the years. The phase diagram of Lenormand *et al.* (1988) [33], given in figure 2.16, sums up these regimes.
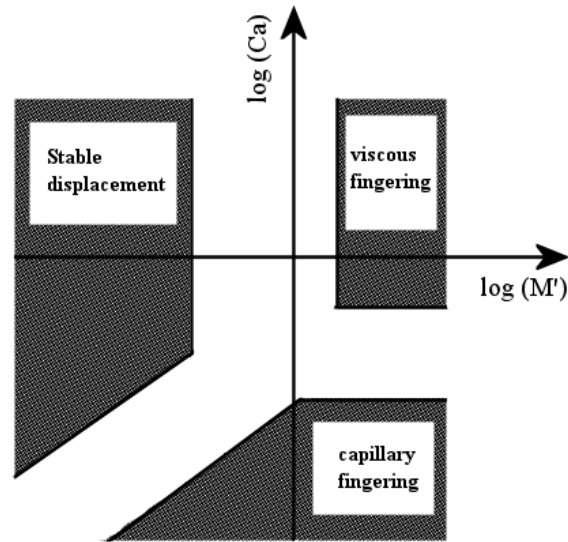

Figure 2.16: *Phase diagram of Lenormand et al. [33]. For a given capillary number and viscosity ratio, the flow regime can be determined. The viscosity ratio is in this case defined as $M' = \mu_{def}/\mu_{inv}$, where μ_{def} and μ_{inv} refer to the viscosity of the defending and invading fluid respectively.*

2.4.5 Gravity stabilization and the pore throat distribution

In all of the above regimes, the flow considered was horizontal, meaning that the Bond number, $Bo = 0$. When the effect of gravity is included the fluid displacement is either stabilized or destabilized dependent on the density difference and flow directions, as explained in [4]. Here we will focus on the case where a low-viscous, low-density fluid (e.g air) displaces a high-viscous, high-density fluid (e.g glycerol). In this case the hydrostatic pressure gradient will tend to stabilize the displacement.

In figure 2.17 we can se how a viscous fingering displacement is affected by increasing the component of gravity parallel to the flow direction. Figure 2.18 serves to illustrate the reason for

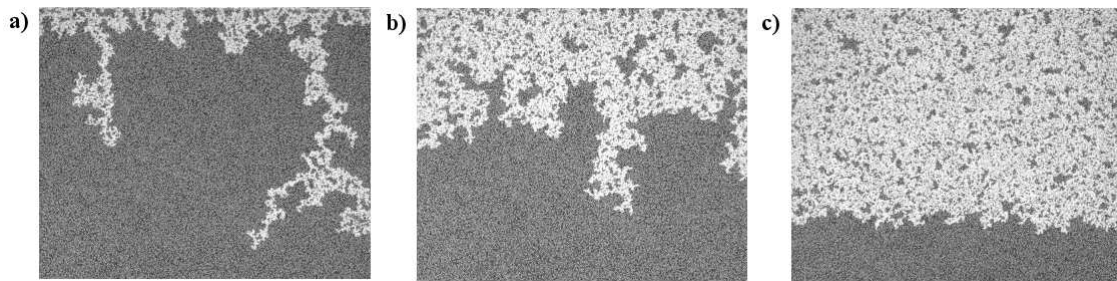**Figure 2.17:** *Gravity stabilized drainage experiments in a porous Hele-Shaw cell, by G. Løvoll at the Complex group (2001). In all cases $Ca = 0.08$. The cell is tilted an angle α from the horizontal plane. In a) $Bo = 0$, $\alpha = 0°$, in b) $Bo = 0.049$, $\alpha = 15°$ and in c) $Bo = 0.155$, $\alpha = 55°$. It is evident that the displacement front stabilize as the Bond-number increase.*

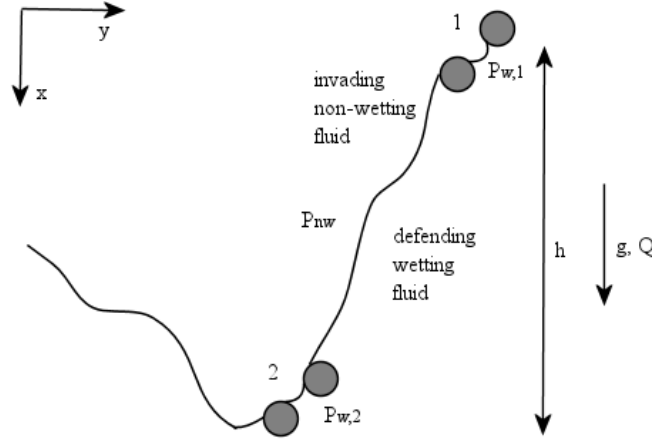stabilization. Due to the low viscosity and low density of the non-wetting fluid, the pressure P_{nw}

Figure 2.18: *Vertical displacement in the capillary regime. Due to the low viscosity and low density of the non-wetting fluid, P_{nw} is constant. The pressure difference in the wetting fluid between 1 and 2, $P_{w,2} - P_{w,1}$, is given by the hydrostatic pressure $\rho_w g h$. This causes a lower capillary pressure at 2 and the front will invade pore 1, if we assume equal pore-throats in 1 and 2.*

is constant along the front. If we consider a slow displacement, the pressure in pore-throat 2 is given by

$$P_{w,2} = P_{w,1} + \rho_w g h, \tag{2.62}$$

resulting in the capillary pressures,

$$P_{\text{cap},1} = P_{nw} - P_{w,1}, \tag{2.63}$$

$$P_{\text{cap},2} = P_{\text{cap},1} - \rho g h. \tag{2.64}$$

We assume that the pore-throats in 1 and 2 are equal. Since the capillary pressure has its lowest value at the tip of the front (at 2), the pore further behind (at 1) will be invaded due to the higher capillary pressure. In other words, gravity tends to "minimize" any height difference between two points along the displacement front in this case. The height difference of the front is called the *front width*, and can be defined as:

$$W = \sqrt{\langle x_f^2 \rangle - \langle x_f \rangle^2}, \tag{2.65}$$

where $x_f(y, t)$ is the position to the wetting/non-wetting fluid interface, at a given vertical distance y at time t, as defined by figure 2.18. The width W is then the standard deviation of x_f.

If the capillary threshold distribution $N(P_c)$, is very sharp, it follows from the above considerations that any initial height difference along the front will be eliminated, and $W \approx 0$. If we assume $N(P_c)$ to be flat as a first order approximation, and increase its width, w_c, the front width W will also increase. The capillary thresholds at 1 and 2 in figure 2.18 follows $N(P_c)$. The probability for invading either 1 or 2 depends not only on P_{cap}, but also on the capillary threshold P_c. When w_c increases, the probability for $P_{\text{cap},1} < P_{c,1}$ and $P_{\text{cap},2} > P_{c,2}$ will increase; thus the front roughness increases. This means that the front width in a gravity stabilized displacement can be exploited to estimate the width of the capillary threshold distribution in the porous medium. A quantitative treatment of this estimation is presented in Auradou *et al.*, [34].

2.5   Simultaneous two-phase flow

All of the flow regimes discussed in the previous section are considered well understood, and have been studied by several authors independently. The common denominator of these studies is that one, and only one, fluid is used to displace a second fluid. Additionally, the experiment or simulation is often terminated after breakthrough. We will refer to these flow regimes as *classical*. In the laboratory or simulation studies of these classical regimes, the popular analogy to oil recovery from underground reservoirs is often claimed. The analogy must of course be considered valid to some extent, but as always, real systems are often more complex. As an extension of previous studies, the main focus of this thesis has been to perform experiments where two phases were injected into a porous medium simultaneously. These boundary conditions should be more similar to what happens deep inside an oil reservoir, and thus take the analogy a step further. The steady-state regime of the experiments has been of special interest. We attempt to answer new questions in a field little explored. The concept of simultaneous two-phase flow is nothing new, in fact it is commonly used in the oil industry to measure relative permeabilities. However, large three dimensional core samples are used, and the experiments does not seek to address the underlaying physics of the complex structures inside. A few experimental studies addressing dynamics and structure do exist, but the systems under consideration have been relatively small.

   We seek in this thesis to answer how pressure and fluid flow relate to the dynamics and structure observed during simultaneous two phase flow. Both the initial and steady-state regime have been considered in a large quasi two-dimensional laboratory model, of length $L = 83$ cm and roughly ~ 213600 pores. In particular we will address how statistical properties as cluster size distributions, cluster orientation and shape relates to measured pressure, flow-rates and saturation. The structural change from the initial to steady-state regime have shown interesting features. Also the effects of using a compressible gas as one of the phases has been investigated. Even though this is an experimental study, we are fortunate to have the possibility of comparison with simulations performed by Ramstad *et al.* at the Complex group, NTNU Trondheim. The experiment/simulation comparison is motivation in its own respect.

2.5.1   Initial transients and steady-state

The classical flow regimes discussed in the previous section must be considered initial transient states. As an example, consider a drainage displacement in the capillary fingering regime. When the invading fluid enters the porous medium, the displacement of defending fluid begins, and the wetting saturation S_w starts to decrease. S_w will continue to decrease until breakthrough. After breakthrough, new non-wetting fluid that enters the medium, will have an open pathway to the outlet through the percolating invasion cluster. As a consequence, no more wetting fluid is displaced, and S_w will reach a constant value. In this way we can define an *invasion phase* before breakthrough, which is a transient state, and a *steady-state* phase after breakthrough. Steady-state is characterized by the vanishing of all partial time derivatives. This means that global pressure, saturation, flow-rate etc. in a given position is constant with respect to time.

   In the classical flow regimes, only invading fluid was injected. It is also possible to have a porous medium initially saturated with defending fluid, and inject both invading and defending fluid simultaneously. When the invading fluid enters the porous media, there will be a background flow field of defending fluid. In all of our experiments the invader has been non-wetting low-viscous air, whereas the defender has been a wetting high-viscous mix of glycerol/water. The invasion phase is in this case defined in the same way as for non-simultaneous flow. The steady-state behavior of simultaneous two-phase flow will be referred to only as steady-state flow. The definition of steady-state however, needs a slight modification.

   The displacement structure in these types of experiments, is at all stages significantly different from that of capillary- or viscous fingering. From a fractal continuous invasion cluster, the introduction of a background flow field, contributes to a high degree of fragmentation of the invasion structure. This is shown in figure 2.19. During the invasion phase, defending fluid is displaced by numerous smaller invasion clusters along a more or less stable front. After breakthrough,
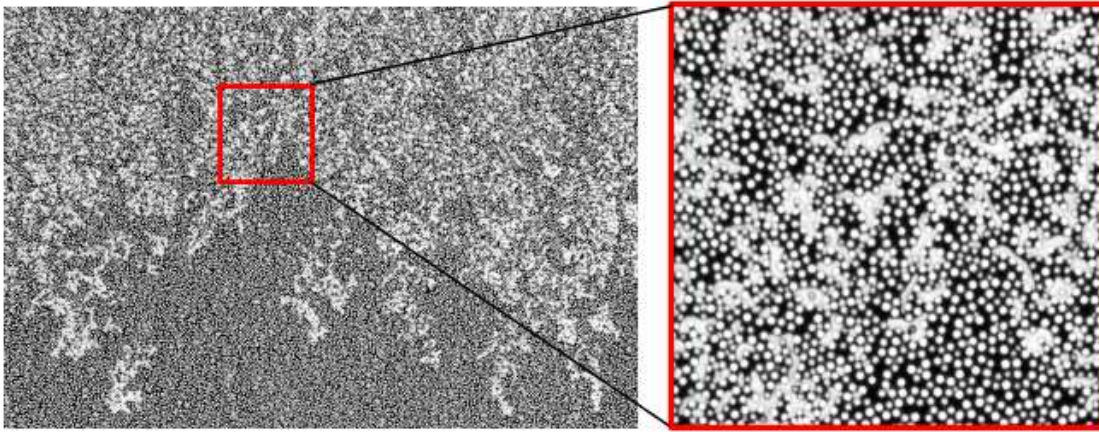
Figure 2.19: *Snapshot of the invasion phase in one of our experiments, performed in the Complex lab (2007). Air (white) and glycerol (black) are injected simultaneously into a porous Hele-Shaw cell, initially saturated with glycerol. In the zoom-in we can see the fragmented air-clusters. The smallest circular shaped white clusters are not air, but 1 mm diameter glass beads that are part of the porous Hele-Shaw cell.*

the average global saturation approaches a constant value, and the structure is characterized by a flow of fragmented invading clusters, mixed in a background field of defending fluid. As an invading cluster moves through the porous medium, it can be deformed in many ways before it reaches the outlet. This may be by further fragmentation, merging with other clusters, trapping in the porous medium etc. The result is a continuous change in flow velocity, pressure and saturation *locally*. In this case we say that steady-state is reached, when the partial time derivatives of time averaged *global* flow-parameters become zero. As an example we have shown in figure 2.20 saturation and pressure development as a system goes from the initial-state to steady-state.
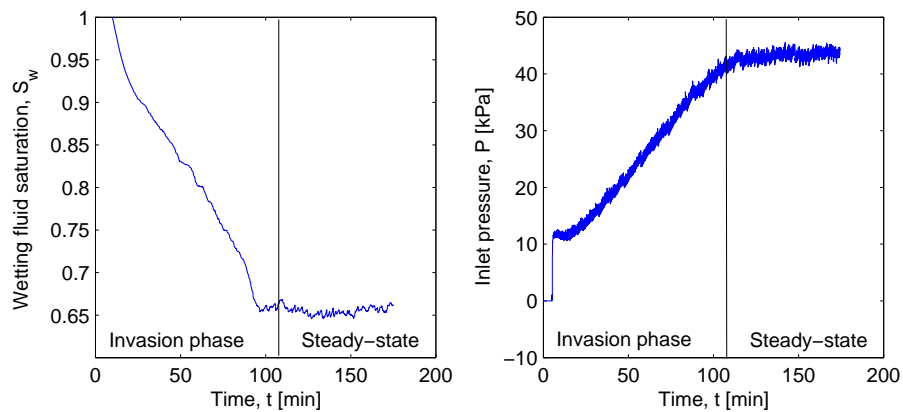

Figure 2.20: *Wetting fluid saturation S_w (to the left), and inlet pressure P (to the right), as a function of time t. The curves are data from the experiment described in figure 2.19. Some time after breakthrough at $t \approx 110$ min, both global saturation and pressure reaches a constant value, and a steady-state is obtained.*

2.5.2 The competition of imbibition and drainage

The main structural difference between classical regimes and simultaneous flow is the existence of multiple independent invasion clusters, due to fragmentation. When the invasion clusters extend a certain length into the model, *snap offs* can occur. By snap off we mean that imbibition occurs somewhere behind the tip of a non-wetting cluster, and disconnects a part of it. We will see that snap offs introduce a characteristic length scale of the largest non-wetting clusters. Due to the simultaneous flow of invading and defending fluid, there is a competition between drainage and imbibition. The snap offs caused by imbibition results in fragmentation and splitting of the invading non-wetting cluster. The flow of viscous defending fluid is the reason for the snap-off
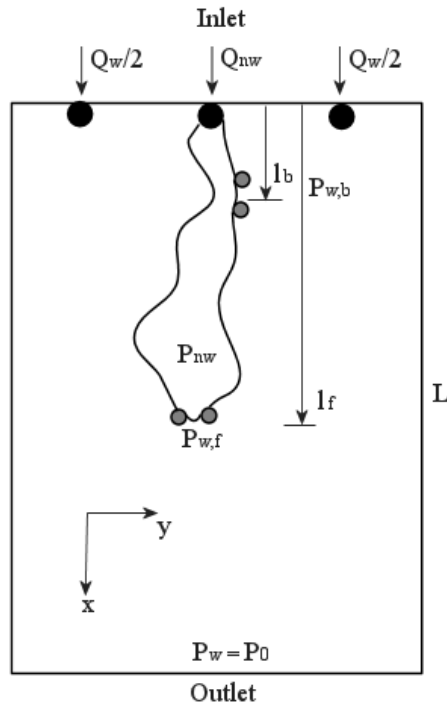

Figure 2.21: *Three inlet nodes are shown, two of which produces a background flow of wetting fluid. The flow-rate is $Q_w = Q_w/2 + Q_w/2$. Non-wetting fluid is pumped in through the middle inlet node, at a flow-rate Q_{nw}. The invasion cluster is connected over a length l_f. At the distance l_b the wetting fluid pressure is $P_{w,b}$. The corresponding pressure at l_f is $P_{w,f}$. At the model outlet $x = L$ the pressure is P_0. Further we assume that the non-wetting fluid pressure P_{nw} is constant.*

effect. This flow contributes with a pressure gradient assumed to be proportional to the flow-rate, by Darcy's law

$$\nabla P_w = -\frac{\mu_w}{k_w^r K A} \mathbf{Q}_w. \tag{2.66}$$

As an example we imagine a model porous medium with three inlet nodes as shown in figure 2.21. High-viscous wetting fluid and low-viscous non-wetting fluid is pumped into every other node to get simultaneous flow. The pressure on the wetting side of a pore-throat located at the tip of the invasion cluster is $P_{w,f}$. The wetting pressure in a pore-throat further behind, located in a narrow part of the air cluster, is designated $P_{w,b}$. Due to the imposed pressure gradient, $P_{w,f}$ and $P_{w,b}$ depend on the distance x from the inlet

$$P_w(x) = P_0 + |\nabla P_w|(L - x) \tag{2.67}$$
$$P_{w,f} = P_0 + |\nabla P_w|(L - l_f) \tag{2.68}$$
$$P_{w,b} = P_0 + |\nabla P_w|(L - l_b) \tag{2.69}$$
$$l_f > l_b \Rightarrow P_{w,f} < P_{w,b}, \tag{2.70}$$

where P_0 is the outlet wetting pressure and L the length of the model. Air is used as the non-wetting fluid, hence the non-wetting fluid pressure P_{nw} is considered constant with respect to

position. It then follows that the capillary pressure P_{cap} decreases from the tip of the cluster to the inlet node, and that $P_{cap,f} > P_{cap,b}$. This implies that there are more curvature of the meniscus at the pore in front than at the pore further behind. If we look at the cluster in figure 2.21, only drainage steps have taken place. We would expect that the probability for imbibition increases as the cluster grows longer, and the length $l_f - l_b$ increases. In this case, both the distribution of critical capillary pressures for drainage $N(P_c^D)$, and imbibition $N(P_c^I)$ become important. We designate w_c^D and w_c^I respectively, as the width of the two distributions. Because of the geometry of our beads, the critical curvature for imbibition is close to the pore-throat outlet, and hence very small. Based on this, we follow the lines of [39] and assume that $N(P_c^I)$ is sharply peaked around a mean value $\bar{P}_c^I \approx 0$, with $w_c^I \approx 0$. A schematic representation of $N(P_c^D)$ and $N(P_c^I)$ is given in figure 2.22. We assume that the distribution of critical drainage pressures is a Gaussian
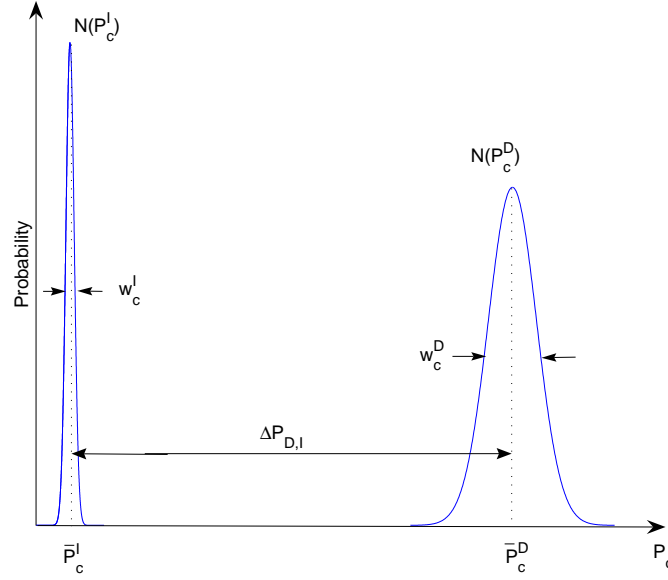

Figure 2.22: *Schematic distributions $N(P_c^I)$ for imbibition and $N(P_c^D)$ for drainage. The width of each distribution is w_c^I and w_c^D respectively. The distance between the average critical pressures, $\bar{P}_c^I$ and $\bar{P}_c^D$, is designated $\Delta P_{D,I}$.*

located at the mean value $\bar{P}_c^D$. Since no imbibition has taken place in figure 2.21, $P_{cap,f} \sim \bar{P}_c^D$ and $P_{cap,b} > \bar{P}_c^I$. If we start to increase Q_w, the pressure gradient surrounding the cluster will increase. Hence $P_{cap,b}$ is tuned towards the critical value for imbibition $\bar{P}_c^I$. When the pressure gradient in eq. 2.66 is sufficiently large, we will expect imbibition to occur whenever,

$$P_{cap,b} < \bar{P}_c^I. \tag{2.71}$$

During this imbibition step, the wetting fluid can reconnect through narrow parts of the invasion cluster, and we have a snap off. If we still assume that $P_{cap,f} \sim \bar{P}_c^D$ eq. 2.71 gives,

$$P_{cap,f} - P_{cap,b} > \bar{P}_c^D - \bar{P}_c^I \tag{2.72}$$

$$P_{nw} - P_0 - |\nabla P_w|(L - l_f) - P_{nw} + P_0 + |\nabla P_w|(L - l_b) > \Delta P_{D,I} \tag{2.73}$$

$$|\nabla P_w|(l_f - l_b) > \Delta P_{D,I} \tag{2.74}$$

$$l_f - l_b > \frac{k_w^r K A}{\mu_w Q_w} \Delta P_{D,I}, \tag{2.75}$$

where $\Delta P_{D,I} = \bar{P}_c^D - \bar{P}_c^I$. For a given porous medium and constant wetting conditions, $\Delta P_{D,I}$, A and K are constants. Snap-offs and the degree of fragmentation will then depend on the viscosity, relative permeability and flow-rate of the wetting fluid. For a high-viscous wetting fluid, we will expect more snap offs and smaller clusters when the wetting flow-rate is increased. Based on eq. 2.75, it is reasonable to assume that there exists an upper length scale,

$$l_c = l_c(k_w^r, \mu_w, Q_w), \tag{2.76}$$

over which invading clusters can stay connected. The probability of finding clusters that extends a length $l \gg l_c$, will be very small.

In some sense, there is an analogy between gravitational flow and simultaneous two-phase flow. Part of the discussion of snap offs presented above, is based on the analysis done by Måløy *et al.* [39]. They studied snap offs caused by buoyancy. Imagine that the model in figure 2.21 is tilted from the horizontal to the vertical direction in the field of gravity. We assume that the outlet is at the top[5]. Further we set the wetting flow-rate $Q_w = 0$. Also in this case $P_{w,b} > P_{w,f}$, but the difference is now given by the hydrostatic pressure drop. The condition for snap off becomes,

$$l_f - l_b > \frac{\Delta P_{D,I}}{\Delta \rho g}, \tag{2.77}$$

where $\Delta \rho$ is the density difference between the fluids. If we compare eq. 2.75 and eq. 2.77, the former equation is the most complicated. Gravity is a body force that acts uniformly, independent of flow parameters. The influence of a background flow field will depend on several parameters, some of which can change during the flow. Vedvik *et al.* comments briefly the topic of buoyancy and viscous pressure gradients in [36]. They study the structural change of a non-wetting invasion cluster, as the flow-rate of a surrounding viscous fluid is increased. The structure of the cluster for high flow-rates is very similar to figure 2.19.

The viscous background field does not only contribute to the snap off of invasion clusters during simultaneous flow. The dynamics displayed is rich and complex. The fate of invasion clusters much below l_c is highly undecided. Some clusters get trapped in the porous medium, whereas others migrate in the direction of flow. Trapped clusters can be mobilized, either by increasing pressure gradients, or by merging with migrating clusters. But then again, if a merging cluster grows to large it will be snapped off and so on. Migration is the process in which a cluster moves without changing its volume. Thus, for each defending pore drained by an invading cluster, a pore belonging to the invading cluster is imbibed by the defending fluid. The result of several migration steps is that the invading cluster moves, and perhaps also changes shape. As for snap offs, a migration step can be studied by a simple example, as shown in figure 2.23. We consider an invasion cluster of constant pressure P_{nw}, that extends a length $l < l_c$ in the direction of flow. The cluster is wide enough to prevent an imbibition step from causing further snap off. The pressure difference $P_{w,b} - P_{w,f} > 0$ of two pores separated by a distance l, is assumed to follow eq. 2.66. The cluster in figure 2.23 will be trapped if the capillary forces balance the viscous forces. We still assume that the distributions of critical drainage and imbibition pressures follow figure 2.22. The balance of viscous and capillary forces depend on the width w_c^D of the distribution $N(P_c^D)$. For a trapped cluster, the capillary pressure of every pore must lie between the two distributions $N(P_c^I)$ and $N(P_c^D)$. For the particular pores shown in figure 2.23 we get

$$P_{\text{cap},f} - P_{\text{cap},b} < \bar{P}_c^D - w_c^D - (\bar{P}_c^I + w_c^I) \tag{2.78}$$

$$\nabla P_w l < \Delta P_{D,I} - w_c^D - w_c^I. \tag{2.79}$$

If we still assume that $w_c^I \approx 0$, eq. 2.79 reads

$$|\nabla P_w| l < \Delta P_{D,I} - w_c^D. \tag{2.80}$$

---

[5]This assumption is crucial. If the outlet was placed at the bottom, gravity would have stabilized the flow as discussed in section 2.4.5.
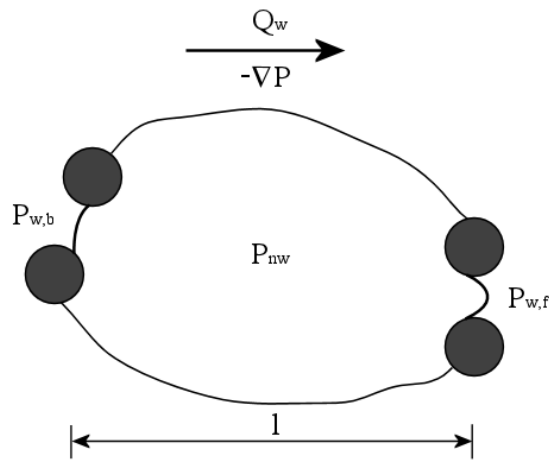
Figure 2.23: *A snapped off non-wetting cluster in a viscous background field. The flow direction and pressure gradient of the wetting fluid are indicated. Due to the wetting pressure difference $P_{w,b} - P_{w,f} > 0$, caused by $-\nabla P$, migration might occur through the pores shown.*

If the capillary forces can not withstand the viscous ones, migration will happen. Since the curvature of the menisci will decrease in the direction of higher wetting fluid pressure, see figure 2.23, the pores furthest behind will be most susceptible for imbibition. Pores in the middle part of the cluster are more likely to be somewhere in between $N(P_c^I)$ and $N(P_c^D)$, whereas pores along the front part will be most susceptible to drainage. Thus, it is reasonable to expect that the background field will shape and elongate invasion clusters in the direction of flow. Based on the difference in curvature, we can identify pairs of drainage/imbibition pores where migration might occur. Note that the drainage and imbibition step is linked in the case of migration, one cannot occur without the other. Migration will take place, if there is a drainage/imbibiton pair at the cluster perimeter with a capillary pressure difference that exceeds the corresponding difference in threshold pressure. If we assume this pair to be the pores shown in figure 2.23, migration will occur when the inequality of eq. 2.80 is violated. We would expect that when the width w_c^D decreases, only larger clusters would be able to migrate, due to the larger capillary pressure difference needed. On the contrary, if w_c^D is increased smaller clusters will also be able to migrate.

Studies of fluid displacement incorporating migration caused either by buoyancy or viscous pressure gradients have been done. Schmittbuhl *et al.* [43] modified the IP-algorithm to also include migration effects caused by buoyancy, during displacement in a rough self-affine geometry. Payatakes *et al.* [44] have simulated the migration of single non-wetting clusters in a background flow field of wetting fluid.

2.5.3 Cluster size distributions

The distribution of clusters in a system, can provide important information of both statistical and dynamical properties. To the best of our knowledge, no experimental studies exist that address the cluster distributions during simultaneous flow.

In this thesis we want to study how the steady-state distribution of non-wetting clusters are affected by changing the flow-rate of the viscous wetting fluid. This flow-rate Q_w is our only tuning parameter. From the discussion of snap-offs, we will expect a cutoff for larger clusters. By this cutoff, we mean that the distribution would drastically decay to zero as the clusters reach some critical size. We do believe that the size of the largest clusters is controlled by a length scale dependent on the properties of the wetting fluid. The question of whether this length scale also depends on the system size is an important one. Another interesting question is how much

small and medium clusters are affected by a change in Q_w. We could e.g. imagine that the only difference in the distributions for different Q_w, would be the cutoff of larger clusters. Another possibility is that the whole distribution changes shape, that is, both small, medium and large clusters are affected by a change in Q_w.

We will also consider, for a constant Q_w, how the distribution changes in the transition from the invasion phase to steady-state. This was studied numerically by Ramstad *et al.* [8], but with different boundary conditions. We will present some of their findings in the next section.

2.5.4   A review of previous studies

Steady-state flow is often mentioned in the literature in connection with the so-called "Penn State"-method, [20], [21]. This method, invented by Osoba *et al.* (1951) and named after Pennsylvania State University, is used to measure relative permeabilities. Briefly explained, it consists of injecting two phases simultaneously into a porous sample. When steady-state is reached, the pressure drop of the two phases over a given distance in a central part is measured. Flow-rates, viscosities and absolute permeability are assumed to be known, and the relative permeabilities are found from the generalized Darcy equations, eqs. 2.32-2.33. The porous media considered in such measurements, are often large three-dimensional core samples. It is obviously hard to extract information of the fluid structure in this case.

The experimental procedure suggested by the "Penn State"-method, has been around since the early 50's. However, the first to do a pore-scale "microscopic" study of steady-state flow, was Payatakes (1995) *et al.*, [17], [18]. As a model porous medium, they used a one-layer network model. The network consisted of chambers (pores) and tubes (pore-throat), etched in glass. The size of the model was 16×7 cm, consisting of 11300 chambers. The chamber and tube diameters were picked from flat distributions in the μm range. The boundary conditions used were six inlet nodes and three outlet nodes. Wetting and non-wetting fluid was fed simultaneously into every other inlet node. The separate flow-rate of each fluid was constant. In their experiments the viscosity ratio ($0.66 \leq M \leq 3.35$), wetting flow-rate ($0.0097 \leq Q_w \leq 0.97[\text{ml/min}]$) and non-wetting flow-rate ($0.0024 \leq Q_w \leq 2.7[\text{ml/min}]$) were the tuning parameters. In each experiment they measured relative permeabilities based on the "Penn State" method. The displacement structure was recorded visually through an imaging device. One important observation they made, was that the wetting fluid percolated the model in all experiments. This happened through a changing network of connected pathways and also wetting films. The wetting properties were kept constant at a static contact angle of $\sim 40°$, in all experiments. Based on the structure dynamics through the range of tuning parameters, four steady-state flow-regimes were suggested:

- LGD, *large ganglion*[6] *dynamics*: The non-wetting fluid is disconnected in the form of independent clusters. The mean size of moving clusters is ~ 10 pores. The total cluster population consists of both moving and trapped clusters, whose interaction is complex. Moving clusters can become trapped when encountering a difficult passage, or they can be snapped off into smaller clusters. These clusters, being shorter, can become trapped again. On the other hand, moving clusters can collide with other clusters, either moving or trapped, and continue to move. This regime is found for small Ca-numbers.

- SGD, *small ganglion dynamics*: This regime is reported very much similar to LGD. However, the mean size of moving clusters in this case is substantially smaller than 10 pores. It is emphasized that there is no sharp limit between SGD and LGD. The transition from LGD to SGD occurs for increased Ca-numbers and decreased wetting saturation.

- DTF, *drop-traffic flow*: Most of the non-wetting fluid is disconnected into moving clusters of size comparable to a pore. The clusters are formed through vigorous snap-offs and fragmentation, characteristic of high-Ca flows.

---

[6]In our terminology, ganglion means cluster.

- CPF, *connected pathway flow*: For relatively high-Ca values and small wetting saturations, both phases flow through separate channels during steady-state. The boundary between a wetting and non-wetting channel is influenced by DTF and SGD. The connected pathways are reported to be rather stable, and they are stabilized further with increasing flow-rates.

The regimes described above illustrate that the dynamics during steady-state are truly rich, and non-trivial. One of the main objectives of Payatakes *et al.* was to study how the pore-scale dynamics related to the measured macroscopic relative permeabilities. Based on their findings, some of the long standing assumptions and rather uncritical use of relative permeabilities in the oil industry, were sharply addressed. First of all there seems to be a presumption that non-wetting fluid only flows through connected pathways in the porous medium, and that snapped off clusters are trapped[7]. We can already conclude that this is not the case, based on the discussion in this section. Furthermore, it is not clear in the literature, which parameters will affect the flow and the relative permeabilities significantly. Simultaneous two-phase flow is of key importance to the oil industry. Relative permeabilities are usually measured under steady-state conditions, and then applied to predict the behavior of transient displacements. Payatakes states that this procedure is highly questionable.

When it comes to connected pathway flow, it was observed only for relatively high-Ca values, and favored by a combination of a high viscosity ratio and low wetting saturation. In all other cases, non-wetting fluid moved through the porous medium in disconnected clusters. The relative permeabilities were found to correlate strongly with the flow-regimes described above. The experimental results showed that k_w^r and k_{nw}^r depended strongly on S_w, Ca, Q_w, Q_{nw} and M.

A review of the full study [17] would be to elaborate to be included here. However, the following quote emphasizes part of the conclusion: "*Indeed, it is neither consistent nor satisfactory to rely on a model in which the parameters that are used to predict the flow-rates of the two fluids depend very strongly on the flow-rates themselves, as well as on a number of other flow-related quantities.*" This quote suggests that a revision of the conventional use of eq. 2.32-2.33 and the concept of relative permeabilities is warranted, or that other methods must be applied to study steady-state flow.

For the study of simultaneous flow, there exists no simple statistical algorithm along the lines of IP and DLA. Network models based on Washburn's equation[8], [37], are often used. The network consists of *nodes* (pores) interconnected by *tubes* (pore throats) of different diameters. Payatakes *et al.* (1996) [38] and Knudsen *et al.* (2002) [25] have both done network simulation studies on the effects of saturation, capillary number and fractional flow during steady-state. The model used by Knudsen *et al.* was a further extension of the network simulator developed by Aker *et al.* (1998) [45]. The extension consisted in applying what is called *biperiodic boundary conditions* in the direction of flow. Whenever fluid left the network "outlet", it re-entered the network "inlet". In this way the fluids were left to run in a continuous loop. Using these boundary conditions, they were able to simulate a steady-state environment. The cluster size development in a steady-state environment was studied by Ramstad *et al.* (2006), [8]. They used a network model similar to that of Aker and Knudsen, with the same boundary conditions. The networks under consideration had sizes up to 1024×1024 nodes. In all simulations the surface tension and the viscosity ratio were kept constant, $\gamma = 30$ mN/m and $M = 1$ respectively. There is an important difference between these simulations and the way experimental models normally are devised. Initially the simulation network is segregated into one region of wetting fluid and one region of non-wetting fluid. The fluid volume in each region is set according to pre-selected saturations S_w and S_{nw}. Flow is then induced by applying a varying pressure gradient such that the global flow-rates Q_w and Q_{nw} are kept constant. In an experimental model, it is often the other way around; the flow-rates are pre-selected by a syringe-pump and the pressure gradient and saturation varies accordingly.

---

[7]The question whether this assumption is made to justify the use of the generalized Darcy equations, does come to mind.

[8]The Washburn equation for capillary flow in a tube, relates flow-rate to pressure: $Q = -\frac{K\gamma}{\mu_{\text{eff}}l}(\Delta P - P_{\text{cap}})$.
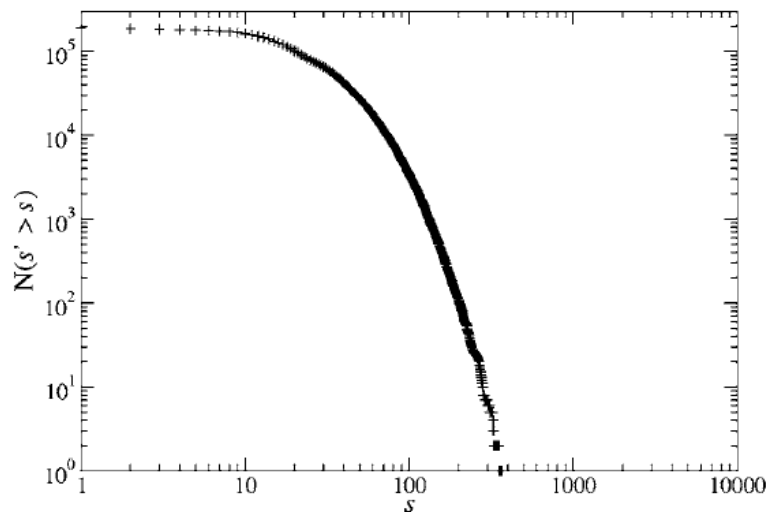
Figure 2.24: *Cumulative distribution $N(s' > s)$ of non-wetting clusters at steady-state, by Ramstad et al. [8]. The non-wetting saturation and capillary number are given as, $S_w = 50\%$ and $Ca \sim 10^{-5}$ respectively. The clear cutoff is evident.*

Figure 2.25 shows the transition from the invasion phase to steady state in one of the simulations by Ramstad *et al.*. Because of the biperiodic boundary conditions and the initial segregation of fluids, drainage and imbibition are observed separately during the first part of the displacement. After a while, the drainage front catches up with the imbibition front. At this point there will be a competition of both drainage and imbibition. As discussed previously in this section, clusters will experience snap offs and fragmentation. In the steady state regime, no signature of initial displacement is left, and the flow is characterized by the movement of independent clusters. This is very much similar to what we find in our experiments.

Ramstad *et al.* finds in their study that for capillary dominating flows, there exists a critical saturation[9] of the non-wetting fluid, $S_c \sim 0.69$. Above this value, the non-wetting cluster size distribution is found to obey a power-law. Based on this power-law, an analogy to percolation theory is made. For $S_{nw} < S_c$, they observed a cutoff of larger clusters in the distributions. This is shown in figure 2.24. The observed cutoff behavior is highly relevant for our studies. We will return to this discussion in chapter 4. As stated in the introduction to this section, we are fortunate to be able to compare our experimental results with the network model described here. In recent time, the simulation model has been further developed to mimic our experimental boundary conditions.

Before we present our results, we turn to a description of the experimental setup and instrumentation in the next chapter.

---

[9]The critical saturation is found to somewhat vary with Ca, and its accurate value is difficult to establish.
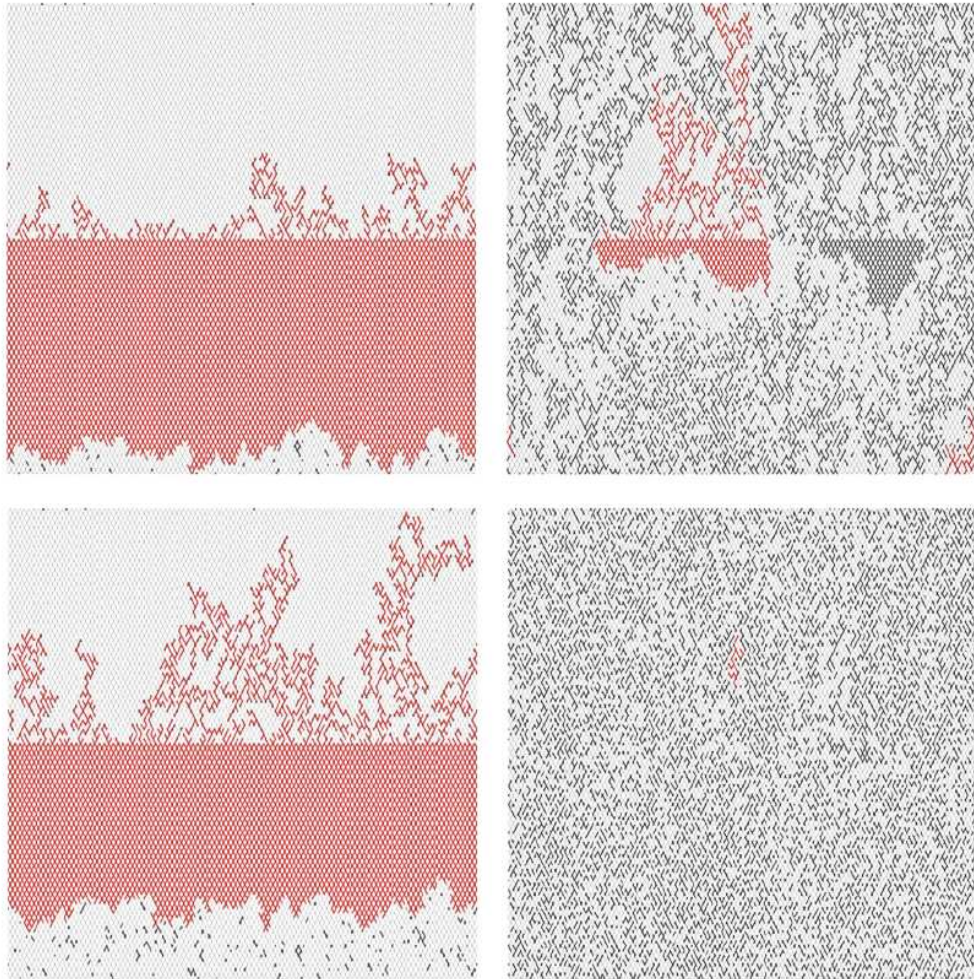
Figure 2.25: *Network simulation by Ramstad et al. [8], at viscosity match, saturation match and low Ca-number, $M = 1$, $S_w = 50\%$ and $Ca \sim 10^{-5}$ respectively. Upper left: Inital stage of invasion. Non-wetting fluid colored red. Lower left: Mid stage of invasion. Non-wetting fluid colored red. Upper right: Last stages of the invasion phase. Non-wetting fluid colored gray, and the largest non-wetting cluster colored red. Lower right: Steady-state regime. Non-wetting fluid colored gray, and the largest non-wetting cluster colored red. Due to the boundary conditions and initial segregation of fluids, the first part of the invasion phase consists of drainage in the upper region and imbibition in the lower region. The mixing of both fluids and the small clusters is characteristic for the steady-state regime. In fact, the lower right image is visually very similar to our experiments.*

Chapter 3

Experimental setup and instrumentation
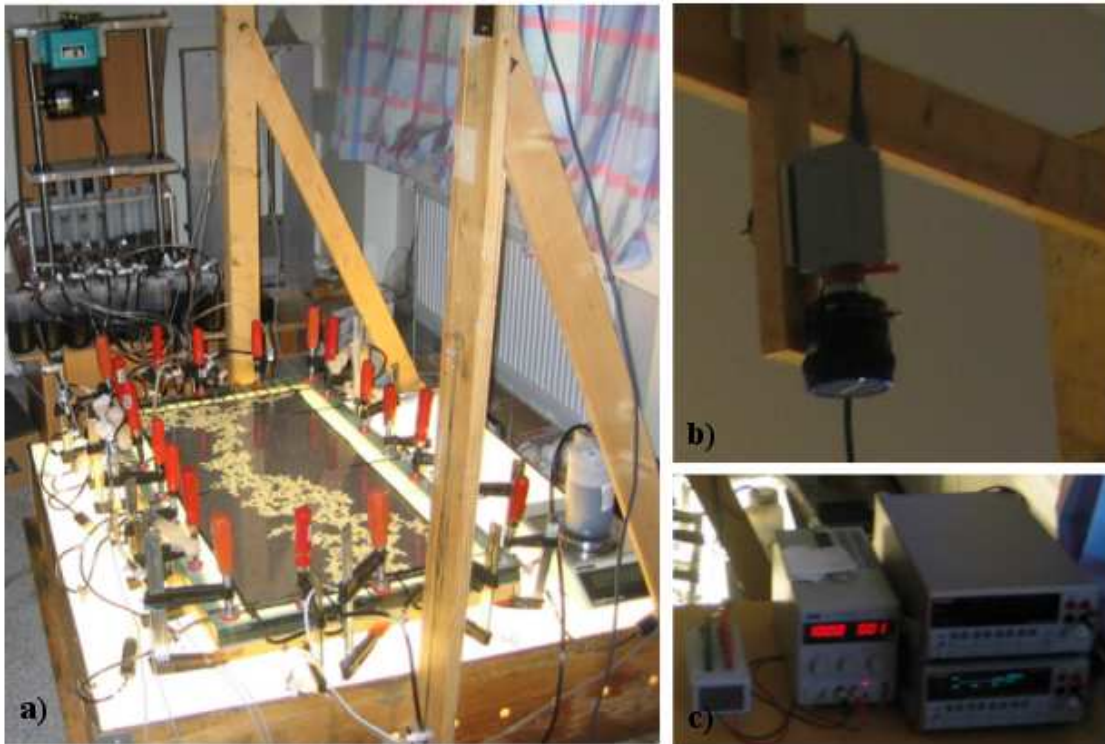
Figure 3.1: *Pictures of the experimental setup: **a)** Pump system, lightbox and flow model. **b)** Pixelink digital camera. **c)** Multimeter and power supply for excitation of pressure sensors.*

As always when doing experimental work, much time is dedicated to instrumentation and making the setup work properly. This is also the case here, and should be well supported by figure 3.1. In this chapter we will give a description of the experimental model and setup used in this thesis. The main part of the setup, namely the model porous medium, is by no means a new concept. It was first constructed by Måløy *et al* [1] in the 80's, and has been used at the Complex group for a great diversity of flow experiments ever since [2], [3], [4]. The last part of this chapter will be concerned with the instrumentation, image- and data treatment.

3.1 The quasi 2D flow model

For all the experiments we use a quasi two dimensional model, where the height of the model is much smaller than the length and width. Of course real models can never be strictly two dimensional, hence the term quasi. One can also study flow in a 3D model, but this introduces several new complications. First of all, visualization of a complex 3D geometric structure inside a porous medium is much more difficult than in the 2D case. In general 3D models are not transparent. A common approach to obtain transparency, is to use a saturating fluid with an index of refraction that matches the porous media. However, an image from one side of a 3D model would just be a projection of the exterior, and give no information of how the structure looks inside. Different studies have been done, concerning visualization techniques and two-phase flow in 3D porous media [5], [9], [10], but this is not the selected approach in this thesis. Yet another factor in 3D models is gravitational forces, which always have to be accounted for. In a 2D case these forces are ignored assuming that the model is kept in a horizontal position.

Our quasi 2D model porous media consists of a mono layer of glass beads randomly distributed between two rectangular sheets of contact paper. This will be referred to as the porous matrix, see figure 3.2. A layer of silicone glue is applied in between the contact papers at the boundary and defines the system size. The porous matrix is part of a bigger model. A pump system, consisting of fifteen syringes pumps fluid/air into the porous matrix. The fluid/air enters the matrix through inlet channels in an overlaying plexiglass plate. The plexiglass plate and porous matrix is placed in between a heavy glass plate and a pressure cushion, to prevent bending and thereby buoyancy effects, as shown in figure 3.5. Fluid/gas leaves the porous matrix through a wide outlet channel. The outlet channel has a tube connection to a reservoir open to atmospheric pressure. A balance is then used to continuously measure the extracted fluid mass in this reservoir. The flow model is placed on a leveled light-box, which in addition to illuminate the porous matrix, contains a rack for a digital camera.

Four flow through pressure sensors are placed along the model. Additionally, a thermistor is placed at the model outlet, in direct contact with the porous matrix. The pressure sensors, thermistor, camera and balance are all computer monitored.

In the following subsections, a description of the flow model and all of is components will be given. Sections 3.1.1-3.1.2 are fairly detailed, and are intended as a recipe for the construction of the flow model. For the reader interested only in a quick description of the setup, the resume given above, together with figure 3.5 and 3.6 should suffice.

3.1.1 Making of the porous matrix

As mentioned in the previous section, the porous matrix consists of a sandwich of contact paper and glass beads. Here we describe how it is made.

A piece of contact paper is rolled out on a table, and cut to a suitable length according to the rest of the model (560×980 mm). A marker is then used on the uncoated side of the paper to draw up the system size and the tube connectors, as shown in figure 3.3. The markings are then taped with double coated tape, both to reinforce the spots where the fluid enters the porous matrix and to make the matrix stick to the plexiglass plate. After removing the coating of the contact paper, also revealing the markings on this side, 1 mm in diameter glass beads[1] are pored over the paper several times. In the end, excess beads are gently brushed off until a nice random monolayer of beads is obtained. The next step is to apply the silicon glue on top of the beads along the marked lines (420×850 mm). Finally the matrix is glued together by the second sheet of contact paper, as shown in figure 3.2. After the silicone glue is smeared out properly, a scalpel is used to cut out the markings so that the fluid can flow from the tube connectors and into the porous matrix. To finish up, the matrix is glued to the plexiglass plate by double coated tape. The two components are then mounted in the flow model, see figure 3.5, and left to dry overnight.

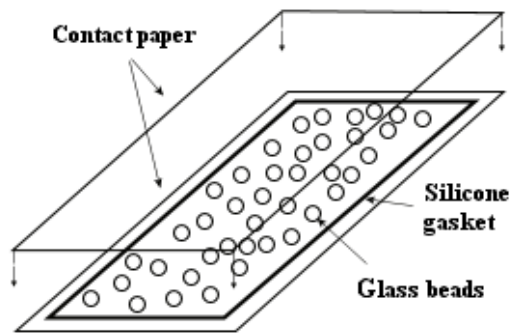[1]The beads used are fairly mono disperse.

Figure 3.2: *The porous matrix.* 1 *mm in diameter glass beads are randomly distributed between to layers of contact paper, and sealed off by a silicone gasket. The gasket has the dimensions* 420×850 *mm.*
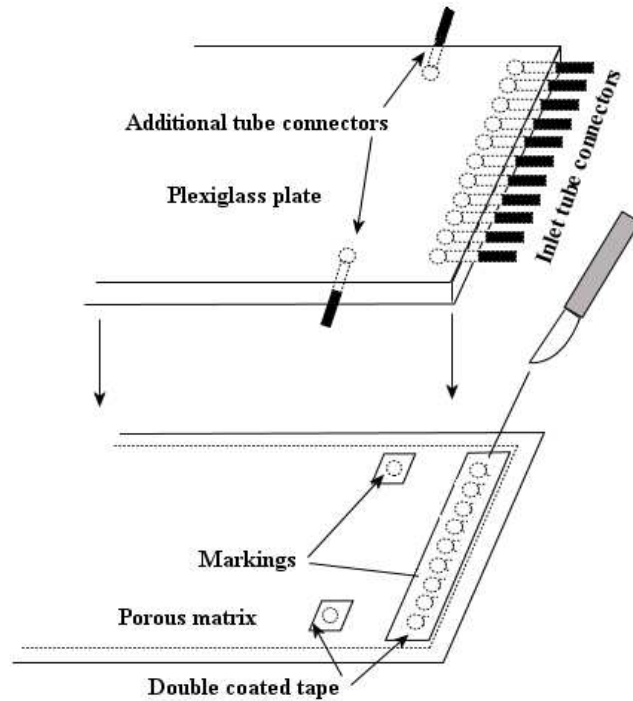

Figure 3.3: *After the porous matrix is sealed off, cuts are made along the markings, so that the fluid can flow through the tube connectors in the plexiglass plate and into the porous matrix. After the cuts are made, the porous matrix is glued to the plexiglass plate by double coated tape.*

3.1.2 Supportive parts of the porous matrix

To get fluid and gas from the syringes into the porous matrix, we use a plexiglass plate of the dimensions $980 \times 560 \times 15$ mm. The plate has 15 inlet tube connectors, 4 outlet tube connectors and 8 additional tube connectors. A tube connector consists of two perpendicular channels in the plexiglass plate. One from the end of the plate where the plastic tubes are connected, and one from underneath the plate where the fluid or gas enters/leaves the porous matrix. To attach the plastic tubes, a hollow brass plug is fitted into each plexiglass channel.

The eight additional tube connectors of the plexiglass plate are, among other things, used to attach flow-through pressure sensors. The attachment of a pressure sensor is shown in figure figure 3.4. With this setup, one is able to screen the sensor from the model by simply close it off with the three-way vent and opening the two-way vent. Screening of the pressure sensor is important because it can be damaged if exposed to extreme pressures. This can occur when the model is flushed between experiments.

All the additional tube connectors of the plexiglass plate, including those who have a pressure sensor attached, are connected to syringes. In this way, one has the ability to extract air bubbles, excess fluid and so on from the porous matrix. A schematic overview of the plexiglass plate and the porous matrix is shown in 3.6.
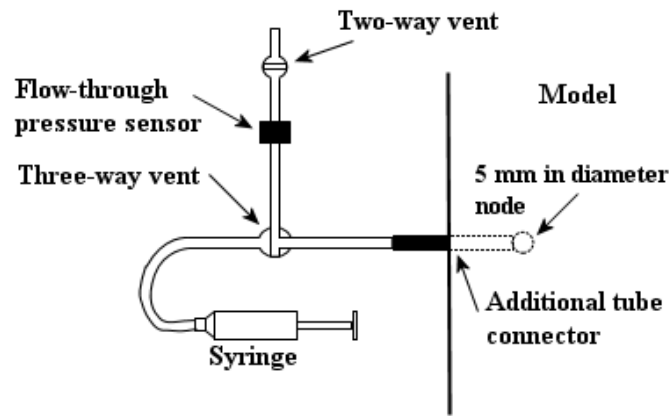
Figure 3.4: *A tube is connected to the pressure sensor, and sealed off by a two-way vent. When the vent lever is perpendicular to its tube connectors, no fluid can flow through. The sensor is then connected to a three-way vent. The remaining tube connectors of the three-way vent are connected to a syringe and to the model respectively. The three-way vent has four lever positions. The first lets fluid flow through all tube connectors. The second blocks out the connector perpendicular to the two parallel connectors. The last positions only allows fluid to flow through perpendicular tube connectors. During experiments the tube from the pressure sensor to the model is filled with fluid. The sensor is in contact with the porous matrix through a 5 mm diameter node.*

As mentioned earlier the porous matrix is resting on a pressure cushion, see figure 3.5. As a base for the cushion a 30 mm thick plexiglass plate is used, with two holes drilled through it so that water can flow in and out. Along the rim of the plate, a thick layer of vacuum grease[2] is smeared out, and a mylar film is placed on top. To fix the mylar film we used a rectangular aluminum frame with an O-ring, as shown in figure 3.7. A diffusion proof film is applied on top of the cushion to prevent any water from diffusing into the porous matrix. It is important to mention that the film must be applied with some slack. A tight film can cause high stresses along the rim when the cushion is filled with water, and will often result in leakage.

After the cushion is filled with water, the next step is to apply pressure. This can be done by the help of gravity. The siphon principle is used to fill a bottle with water from a reservoir, in our case a 10 liters bucket with a tube connection to the bottle. To ensure atmospheric pressure at the water/air surface in the bottle, a little hole is drilled through the cap.

---

[2]Along with tissue paper, vacuum grease is a must when building and working with this kind of setup. Tissue paper to clean up the unavoidable spilling of fluid and vacuum grease to prevent leakage when surfaces are sealed together.
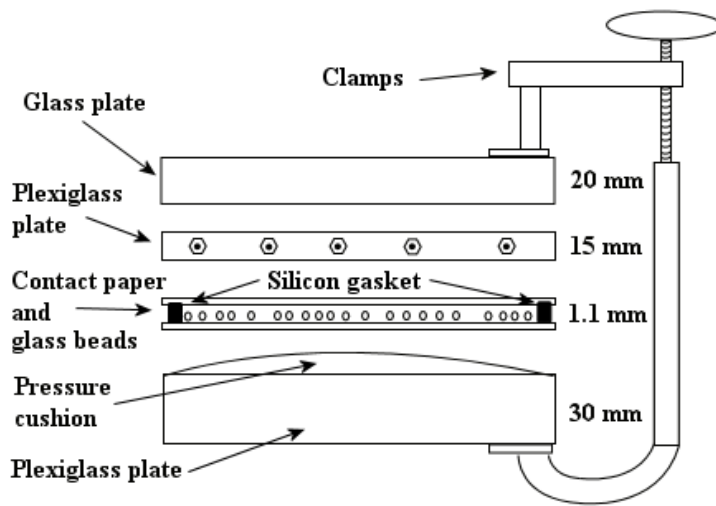
Figure 3.5: *Schematic cross section of the flow model. The porous matrix rests on a pressure cushion, and has on top a plexiglass plate with channels and tube inlets so that the fluid can flow into the matrix. The heavy glass plate and the clamps prevents bending of the model.*
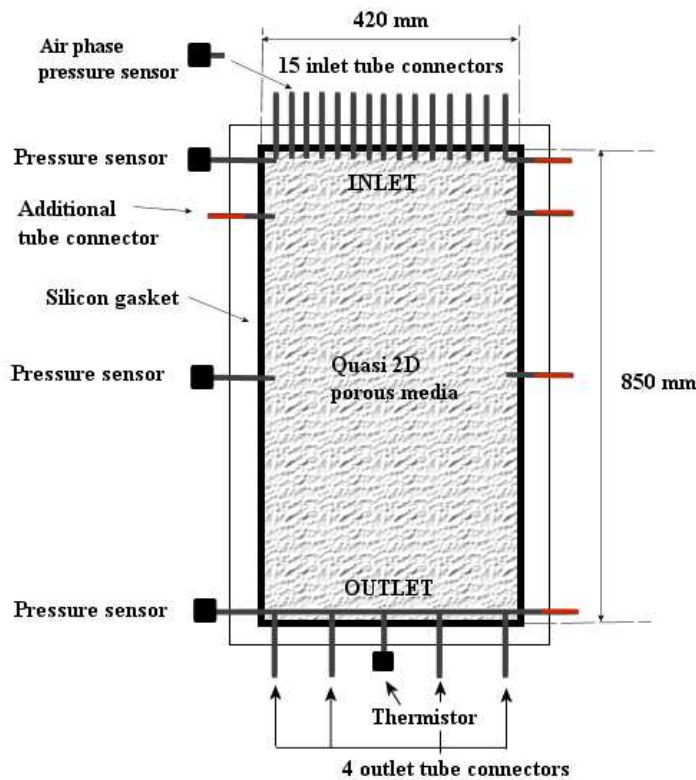

Figure 3.6: *Overview look of the flow model. There are four pressure sensors connected to the setup. Three of these are connected to the model. The last one is connected to one of the syringes that injects air. There is also a thermistor mounted at the model outlet, so that the temperature can be monitored. The additional tube connectors (marked red) are a practical convenience used to extract or refill fluid or gas.*

The bottle is then hoisted up to the ceiling approximately 2.5 meters in vertical distance from the cushion, see figure 3.8. The pressure in the cushion is then given by the equation:

$$P_{\text{cushion}} = P_0 + \rho g z_1, \tag{3.1}$$

where P_0 is the atmospheric pressure and z_1 the height difference from the zero-level. It is evident from eq. 3.1 that elevating the bottle creates overpressure in the cushion. This pressure is in is in the order[3] of 2.5 mH$_2$O. For the fastest experiments it was observed that the pressure in the

---

[3]1 mH$_2$O is the pressure in the bottom of a 1 m water column with reference pressure, $P_0 = 0$ Pa. From eq. 3.1 we see that this corresponds to: 1 mH$_2$O $\approx$ 1000 kg/m^3 $\cdot$ 9.81 m/s^2 $\cdot$1 m = 9810 Pa
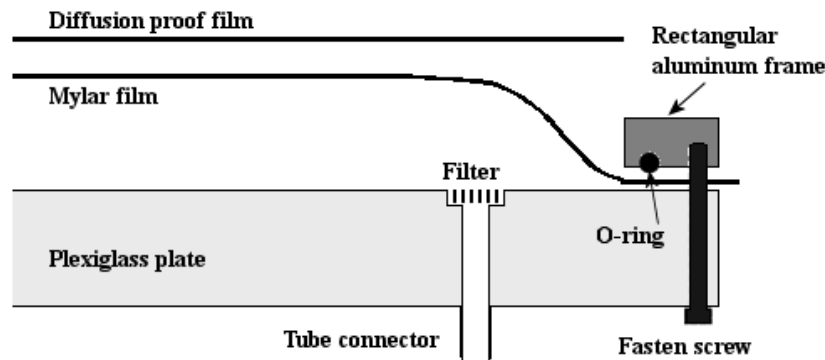
Figure 3.7: *Cross section of the pressure cushion. A mylar film is attached to the plexiglass plate and fastened with a rectangular aluminum frame. Water is then filled between the plate and the mylar film. A diffusion proof film is applied on top of the cushion, to prevent water from diffusing into the porous matrix. Between the tube connector and the cushion there is also a filter ensuring homogenous flow.*
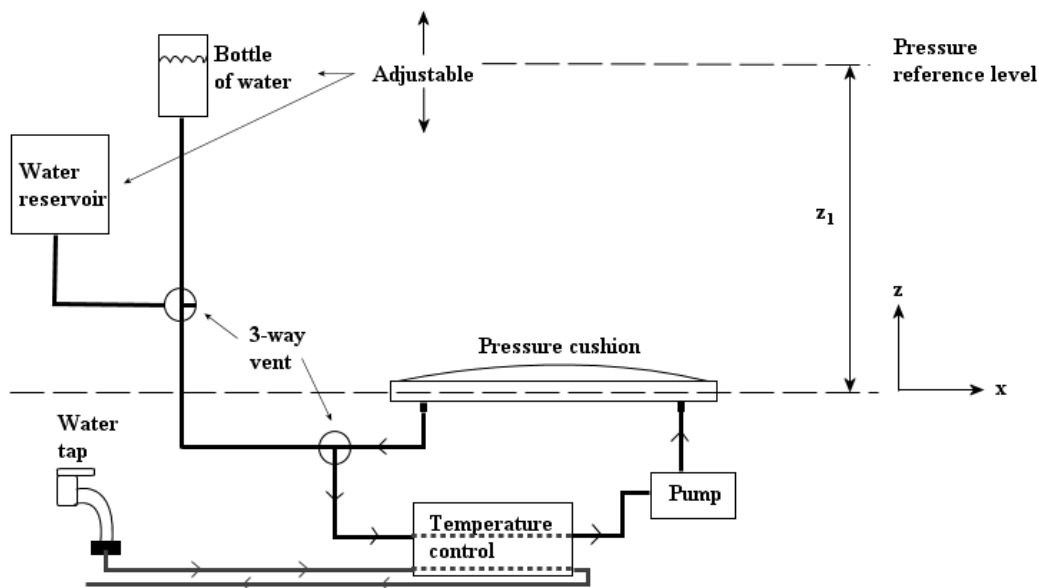
Figure 3.8: *The pressure cushion and the temperature control system. The bottle is kept at a distance $z_1 \approx 2.5$ m above the pressure cushion, to assure overpressure. To fill/empty the system, a water reservoir is connected by a 3-way vent. The water pump circulates the water in the cushion through the temperature control box. The temperature control box is water cooled by a connection to the water tap, which has no connection to the pressure cushion.*

porous matrix exceeded that in the cushion. This caused the problem of a non-constant pore-space volume between the different experiments. We were then forced to apply compressed air pressure to the elevated bottle. It should be noted for later use that a cushion pressure of ~ 7 mH$_2$O (~ 0.7 bar), is at the limit of what the model can handle.

The pressure cushion is a result of previous problems encountered during experiments. In the cand. scient thesis of O. I. Frette [6], it was discovered when using just a plexiglass plate as the resting surface, the displacement structure tended to move in specific parts of the porous matrix. This was due to bending of the model. Bending implies that there are height differences and

thereby a varying hydrostatic pressure between different parts of the porous matrix. This means buoyancy effects when there are density differences between the two fluids. If the gravitational forces causing buoyancy, are comparable with the viscous and capillary forces, the former can no longer be ignored. It is equally important in this respect, to mention that the model itself must be leveled. For our experiments in particular, the viscous forces will dominate. If the model gets slightly out of level, we would not expect the flow to be affected. Another advantage of using a water filled pressure cushion, is that by circulating the water through a temperature controller, one can gain some control over the viscosity of the fluids in the porous matrix.

At the boundary of the cushion there will of course be curvature effects. These are avoided by making the porous matrix (420×850 mm) smaller than the cushion (560×980 mm), and thereby ensuring that the porous matrix is homogenously pushed to the plexiglass plate.

A heavy glass plate completes the main part of the model. The glass plate is of the same dimension as the the pressure cushion, and is placed on top of the plexiglass plate. The plate is 20 mm thick and has a mass at about 28 kg, ensuring that the model is not bent. To completely seal off the model, a number of clamps is used around the rim as shown in figure 3.5.

When the fluid leaves the porous matrix through the four outlet tubes, it continues into a reservoir placed on a digital balance. The balance is relevant because it enables us to measure extracted volume and flow-rates.

3.1.3 Temperature control of the porous matrix

A main point in the experiments performed by Frette [6] was to match the viscosities of the two phases. A temperature control system was developed, due to the strong temperature dependence of the viscosities involved. We use part of this setup in our experiments. As seen from figure 3.9, the viscosity of the glycerol/water mixture varies from 116 cP to 84 cP in a temperature range of 20°C to 25°C. The room temperature in our lab can easily vary in the same range. It will become apparent at a later time, that temperature control is required.
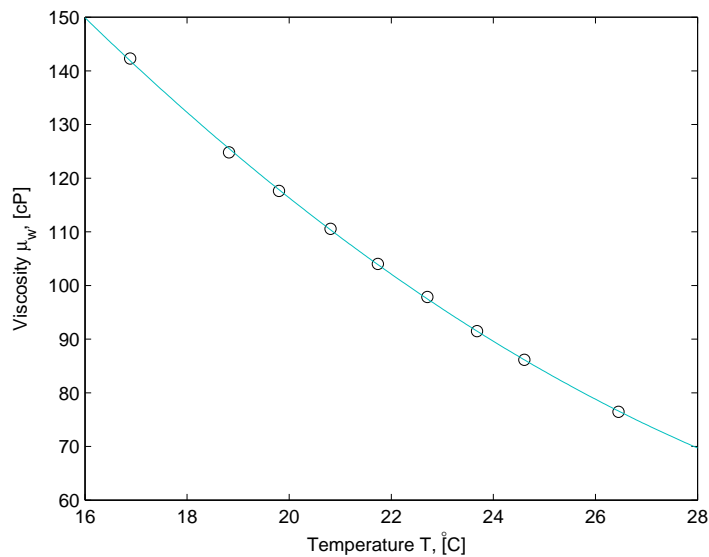

Figure 3.9: *Viscosity measurements of the wetting fluid for nine different temperatures, $\mu_w(T)$. A strong temperature dependence is evident.*

In our experiments we use a *Heto Birkeland* temperature controller. It consists of a box with tube connectors, a heating element and controllers. The box is placed on top of a water bath, and

has a copper spiral for water cooling that extends down into the bath. By a small pump in the box, the water in the bath is continuously circulated through a heat element. The controller can only heat, and therefore water cooling is needed if temperatures below room the temperature are desirable. This is achieved by connecting the copper spiral to the water tap by plastic tubes. To control the temperature of the pressure cushion, we have to circulate its water through the *Heto*-controller by an external pump. Due to the pressure difference between the cushion and the bath, the water in the cushion cannot be circulated directly through the bath. Instead it is looped through a second copper spiral. Figure 3.8 indicates the loop and the water cooling.

To ensure a stable and homogenous heat transfer from the water pillow to the porous matrix precautions have been taken. First of all the water loop is short and also insulated to prevent unnecessary heat loss. Also, two channels have been made at the inlet and outlet of the pressure cushion. A porous filter, i.e a thin plate with lots of small holes, is glued over each channel to get a homogenous flow field in the cushion.
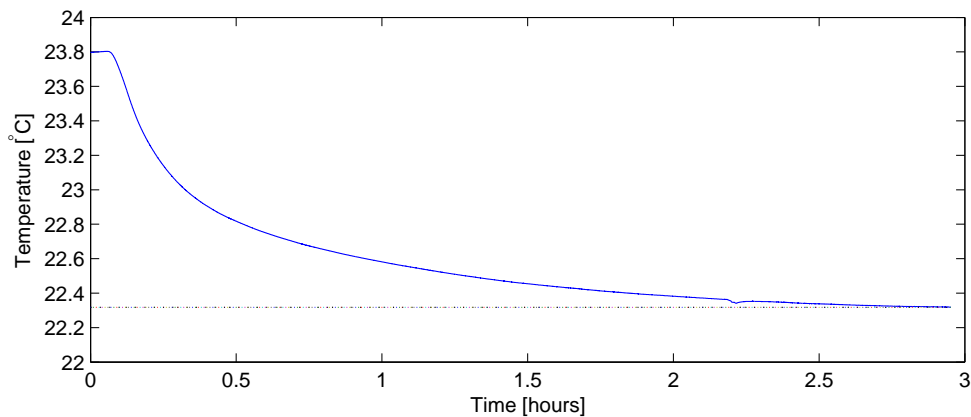

Figure 3.10: *The temperature as a function of time for the thermistor in the porous matrix. The temperature reaches a constant value after* 2.5 *hours.*

When Frette *et al.* developed the heat control system, several thermistors[4] were placed at different positions in the porous matrix, to ensure that every part were at the same temperature. Measurements showed that the setup worked well [6]. In our model we have only one thermistor located at the outlet channel of the porous matrix, see figure 3.6.

When the temperature controller and the pump are started, it usually takes about two or three hours to stabilize the temperature. Figure 3.10 shows the temperature as a function of time from when the controller is turned on, at a temperature of 23.8°C, to the temperature reaches the constant value at about 22.3°C. During our experiments, wetting fluid at room temperature is injected into the temperature controlled porous matrix. It is thus important that the controlling temperature is chosen accordingly. On the other hand we want the wetting fluid to have the same viscosity during all experiments. We find from the thermistor measurements that the temperature at the outlet is stable during steady-state, and fluctuates around a mean value. A point of improvement would be to adapt a thermistor to the inlet side, and also to run the injected fluid through the temperature controller. The largest temperature difference between experiments were about 2°C. This did cause different viscosities, but we have found a way to correct the deviations, as discussed in section 4.3.1.

---

[4]A thermistor is an extremely temperature sensitive resistance. By measuring the resistance, the temperature can be calculated through a proportionality relation.

3.1.4 The pump system

To inject fluid from multiple syringes, a pump system is used. This is shown in figure 3.11. A motor is connected to a speed reducer or gear box, with ten different reduction rates: 1, 2, 5, 10, 20, 50, 100, 200, 500 and 1000. As an example, when the gear box is set to 1000, the gear wheel will have rotated one full turn when the motor has rotated a 1000 turns.

A threaded bar from the gearbox causes the translation bar to rotate. The translation bar is also threaded, hence the "squeeze plate" is moved either up or down, dependent upon whether the motor is in forward or reverse mode. The 15 syringes are mounted in a rack under the "squeeze plate" and are connected by tubes to the flow model. For incompressible fluids, all of the 15 syringes will inject at the same constant flow-rate. To get a feel of the flow-rates involved when

Gear box setting	Flow rate, Q_0 [ml/min]
1	4.59
2	2.51
5	1.02
10	0.55
20	0.27
50	0.10
100	0.055
200	0.027
500	9.4×10^{-3}
1000	6.8×10^{-3}

Table 3.1: *Flow-rate Q_0 from one syringe at different gear box settings.*

using this pump system, measurements have been made. Fluid from one syringe was pumped through the model, saturated with the same fluid, and into a reservoir placed on a balance. By recording the linear mass increase as a function of time, the flow-rate Q_0 was calculated. The values are tabulated in table 3.1.

3.1.5 The lightbox

It is important that the images taken during experiments are of high quality. In practice this means, in addition to use the right lens and camera settings etc, that the lighting of the flow model is favorable. In our experiments we have placed the flow model on top of a lightbox as shown in figure 3.1.a. When experiments are ongoing, the ceiling lights are off and the only light source is the lightbox.

Our objective with the lightbox is to illuminate the flow model as homogenous as possible. This makes the image analysis job much easier, as will be discussed later. The inside of the lightbox is covered with crumpled aluminum foil to ensure that the light is reflected in random directions. Ten light tubes, each at 38 watts, with reflectors are mounted at the bottom of the box. As opposed to most normal light tubes which uses igniters, we use devices that in addition to ignite the tubes also make sure that there is no light flickering. By light flickering we mean the periodic light intensity variations caused by the 50Hz AC voltage supply in the lab. There are of course some heat release from these light tubes, and therefore four fans have been mounted in such a way that air constantly circulates the lightbox. The lid of the lightbox consists of a heavy plexiglas plate to support the weight of the model, and a thin white plexiglass plate to ensure a diffusive white homogenous illumination.

The lightbox as described above, is an upgraded version of the original. The original lightbox consisted of 20 small light tubes similar to those found in desktop lamps, placed at random positions in the box. There were two disadvantages with this setup. A significant light intensity gradient was showing up in every image. The intensity was strongest in the middle and
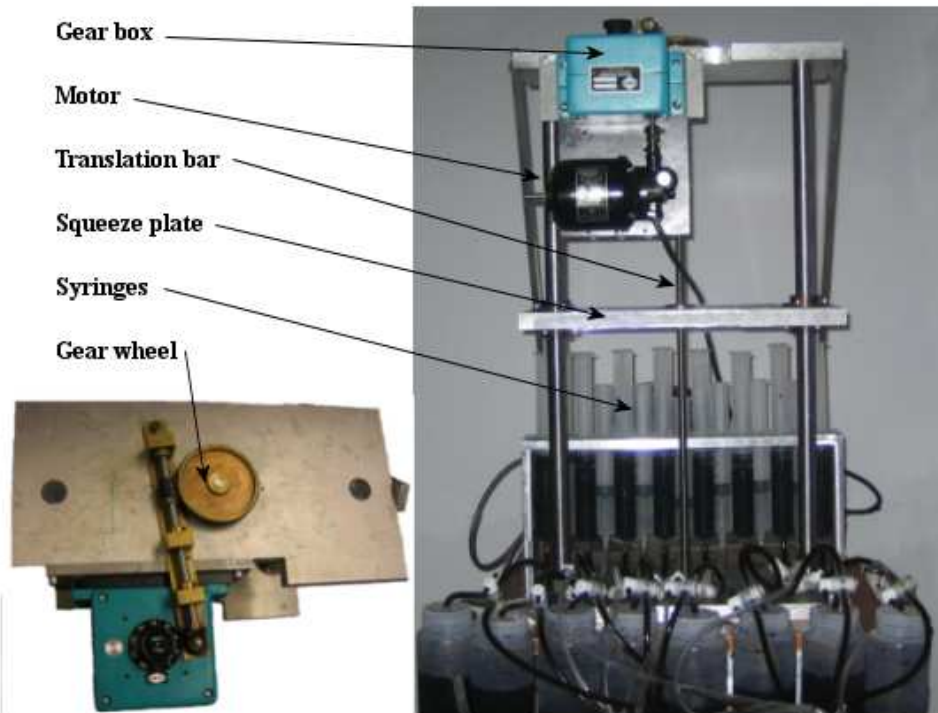
Figure 3.11: *The pump system used in our experiments. A motor is connected to an adjustable gear box. The gear box is connected to a gear wheel that is mounted on top of a threaded translation bar. When the bar rotates it moves the squeeze-plate either up or down, dependent of the motor setting. 15 syringes containing either fluid or gas, are mounted in a rack below the squeeze-plate. There are also mounted two big support bars. In the picture one can also see the fluid reservoirs, used to refill the syringes.*

decreased towards the sides. We also observed intensity shifts when studying several pictures taken with the same background at different times. This was due to the AC voltage supply in the lab.

To test the improvements of the new lightbox, we compared several gray scale images from the old and the new box. In a grayscale image each pixel has an intensity value in the range $[0, 255]$, where 0 corresponds to black and 255 to white. In figure 3.12 we have compared two images of the porous matrix saturated with the black water/glycerol fluid. As can be seen by comparison, there is a significant intensity gradient in the old image, while in the new image the intensity distribution is more homogenous. This is also supported[5] by figure 3.13. As can be seen from the figure, the old lightbox has a parabolic like intensity distribution. In our case the lighted area of our box is 860×1000 mm whereas the area of the porous matrix is 420×850 mm. Since the inlet and outlet of the porous matrix are at the borders of the lightbox, we will experience lower intensity here. This is difficult to improve without using a lightbox much bigger than the flow model.

We also studied intensity distributions of images taken with the same background but at different times, from both the new and old lightbox. This is shown in figure 3.14. Clearly the intensity is a function of time in the old lightbox. In the new lightbox however, the intensity curves from all images fall onto one single curve, indicating little intensity shift.

---

[5]In figures 3.13-3.14 one can not compare intensities directly. This is due to the fact that images from the old and new box is taken with two different cameras with different settings.
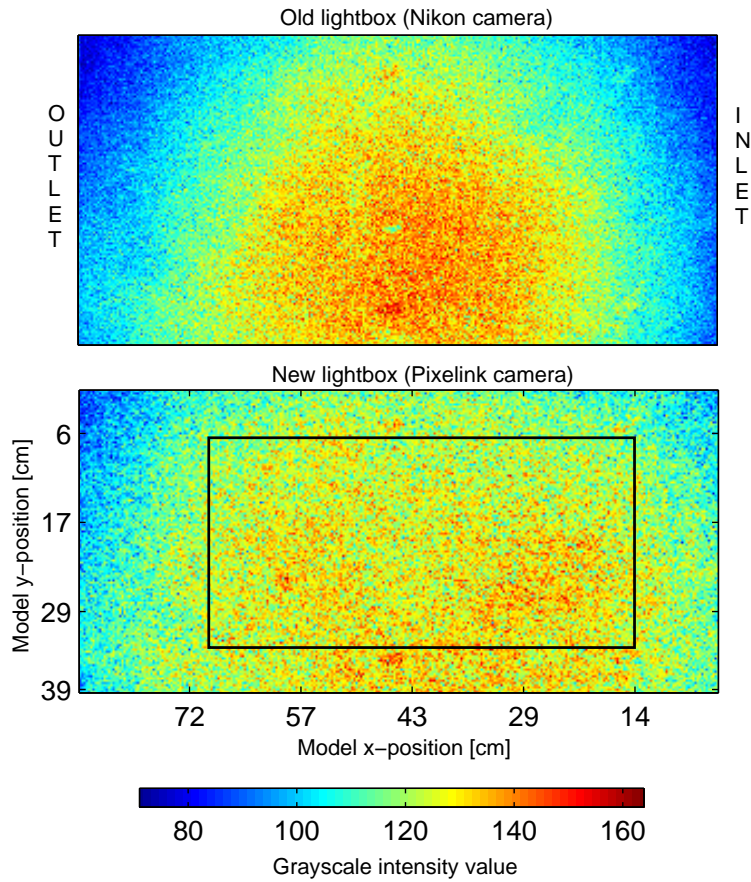
Figure 3.12: *Two images of the porous matrix saturated with the glycerol/water fluid. The images are taken with two different cameras. Each pixel value can be found by the bottom colorbar. These images have been course grained from an original resolution of 1460×2970 pixels to 146×297 pixels. Each element in the course grained matrix is the mean pixel value of the corresponding 10×10 submatrix from the original image. The course graining reveals a strong gradient in the upper image, whereas the situation is more homogenous in the bottom image. The black rectangle indicates the cropped region of our experimental images that is used for analysis.*
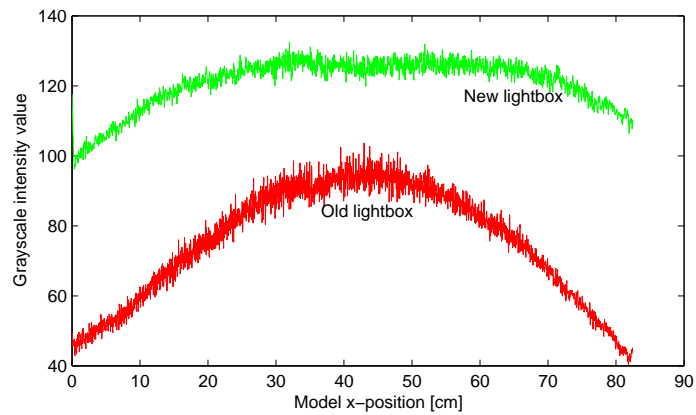
Figure 3.13: *Mean intensity value of each pixel column vs. the model x-position ($x = 0$ cm at the inlet, $x = 83$ cm at the inlet). 1 cm corresponds to ~ 36 pixels. The intensity distribution obtained with the new lightbox is much more flat that the old one.*
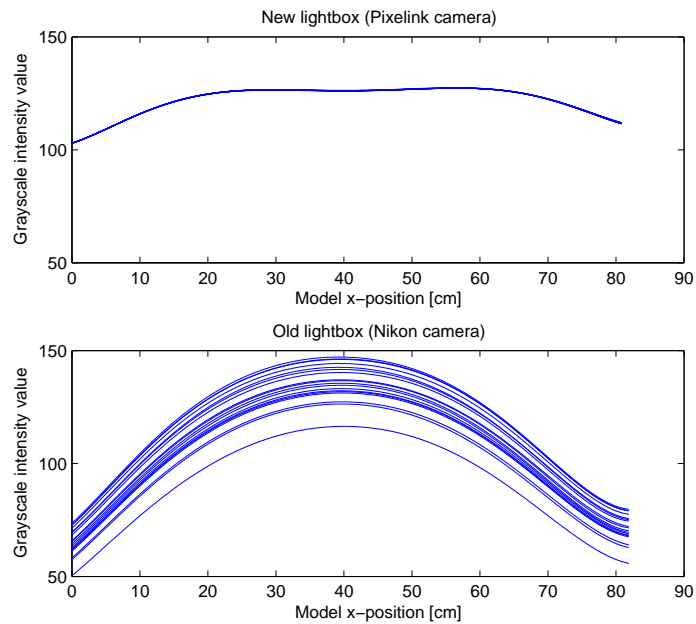
Figure 3.14: *18 images from each lightbox have been used to study any intensity shifts. In both plots the first image is taken at $t_{start} = 0$ min, and the last at $t_{end} \approx 3$ min. The curves were found in the same manner as in figure 3.13, but a polynomial fit was made to avoid the noise and better emphasize the shifts. As we can see intensity is independent of time for the new lightbox.*

3.2 Instrumentation

A considerable amount of time has been put into the instrumentation part of the experiments: Calibration of pressure sensors, getting familiar with the camera, synchronization of all the components, writing the instrumentation program and so on. In our experiments we have four pressure sensors and a thermistor connected to respective channels on a digital multimeter. The multimeter, a camera and a balance are connected to the same computer and controlled by a software package called *LabView*. In this section the various parts of the instrumentation are described.

3.2.1 The Pixelink camera

The imaging device used in all experiments was the *Pixelink Industrial Vision PL-A781* digital camera, shown in figure 3.15.


Figure 3.15: *The* Pixelink PL-A781 *camera. In addition to a lens mount, the camera has two identical FireWire outputs and a Hirose connector for external triggering.*

This is an industrial camera, meaning that it is completely software-controlled by the host computer. The camera uses a 6.6 megapixel monochrome CMOS[6]-sensor, which is a cell consisting of 2208 horizontal- and 3000 vertical pixels. The output from each pixel is a grayscale value. The pixel pitch is 3.5 microns, giving a cell size of 7.7×10.5 mm^2. Table 3.2 lists the manufacturer specifications [11] of maximum frames pr. second at a given resolution. We see that the max-

Resolution, [*pixels*]	Max frame rate, [*fps*]
2208×3000	5
1584×1200	16
1272×1008	25
648×480	88

Table 3.2: *Manufacturer specifications of maximum fps at a given resolution.*

imum frame rate at full resolution is 5 fps. In the lab however, we only managed 3 fps using optimized camera settings without triggering. The reason for this deviation is still unclear to us, but since the time intervals between images in experiments are much larger than the maximum fps interval, we have not put too much emphasis on this point.

Two shutter types are available, namely the *rolling shutter* and the *fast reset shutter*, [11]. The rolling shutter is used when the trigger feature is turned off. This shutter reads out the frame continuously and should be used when the object is static, or only moving slowly. Max fps is obtained with the rolling shutter, due to the continuous readout. The fast reset shutter is somewhat slower because the frame is not read out until the whole frame has finished integration. As the name indicates the whole frame is reset after readout.

The camera has two identical FireWire outputs and a Hirose connector for external triggering. One of the FireWire ports is connected to the host computer and provides power, data and control

---

[6]Complementary metal oxide semiconductor.

communication. The second FireWire port can be used to link multiple cameras etc. Controlling the camera by a laptop may require additional power support to the FireWire bus.

A great advantage of this camera compared to standard digital cameras, is the possibility to program it. In addition to the supplied GUI software, the Pixelink camera can be controlled by custom-made scripts (LabView, Matlab, C++, Basic etc.). In our experiments we control the camera from LabView by the use of *NI Vision Acquisition software*.

The Pixelink camera is flat-field correction enabled or FFC-enabled, which means that the camera can be calibrated to help account for uneven illumination of the object being imaged. As figure 3.12 shows it is very difficult to get a perfectly homogenous lighting of the object. The basic steps of the FFC algorithm are fairly simple. First the background is imaged, in our case the thin white plexiglass plate used to cover the lightbox. From this image, the mean intensity value is calculated and used to normalize every pixel. Then each pixel of the CMOS sensor is offset by division of its respective normalized pixel value from the background image. The FFC-algorithm can also be applied during image analysis, if the camera at hand is not FFC-enabled. Figure 3.16 shows mean intensity values across the lightbox and model. Before the FFC calibration of the camera we can se from the upper blue graph that our lightbox is not completely homogenous. Especially we see the signature of the light tubes by the many "humps" in the graph. After the
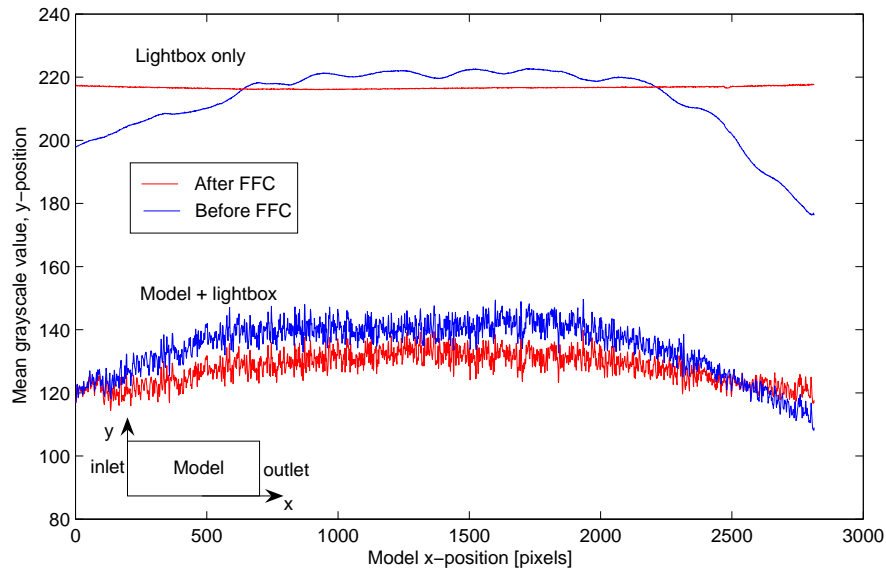
Figure 3.16: *The upper two graphs of the figure show the light intensity variations across the lightbox (background), before and after the FFC calibration of the camera. The lower two graphs show the light intensity variations across the model, before and after the FFC.*

FFC calibration it is clear from the upper red graph that our background is now more or less homogenous. The lower before- and after-FFC graphs of figure 3.16 show the difference in light intensity when the model, saturated with the black glycerol fluid, is placed on top of the lightbox. Part of the reason for the slight curvature of the lower red graph is due to the trapping of small "white" air bubbles when the model was filled with "black" glycerol fluid. However there still seems to be a weak intensity gradient across the porous matrix, but this can be handled in the image analysis process as described in section 3.3. All the work put into optimizing images, is motivated by the fact that the accuracy of results obtained from image analysis are highly dependent upon raw image quality.

3.2.2   Photron fast camera

To specifically study burst behavior of air and also general dynamics during experiments, we used the *Photron Fastcam-Ultima APX*. This is a high speed camera with a maximum frame rate of 2000 fps at maximum resolution, 1024×1024 pixels. The camera can be controlled by a host computer through a FireWire connection. A nice feature of the Photron camera is the possibility to trigger it manually *after* an interesting event has occurred. This means that the camera records continuously, and when triggered it reads out all previous recorded images stored in the camera memory. In this way we were able to capture fast events even when we did not know when they would occur.

3.2.3   Pressure sensors

To control the global pressure development in our experiments, four flow-through *SensorTechnics 26PC0100G6G* pressure sensors were used. Three of them were connected alongside of the porous matrix, and the last one was connected to the air face in one of the syringes as shown in figure 3.6. The sensors measure gage or relative pressure, meaning that a sensor output pressure is always relative to some reference pressure. Each sensor has four pins, two of which are connected to a constant 10 V power supply for excitation, and the remaining two gives the measured pressure output in terms of [V].
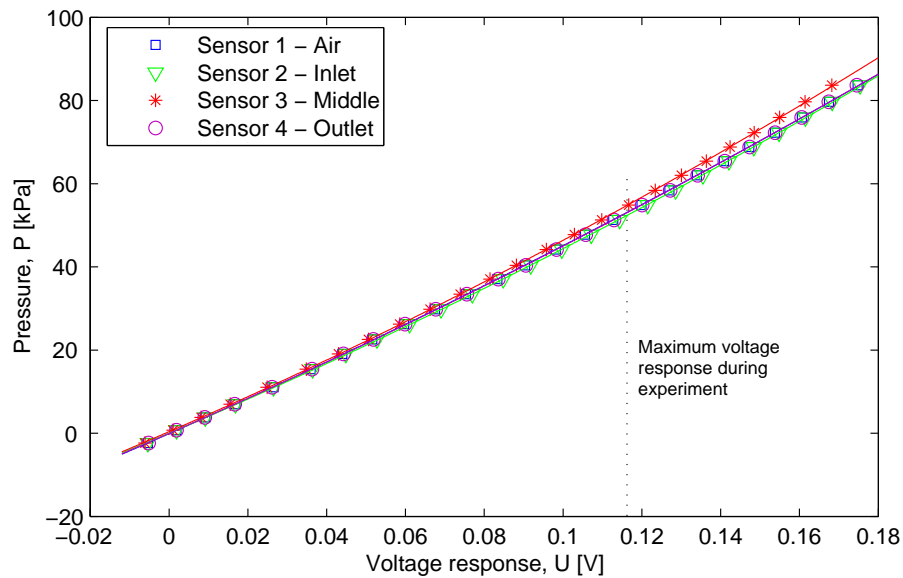
Figure 3.17: *Hydrostatic pressure P as a function of voltage response U from our pressure sensors. The upper limit of the voltage range during an experiment is also indicated by the dotted line.*

The sensors were manufacturer pre-calibrated in the range [0,100] mbar, meaning that they should have the same linear pressure vs. voltage dependency in this range. The highest measured pressures in our experiments exceeded the upper limit of this range by a factor of almost five, hence a calibration in a much wider range was required. During calibration the sensors were connected to a long tube, filled with the water/glycerol fluid. The tube was hoisted vertically in steps of 30 cm. Due to some elasticity in the tube, the fluid level decreased slightly as the pressure increased for each height increment. To account for this, the fluid level was always adjusted to the zero level of the measuring tape. During each step, the sensor output and the distance to some reference level were recorded. Since the vertical distance is proportional to the hydrostatic pressure,

pressure vs. voltage curves were obtained for all sensors, as shown in figure 3.17. These points should be fitted by a quadratic function rater than a linear one.

The calibration function is found from the hydrostatic pressure equation and the fitted quadratic function for each sensor,

$$P(x) = \rho_w g x \tag{3.2}$$

$$P(U) = aU^2 + bU + c \pm 140 \text{ Pa}, \tag{3.3}$$

where P is the pressure, $\rho_w = 1.217$ g/ml is the density of our water/glycerol fluid, $g = 9.81$ m/s^2 the acceleration of gravity, x the height above reference level, U the sensor response and a, b, c fitted constants. The uncertainty given in eq. 3.3 stems from random read-off error during the calibration. Table 3.3 gives the fitted constants for each sensor.

#	a [10^5 Pa/V^2]	b [10^5 Pa/V]	c [10^2 Pa]
Sensor 1	3.505	4.169	-0.929
Sensor 2	4.198	4.017	0.117
Sensor 3	4.922	4.108	3.797
Sensor 4	3.676	4.137	-0.355

Table 3.3: *Fitted calibration constants for our pressure sensors.*
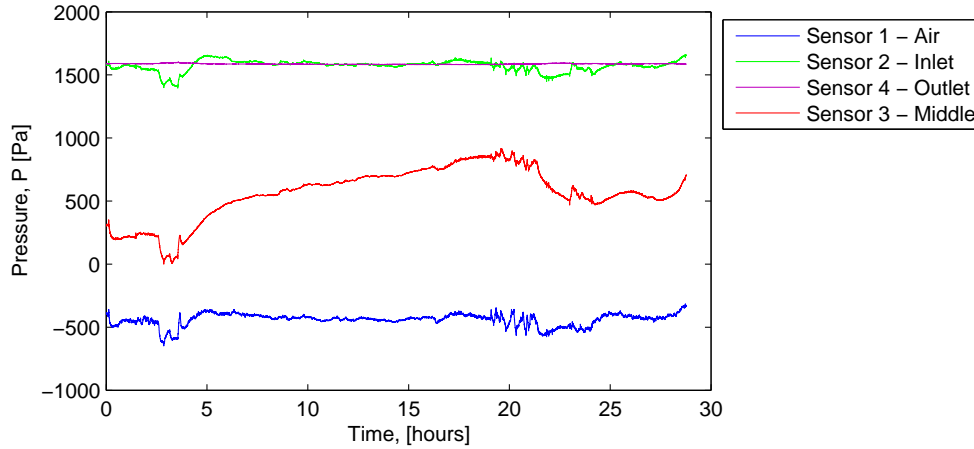
Figure 3.18: *Pressure drift in all four sensors as function of time. The sensors measure constant hydrostatic pressure in this case.*

From the different values of the constant c in table 3.3 we can se that the sensors are offset from each other. To account for this offset, we always start the recording of pressure data before injecting the two phases into the porous matrix. During this time, the sensors are under constant hydrostatic pressure from the outlet reservoir, and hence a plateau $P_{0,i}$ in the pressure recording for each sensor is obtained. The plateaus are then used as new reference pressures for each sensor respectively, so that both the offset and sensor placing relative to the outlet reservoir can be accounted for in later analysis. The measured pressures in our experiments $P_{\text{exp},i}$ are then given as:

$$P_{\text{exp},i}(U) = P_i(U) - P_{0,i}(U_0) \tag{3.4}$$

$$= aU_i^2(t) + bU_i(t) + c - \left(aU_{0,i}^2 + bU_{0,i} + c \right) \tag{3.5}$$

$$= aU_i^2(t) + bU_i(t) + d, \tag{3.6}$$

where the subscript $i = 1, 2, 3, 4$ denotes the different sensors. The coefficient $d = -aU_{0,i}^2 - bU_{0,i}$ is constant and independent of the offset c, provided that sensor drift can be neglected.

To check any sensor drift, $P_{0,i}$ was recorded for a time period of ~ 28 hours. Figure 3.18 shows the large-scale pressure development for all sensors, and the corresponding means and standard deviations are given in table 3.4. From figure 3.18 we see that sensor 1,2 and 4 has little or no

	Sensor 1	Sensor 2	Sensor 3	Sensor 4
$P_{0,i}$ mean [Pa]	-440	1572	565	1587
$P_{0,i}$ std. deviation [Pa]	48	43	203	4

Table 3.4: *Mean values and standard deviations for all four pressure sensors when measuring a constant pressure (figure 3.18). The measurement time was ~ 28 hours.*

drift and fluctuates around the mean value. This is also reflected by the standard deviations i table 3.4. Sensor 4 is very close to measuring the same constant pressure at all times, with a standard deviation of only 4 Pa. Sensor 3 has larger fluctuations and the standard deviation is also considerably larger than for sensor 1,2 and 4. There seems to be some drift over the measured time interval. However, the drift should not be of crucial importance in the experiments, due to the much larger pressures. The pressure range in our slowest experiments is approximately $[9500, 18450]$ Pa relative to atmospheric pressure, whereas the measured drifting range is in the interval $[0, 700]$ Pa relative to atmospheric pressure.

The reason for the difference in fluctuations, between identical sensors is still unclear. It does however illustrate the importance of calibration and checking for drift.

3.2.4   Acquiring data with LabVIEW

To collect data from our experiments we use the *National Instruments LabVIEW 8.0* software package. LabVIEW is commonly used for data acquisition, instrument control and other sorts of technical computing. Its programs are called virtual instruments or just VI's. Each VI has two main components, namely the front panel and the block diagram. The programs are made in the latter, and are based on a visual programming language. This programming consists mainly of dragging and dropping pre-written functions, also called sub-VI's, and wiring them together. This is in principle very simple, with some basic programming knowledge. To run the finished program, one simply opens the front panel of the VI, which is the user interface, and executes. Figure 3.19 shows the making of a simple LabVIEW program.

During an experiment we collect different kinds of data. In addition to the images captured we have both pressure sensors and a thermistor whose response values are read by a *Keithley 2701* digital multimeter. The amount of fluid extracted from the model output is measured by a digital balance. Since LabVIEW can handle a variety of hardware, we were able to run the camera, multimeter and balance all within one VI. This gave us the ability to synchronize every component with good accuracy, and to reduce the number of computers needed to perform an experiment. Figure 3.20 shows the front panel of the VI used for all experiments. This VI can be downloaded at the referenced URL, [49].
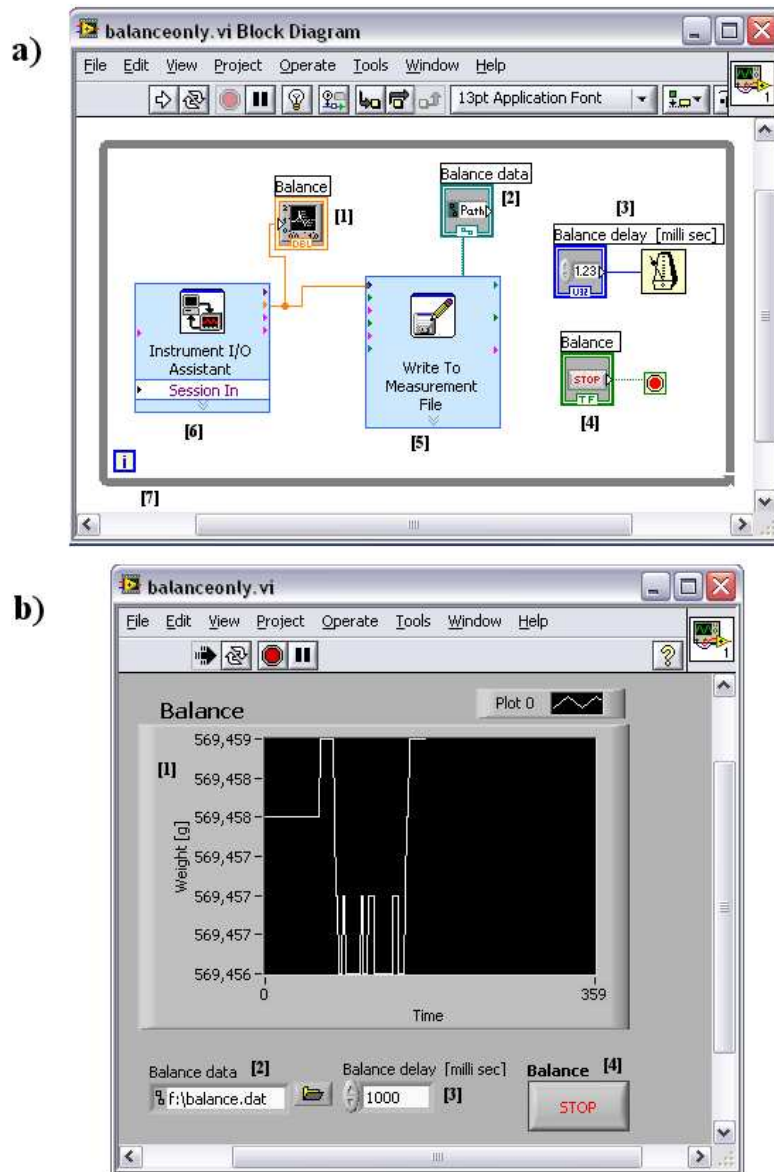
Figure 3.19: *Simple LabVIEW program that reads data from a digital balance connected to the computer via the COM-port.* ***a)*** *shows the block diagram, with the different sub-VI's labeled from [1] to [7]. First the "Instrument I/O Assistant" [6] is placed on the block diagram. This sub-VI communicates with the device connected through the COM-port. The output data of [6] is then wired to a graphical display [1] and the "Write To Measurement File" [5] sub-VI. The latter writes the balance readings as a function of time to file, specified by the file path [2]. Multiple readings are performed by placing the whole structure inside a while loop [7]. The "while-loop delay" [3] is used to set the timestep of the readings and the stop button [4] terminates the loop.* ***b)*** *shows the resultant front panel. In addition to just writing data to file, the user is able to adjust the time step and monitor the measurements through the graphical display.*
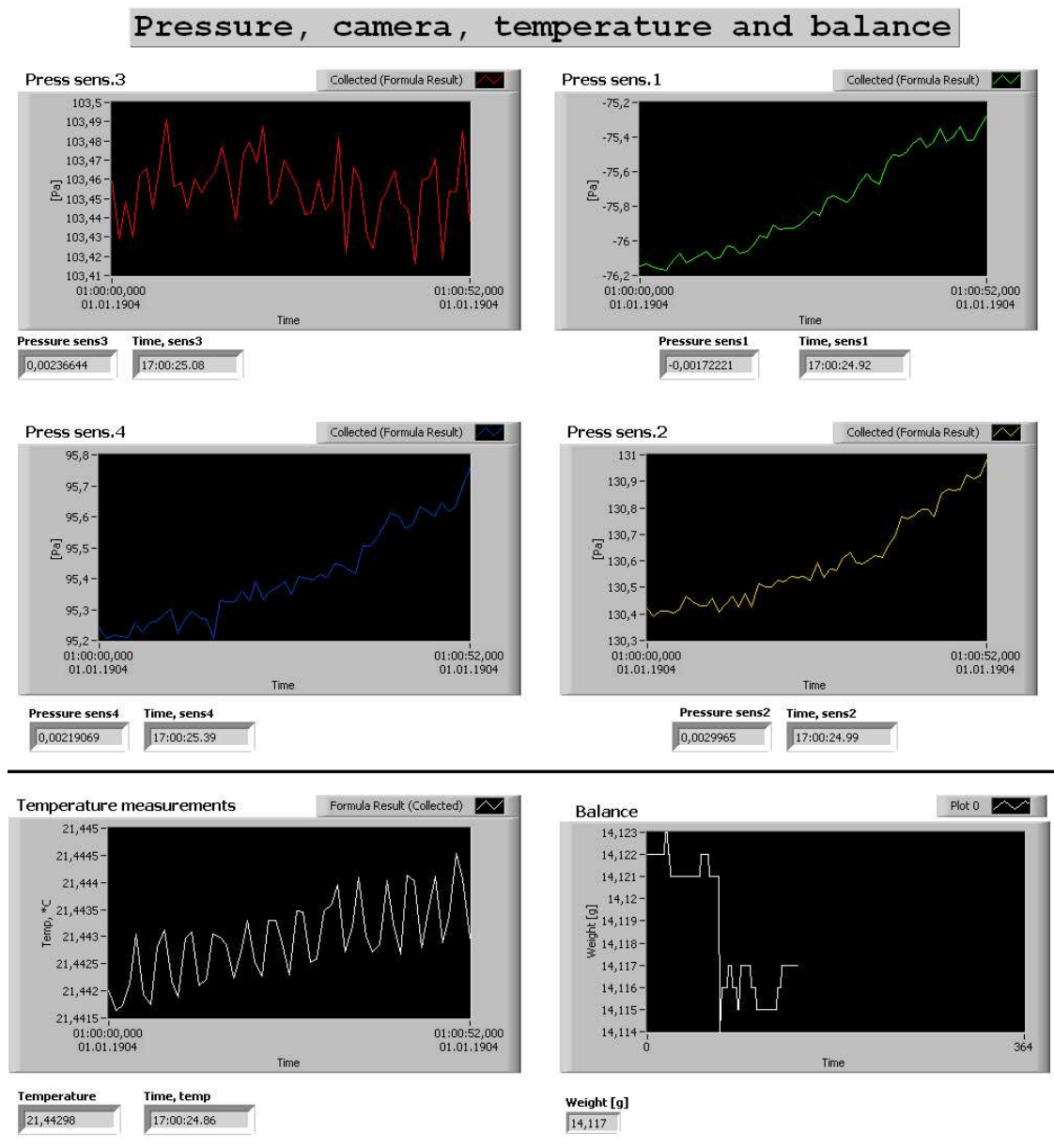
Figure 3.20: *Front panel of the VI that we constructed for our experiments. There are six graphical display windows, one for each of the four pressure sensors, one for the thermistor and one for the balance. In the "write to file" section we can choose the path for the out-data files. We can also set different timesteps for the hardware components. In an experiment we measure the pressure at the fastest rate, keeping "scan delay"= 0 ms. The balance is typically read every second and the time between images depends on the duration of the experiment. Each hardware device can be switched on or off by the indicator buttons placed bottom right in the front panel.*

3.3   Image analysis

Everyone know the expression that "*a picture says more than a thousand words*". Our experimental images contain large amounts of data. A trained eye would, just by looking at an image, be able to give rough estimates of geometrical properties such as clustersizes, clustershapes, orientation of clusters, saturation of fluid and so on. To quantify these and many other properties, the experimental raw image has to be analyzed.

3.3.1   The black and white image

A random pixel from one of our raw images can be part of either the air phase, glycerol phase or a glass bead. The raw images are grayscale and have pixel values/intensities in the range $[0, 255]$, where 0 corresponds to black, and 255 corresponds to white. Glass beads and air typically have a distribution of pixel values near the upper limit of this interval, whereas the distribution of glycerol fluid pixels is centered much lower. The first part of the image analysis is always to reduce the raw image to a binary or black and white image. We want all pixels representing air and glass beads to have the value 1 (white), and the remaining pixels representing the glycerol fluid 0 (black). This conversion is not solely used for our porous media experiments. A variety of experiments involve geometrical objects that differ in size and shape, but have common properties like the color. If you want to extract the interfaces between objects of different graylevels, this is not easily done with the raw image. There is no pronounced jump in graylevels from one object to the other, so the interface is not clearly defined. This motivates the need for a binary version of the original image, where an interface consists only of neighboring black and white pixels.

   An image is basically just a matrix whose elements represents pixels, and again the pixel values gives the color coding according to some color map. Figure 3.21 illustrates the visualization of a binary 5 by 5 matrix, with the black and white color map.

$$\begin{bmatrix} 0 & 0 & 0 & 0 & 0 \\ 0 & 1 & 0 & 1 & 0 \\ 0 & 1 & 1 & 1 & 0 \\ 0 & 1 & 0 & 1 & 0 \\ 0 & 0 & 0 & 0 & 0 \end{bmatrix} \rightarrow$$
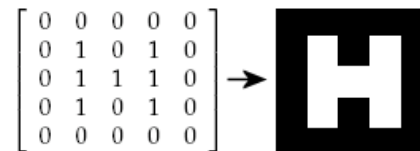
Figure 3.21: *Visualization of a binary 5 by 5 matrix, using the black and white color map. The image size is 5×5 pixels and equals the matrix dimension.*

After converting the raw image, the resultant matrix of the binary image can be used to compute numerous properties of the object imaged. Properties relevant for our experiments will be discussed later in this section, but to pursue the task of extracting the interfaces in a binary image, a simple algorithm can be used:

Loop through the image matrix, and for each element test the following:

1. Find the pixel value?

2. If the pixel value is 0 find the value of all the neighboring elements.

3. If one of the neighbors has the value 1, the element is part of an interface and its coordinates (matrix indices) must be stored.

4. Else, go to the next matrix element.

3.3.2   Finding the threshold

Upon conversion of a grayscale image to a black and white image, one must define a so called *threshold* level, which is an integer value in the grayscale range. Every pixel above this threshold level is counted as white, the rest is counted as black. The accuracy of any results obtained from image analysis is highly dependent upon how well the interfaces of the black and white image trace the actual interfaces of the object imaged. The only tuning parameter here is the threshold value.

To find a good threshold value the raw image itself must be of high quality. This means of course optimal camera settings and satisfactory resolution, but the most important thing is perhaps the illumination of the object. Uneven illumination causes intensity gradients in the image, which is unfavorable. Imagine an object whose illumination is strongest at the center and decaying fast towards the sides, like our old lightbox seen in figure 3.12. If we take the object imaged to be our porous matrix, air and fluid clusters at the middle would have a higher intensity (grayscale value) than clusters far away from the center. Conversion of this image into a binary image, using a threshold value suited for the center of the porous matrix, would cause the extracted interfaces between air and fluid at the sides to correspond badly with the actual interfaces. "Air" pixels at the actual interface would be below the threshold value and therefore counted as black. The effect is a size increase/merging of black clusters and size decrease/separation of white clusters towards the sides of the resulting black and white image. Figure 3.22 shows this distortion effect. An apparent solution to this problem is to reduce the gradient as much as possible, so that the chosen threshold works for the whole image. This can be a tedious process, as was experienced in our case by having to rebuild the lightbox, but the advantage is images easier to threshold. Another approach is to split your image into smaller regions and threshold them differently. The threshold would then be high for the darker regions and decreasing towards brighter regions of the image. Using multiple thresholds for a single image is very time consuming when analyzing multiple images.
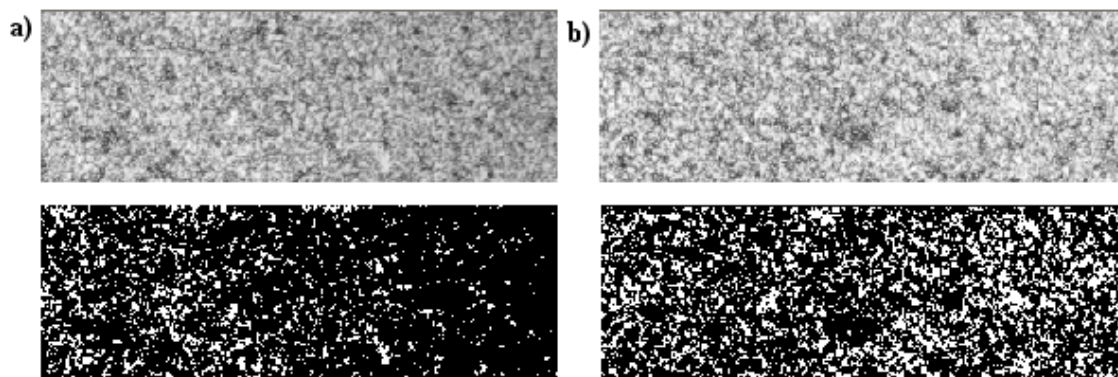

Figure 3.22: *a) The upper image is a segment from a larger grayscale image, showing small air and fluid clusters. Illumination intensity decreases from left to right. The corresponding black and white image does not represent the distribution of air and fluid in the segment imaged very well. b) Segment from the center of the same image as in a). There is no intensity gradient present and the black and white image gives a good representation of the air and fluid distribution in the segment imaged. The threshold value in both a) and b) is* 203.

The influence of gradients upon image thresholding depends on several factors, but mainly the gradient strength over the region imaged. In addition small clusters are more sensitive to gradients than large ones. In our experiments clusters of the air phase is much smaller compared to the size of the model, so the gradient effect can be severe if not dealt with. The lower image of figure 3.12, shows the gradient in our experiments. We mostly study the region indicated by the black rectangle in the lower image, which is fairly homogenous. In addition to limiting the region

of interest, we also apply the FFC algorithm described in subsection 3.2.1. In every respect, we
have tried to minimize the gradient effect, to be able to use one threshold value equally good for
all parts of the image.

When gradients are minimized, the next task is to choose a good threshold value. For two phase
flow experiments it depends on the experiment at hand. The image histogram should always
be studied. If one is able to identify separated distributions for both phases, the best threshold
is found by locating the minimum between the two. Figure 3.23 shows the histogram from a
capillary fingering image. The mean of the black glycerol/water- and white air-distribution is
located around 125 and 255 respectively. Based upon the histogram the best threshold value is
around 200. Figure 3.24 illustrates the effect a bad threshold value can have upon extraction of
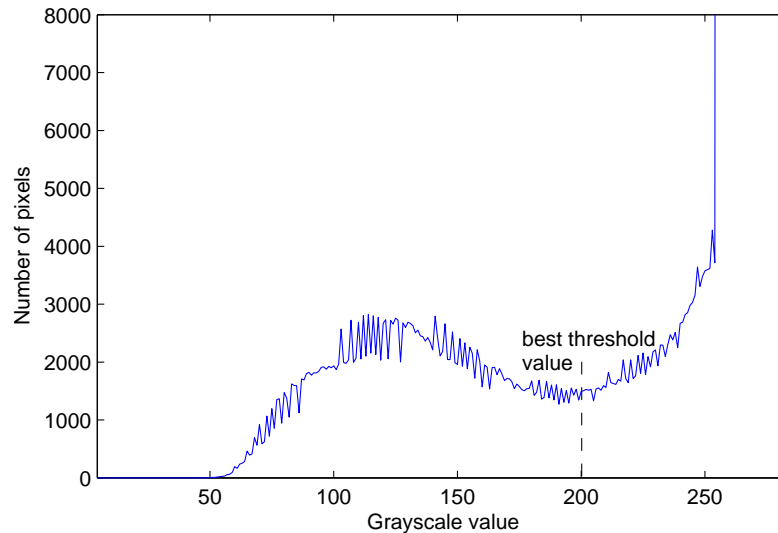

Figure 3.23: *Pixel histogram of the grayscale image shown in figure 3.24 a) and b). The best threshold value is found from the local minimum as indicated.*

image properties. Each of the images c), d) and e) is a zoom in of the original image shown in a)
and b). In a) and d), we have used the threshold value of 200 to convert the raw image into black
and white. From the binary image the largest interface, i.e. the front of the capillary fingering
experiment, is found and superimposed on the original image. In b) and e) we follow the same
procedure but with a threshold value of 156, giving a different front than in a). The image in c)
shows the region where the two fronts from a) and b) differ the most. After comparing the two
fronts, it is evident that the red front follows the interface of the original image the best. Though
the histogram method of determining the threshold level works for some experiments, it should
always be verified by visual inspection. By visual inspection we mean comparing by the naked
eye, extracted interfaces from the binary image with the original image for a given threshold. In
fact, if the histogram resulting from the experimental image does not give a clear indication as to
where the threshold should be set, visual inspection may be the only way.

In our steady state experiments, it is hard to use the histogram in determining the threshold,
due to the wide and mixed distributions of fluid and air clusters. The reason for this mixing lies
in the nature of our experiments. In the steady state phase, thousands of small fragmented air
clusters are embedded in a background flow field of fluid. A large number of clusters means
many interfaces between air and fluid, which again implies local graylevel gradients in the im-
ages. The fluid also wets the porous media well, and give rise to film flow. Films of the black
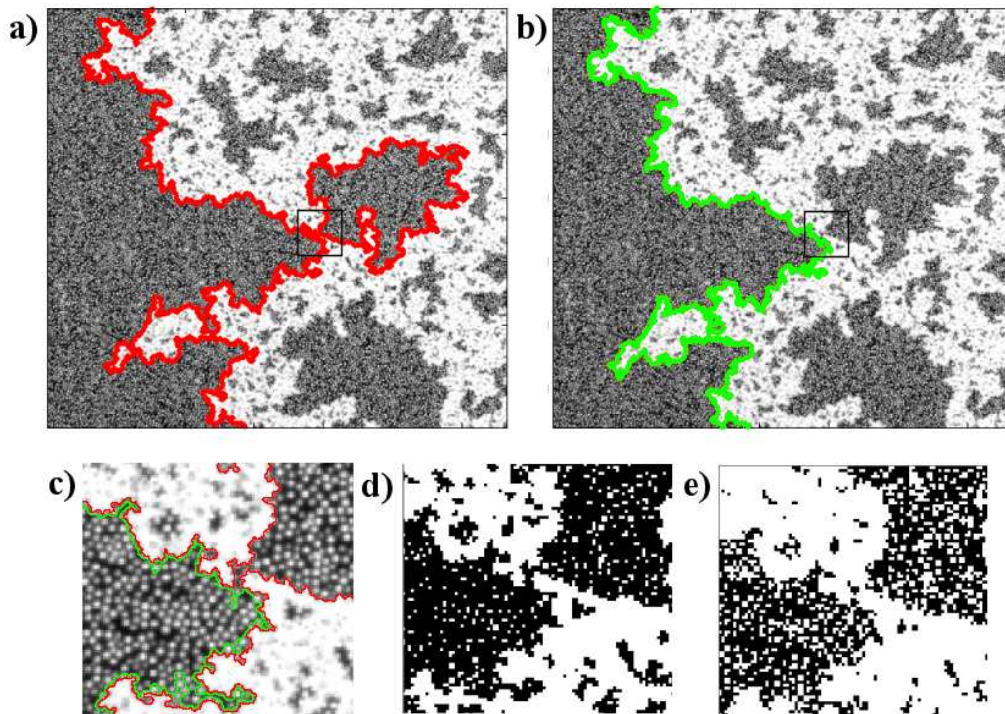
Figure 3.24: *a) Front (red) of the defending cluster in a capillary fingering experiment superimposed on the original image. The front was extracted from the black and white image using a threshold value of 200. b) Similar to a) but the front (green) was now found using the threshold level 156. c) Segment containing the black square of the original image used in a) and b). As can be seen, the biggest black cluster consists of two larger "blobs" connected by some "single" bonds. d) Black and white version of the same segment as in c), using a threshold of 200. The "singly connected" bonds are still intact. e) Similar to d) but with the threshold value 156. This is a case of bad thresholding since the "singly connected" bonds have vanished, resulting in two big separate black clusters.*

fluid obviously transmits more light than e.g a fluid filled pore, thus contributing to a wider pixel distribution for the fluid. Some air clusters also appear darker than others. This is due to a fluid film surrounding the air cluster. The result is a mixing of the two distributions, making the threshold hard to find.

To further improve the quality of our raw images, a sharpening algorithm is applied. We will not go into any details of this algorithm, but it is a common tool in most image treatment software. Sharpening enhances the contrast and shifts "dark" areas to the left and "brighter" areas to the right in the grayscale range, thus reducing the problem with dark air clusters. Figure 3.25 shows before and after images using the sharpening tool, together with the resulting histograms.
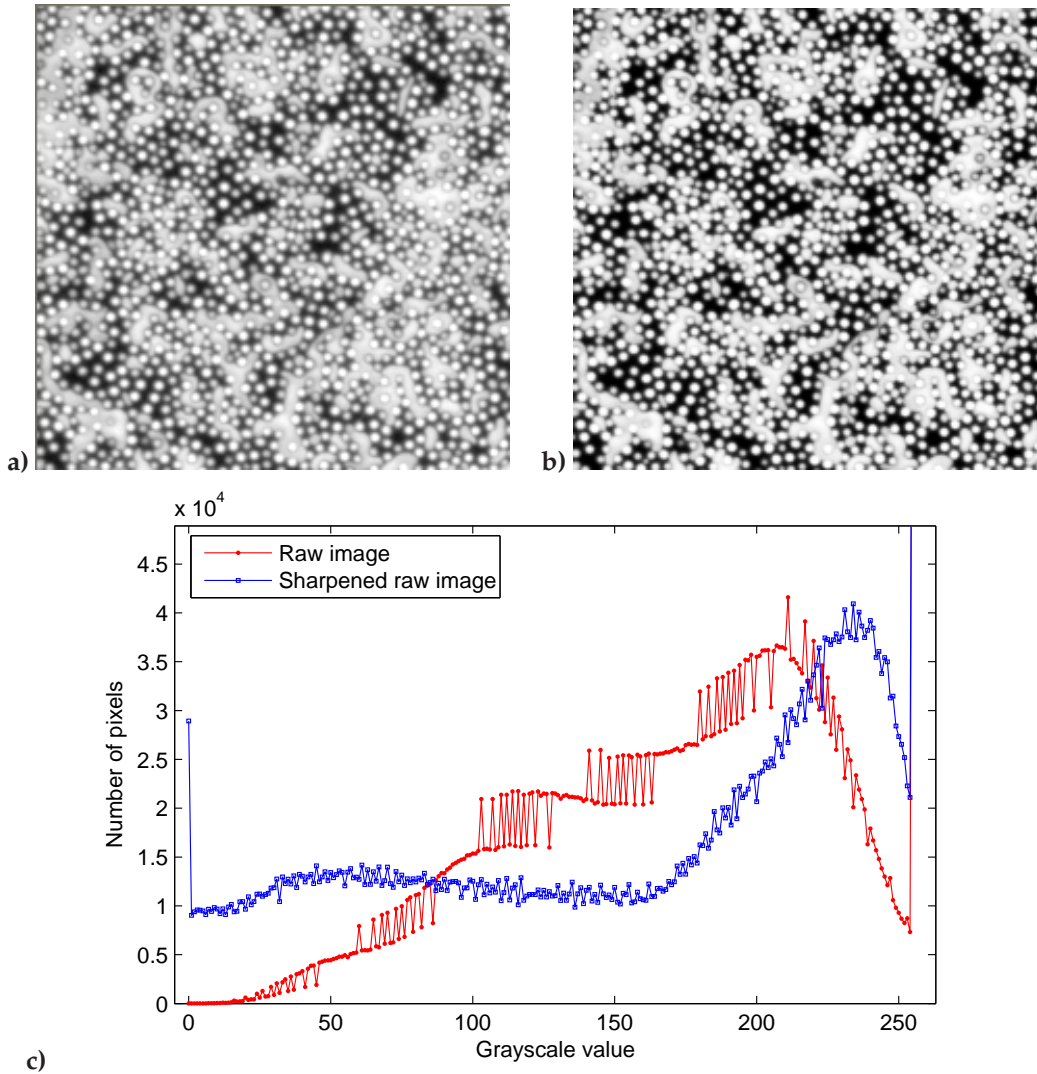
Figure 3.25: *a) Cropped section of a larger raw image from our experiments. b) Sharpened version of the image in a). By comparison of the two images, is clear that sharpening does not affect any of the interfaces. c) Histograms of the full image used to obtain the sections in a) and b). The sharpening separates the fluid and air distributions to some extent.*

When the raw image is sharpened, the threshold is found by visual inspection. It is hard to identify one unique value, so we always narrow the search for the threshold down to an interval in which we believe the value must be set. The upper and lower limit of this interval can then be used to estimate the uncertainty in the extracted properties. This will be discussed in more

detail in Chapter 4. Visual inspection is time consuming, and in an experiment 500-1400 images are captured. A just question is whether all images from the same experiment can be thresholded with the same value, found from a couple of images. If the lighting conditions cause an intensity offset varying in time, the threshold must be changed accordingly. On short time scales we have seen that intensity does not vary with time. On large timescales, the intensity of daylight changes. In our image analysis, we have mainly focused on the steady state regime of the experiments. The duration of this regime varies in the interval $[0.5, 9]$ hours, dependent upon the flow rate of the experiment. To see if the changing of daylight had a significant effect, the porous matrix was imaged for $\sim$ 24 hours without injection of any phases. For all images the mean value of each pixelcolumn was found and plotted against the model x-position, similar to what is done in figure 3.16. A polynomial fit was then made to the resulting experimental data. Using these fits, the mean grayscale value at three positions where found for all images, and plotted as a function of time, see figure 3.26.
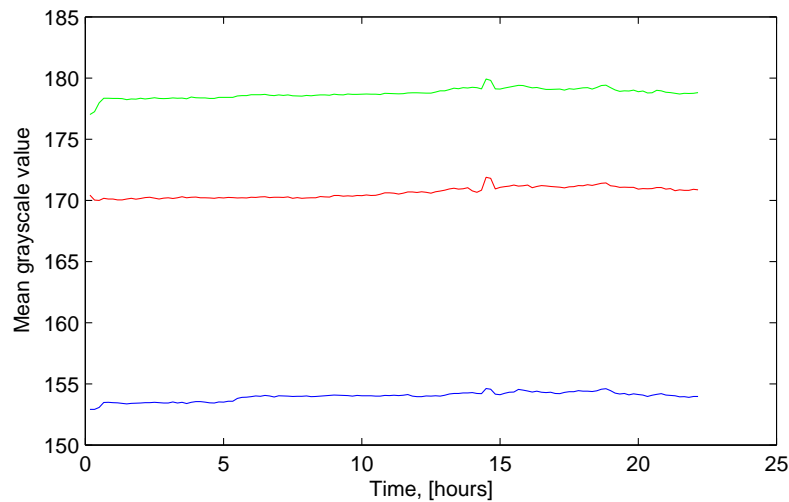

Figure 3.26: *Mean pixelvalues for three positions (inlet, middle and outlet) in the model x-direction as a function of time. The time average for the upper, middle and lower graph is* 179, 171 *and* 154 *respectively. The standard deviation is* 0.4 *for all graphs, indicating little large-scale influence of the images.*

Since the pixelvalues only have small deviations of both large and small timescales, we use the same threshold for all images. Spot tests were nevertheless performed to visually verify that the chosen threshold would work for multiple images.

3.3.3   Extraction of properties and Matlab scripts

To analyze the images from our experiments, the *Matlab Image Processing Toolbox* have been used. This toolbox includes two essential functions, named `bwlabel` and `regionprops`.

The bwlabel-function takes a binary image matrix and connectivity type as input. The output is a labeled image matrix where each cluster has a unique integer label. The algorithm used follows the general procedure outlined in reference [12]. Connectivity type defines the way matrix sites are connected. A value of 4 corresponds to *nearest-neighbor* connectivity, and means that a site can have a maximum of four neighbors located directly to the left, right, above and below the site. A value of 8 corresponds to *next nearest-neighbor* connectivity, which also includes diagonal sites and means that a site can have a maximum of eight neighbors. As an example the center site in the binary matrix of figure 3.21 has two neighbors if we use nearest-neighbor connectivity and six neighbors if next nearest-neighbor connectivity is applied. In both cases the number of

connected sites in the cluster is seven. The ability to choose between connectivity types when analyzing images, raises the question whether this affects the results or not. Again this depends on the experiment at hand. For our steady state experiments with lots of small fragmented clusters, we have found that nearest-neighbor connectivity is the best choice. This prevents to some extent merging of originally separated clusters, when thresholding images. However, comparison of extracted properties using both connectivity types has shown only small deviations.

The regionprops-function uses the labeled matrix found by bwlabel to collect statistics of specified properties. In our analysis we use this function to extract the following properties for each cluster in the image:

- **Area**: Number of pixels in the cluster.

- **BoundingBox**: The smallest rectangle containing the cluster.

- **Eccentricity**: The eccentricity of the ellipse that has the same normalized second central moments as the cluster. Basically this means the best ellipse that can be fitted to the cluster.

- **Orientation**: The angle between the major axis of the ellipse and the *x*-axis of the image matrix.

The area property is used to find the cluster size distribution. The remaining properties provide information about the shape and orientation of the clusters in the porous matrix. Eccentricity of an ellipse is the ratio of the distance between the foci and the length of its major axis. A "circle-shaped" cluster would give an eccentricity close to 0, whereas an "elongated" cluster gives a value close to 1 for the fitted ellipse.

The main Matlab script and sub functions written for extraction of the properties mentioned above, is included in Appendix B.1. The main script time averages the properties of multiple images from the same experiment and saves the data to file.

3.4 Measurement of basic flow parameters

This section gives a review of how the basic flow parameters were measured. By basic flow parameters we shall mean: Viscosities, wetting properties, absolute permeability and surface tension.

3.4.1 Viscosity

The wetting fluid used in all our experiments is a $85 - 15\%$ by weight glycerol-water mixture, dyed with 0.1% Negrosine. The mixture is dyed to enhance the contrast between the two phases. The viscosity of the glycerol/water mixture was measured by a temperature controlled *Ubbelohde Viscometer*. Briefly explained, the kinematic viscosity (eq. 2.9) was found by measuring the time it took for a fixed fluid volume to flow trough a capillary tube. From the Viscometer manual, a constant of proportionality was given that related the measured time to the kinematic viscosity. Separately, the fluid density was measured,

$$\rho_w = 1.217 \, \text{g/ml}. \tag{3.7}$$

The dynamical viscosity could then be calculated through eq. 2.9. The temperature was varied in the range $[17, 27]°$C. For each temperature, the viscosity found was an average measure over four runs. The temperature dependence of our glycerol/water batch is shown in figure 3.27. It is evident that the viscosity has a strong temperature dependence. As will become clear in chapter 4, a temperature difference of only 2°C can cause a significant difference in the measured pressure during steady-state.

The wetting fluid is recycled, and one batch of roughly 5 liters has been used. One could imagine that the viscosity of the batch would change when recycled many times, due to mixing
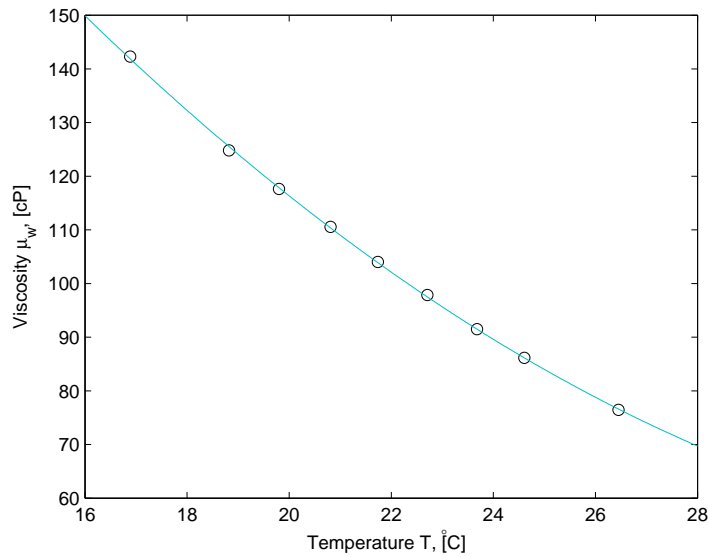
Figure 3.27: *Measured viscosity μ_w of the 85-15% by weight glycerol-water solution as a function of temperature T. The fitted quadratic line is used to find the viscosity in the temperature range $[17, 27]°C$. The density is given as, $\rho_w = 1.217$ g/ml. As a reference, the viscosity of water at $T = 20°C$ is $\approx 1cP$.*

with the glue of the contact paper in the porous matrix. However, measurements performed by Løvoll *et al.* [4] showed that this was not the case.

Air is used as the non-wetting fluid and its viscosity and density are tabulated [46]. At $T = 20°C$ we find the following values,

$$\mu_{nw} = 0.0182 \text{ cP} \tag{3.8}$$

$$\rho_{nw} = 0.0121 \text{ g/ml.} \tag{3.9}$$

Compared to the wetting fluid, the change in non-wetting fluid viscosity are insignificant in the temperature range given in figure 3.27.

3.4.2 Wetting properties

We use air as one of the phases mainly due to its good non-wetting properties. The combination of air, glycerol/water and glass beads gives a very good wetting of the porous matrix. Figure 3.28 shows a droplet of the glycerol/water fluid (surrounded by air) placed on a glass surface. Through a coarse method of image analysis, the static contact angle θ was estimated to be,

$$\theta \approx 33°. \tag{3.10}$$

With this contact angle of the wetting fluid, we are far away from mixed wetting conditions. The fact that air is a very good non-wetting fluid is of great convenience. It is thus possible to recycle the porous matrix, so that it can be used for numerous experiments.

No measurement of the surface tension γ between the wetting and non-wetting fluid, was performed during this work. When needed, we have used the value given in [4]. In this study the surface tension between glycerol-water (mixed $90 - 10\%$ by weight) and air was reported to be,

$$\gamma = 0.064 \text{ N/m.} \tag{3.11}$$

Figure 3.28: *Droplet of the glycerol/water solution (surrounded by air) placed on a glass surface. It is evident that the glycerol/water wets the glass surface. The wetting angle $\theta \approx 33°$ was found through geometrical considerations of the imaged droplet.*
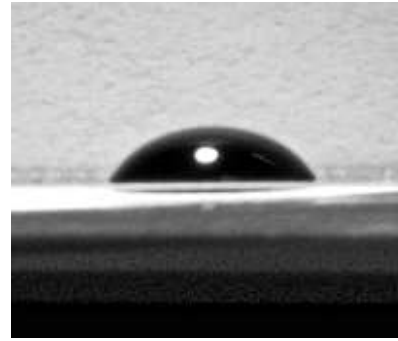
The mixing of glycerol-water in this case is different from ours, but we expect γ to be of the right order of magnitude. In our study, the surface tension is only used to estimate the capillary pressure and so the value in eq. 3.11 is found to suffice.

3.4.3   Absolute permeability

The absolute permeability K has been measured for our porous matrix. A single-phase flow experiment was conducted using eight syringes of wetting fluid. For each selected flow-rate, the pressure difference over the model was measured when it had stabilized. From Darcy's law we would expect these points to fall on a straight line,

$$\Delta P = \frac{\mu_w L}{KA} Q_w. \tag{3.12}$$
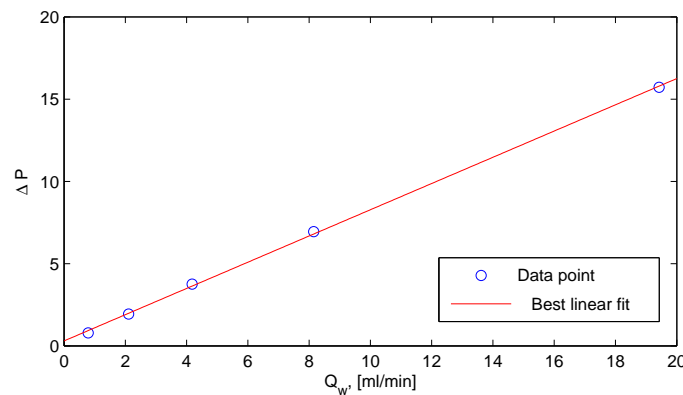
Figure 3.29: *Pressure difference ΔP over the length L of the porous matrix as a function of the imposed wetting fluid flow-rate Q_w. A linear fit is made to the measured data points, and the slope is used to find the absolute permeability K.*

The temperature was controlled to $T = 24.0°C$, giving a viscosity of $\mu_w = 89.6$cP. The system size is,

$$L = 83.1 \text{ cm}, \tag{3.13}$$

with a cross section of,

$$A = lb = 4.08 \text{ cm}^2, \tag{3.14}$$

where $b = 1$ mm is the diameter of a bead. Figure 3.29 shows the pressure difference ΔP over the model as a function of the wetting fluid flow-rate Q_w. From the extracted slope and eq. 3.12, the absolute permeability was found to be,

$$K = 1982 \pm 53 \text{ Darcy} \tag{3.15}$$

This value is consistent with earlier measurements on a similar flow-model, performed by Løvoll et al. [4].

The porosity of the model is found by (see eq. 2.1),

$$\phi = \frac{V_{ps}}{LA} \approx 0.63, \tag{3.16}$$

where V_{ps} is the pore space volume. V_{ps} is found through a stable displacement experiment, when the porous matrix is saturated with the wetting fluid for the first time.

3.5 Experimental procedure

In this section we describe how an experiment was conducted, and how the model was refilled and prepared for the next experiment. The reader should notice the discussion about "jump-starting" of the experiment, as it will be of some importance for the measurement of saturation discussed in section 4.5.2.

3.5.1 Running an experiment

Before the experiment itself could be started, the temperature control system was turned on and monitored in LabView. As we waited for the the fluid-saturated porous matrix to reach a constant temperature; air and fluid syringes were filled, the gearbox was set to obtain the desired flow-rate and the image *fps* rate was set in LabView. When the temperature had stabilized, our LabView VI seen in figure 3.20 was executed and the pump system started.

In the first "try and fail" stages of the experiments, we experienced some problems with back-flow of wetting fluid into the air tubes, due to compressibility. This caused a considerable time delay before air could enter the model. Also, difference in tube diameters and lengths caused the air in various syringes to enter the porous matrix at very different times.

Backflow was prevented by mounting a three-way vent in each air tube, at the same distance (12 cm) from the inlet channels. This is shown in figure 3.30. The original air filled syringe was mounted to connector point A. To the connector point B, a fluid filled syringe was mounted so the region from C to the porous matrix could be filled with fluid. We will refer to this later as the initial volume of fluid in the air tubes, V_0. With the possibility of closing the connection between A and C, we where able to pump up some start pressure in the air tubes. This will be referred to as a "*jump start*" of the experiment. When the air pressure was high enough to prevent backflow, the three-way vents were flipped to make the connection between A and C. In this way, the initial volume V_0 was displaced towards the porous matrix immediately and no backflow was observed. To ensure that V_0 was displaced at the same rate through all inlet nodes, tube diameters and lengths were matched as good as possible for all syringes. After the connection between A and C had been made, the remaining eight inlet tubes containing the glycerol/water fluid were also opened for flow. This marked the start of the experiment.

The experiments were in all cases stopped right before each syringe piston had displaced a volume of 60 ml. To perform a new experiment the model had to be flushed. This is discussed in section 3.5.2.

Boundary conditions are important with respect to the displacement structure in this kind of experiments. Two phases can be fed into a porous medium in many ways. It is not a random
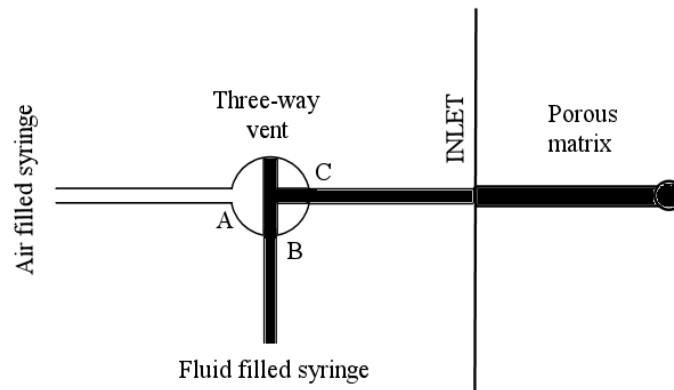
Figure 3.30: *Schematic figure of the connection of air-filled syringes to the flow model. A three-way went is mounted 12 cm from the inlet node. Initially there is no connection from the air tube to the porous matrix. This allows us to displace the syringe pistons before the experiment is started, to obtain overpressure in the tubes. When the connection between A and C is made, the overpressure at the air side will displace the fluid volume into the porous matrix right away. At the start of each experiment, the tube from C to the inlet is filled with wetting fluid, through the connected syringe at B.*

choice, nor a matter of convenience, that all of the fifteen inlet nodes are connected to separate syringes. We have chosen this setup to ensure uncorrelated injection of fluid from all nodes. If e.g all the air-inlet nodes were connected to one big syringe, the flow of air from one node would depend on the other nodes. Especially, if an invasion cluster from one node starts to outgrow the others, cases of inlet node short circuit might occur. This means that most of the air would be diverted into this particular node, since the most advanced invasion cluster experiences the highest pressure gradient. This is similar to the instability of viscous fingering, and would cause a non-homogenous channeling flow in the porous matrix. This could of course be interesting in its own respect, but it was not our intention to study such flows.

3.5.2   Flushing the model

Due to the good non-wetting properties of air, it is possible to recycle the porous matrix. By recycling we mean that the air is flushed from the system, leaving a porous matrix saturated with the glycerol/water fluid. The flushing consists in applying a high under-pressure at the outlet while injecting wetting fluid from all inlet nodes at a high flow-rate.

To obtain the under-pressure a 1 liter bottle filled with air, containing two tube connectors, are used. One connection is made to the model outlet, initially sealed off by a two-way vent, while the second connection is made to a vacuum pump. The vacuum pump is left to run for about one minute, before its connection to the bottle is sealed off. The pressure in the bottle is now considerably below atmospheric pressure. The two-way vent that separates the outlet from the bottle, are then opened and at the same time, fluid is injected at the inlet. This causes the air in the porous matrix to rapidly migrate to the outlet, and in this way the model is flushed. The flushing is stopped when the effect of the under-pressure wears off, and fluid starts to accumulate in the bottle. It is usually difficult to get rid of all the air in one run, and so the process is repeated three or four times.

It is important when flushing, that the tube reaching from the porous matrix to the bottle, does not contain fluid. If fluid is present, there will be a considerable viscous pressure drop through the tubes, and the flushing effect will wear off much faster.

Flushing of the porous matrix saves an enormous amount of tedious experimental work. It means that one matrix can be used for all experiments. Changing of the porous matrix means first of all making a new one, and additionally, dismounting the model to make the replacement.

Chapter 4

Results and discussion

In this chapter we will present and discuss our experimental findings. The diversity of simultaneous flow in porous media is truly striking. Also, the compressibility of air introduces effects not encountered in classical regimes.

We will start with a description of the observed displacement structure and dynamics, from the invasion phase to steady-state. Many similarities have been found between the two regimes. The pressure development and the relation to the observed dynamics is then considered. Due to good synchronization of the data sources, events in the pressure curves can be related with a high degree of accuracy to captured images.

Due to the size of the model, pressures are high and compressibility effects of air are important. A highly dynamic effect is the occurrence of bursts of compressed air, propagating through the porous matrix. Compressibility also affects the imposed flow-rates of non-wetting fluid, as will be discussed.

The saturation is difficult to determine exactly in an experimental setting. We have used three different methods, all yielding consistent results. We hope to compare the found values with numerical simulations.

Towards the end of this chapter the behavior of statistical properties of non-wetting clusters are considered, both during invasion and steady-state.

4.1   Experiments performed

During this work, many experiments were done, both successful and unsuccessful. A new experimental setup is always accompanied by an initial stage of try and fail, and the time frame is often longer than expected. This seems to be the rule, rather than the exception when it comes to experimental work.

The first improvement to the experimental setup was to change the lightbox, due to intensity gradients (section 3.1.5). We also spent some time struggling with backflow of fluid into the air tubes. It turned out that this was due to leaks in some of our three-way vents. In high flow-rate experiments we encountered for the first time that the pressure inside the porous matrix exceeded that of the supporting pressure cushion. This caused a non-constant pore-space volume, making the data incomparable with other experiments.

Only a small portion of the phase space has been explored in the experiments. Table 4.1 summarizes the characteristics for each experiment analyzed in this chapter. During the winter and spring of 2006/2007, two series of successful steady state experiments were performed. In all experiments, the only tuning parameter was the wetting fluid flow-rate Q_w. It was increased from 0.2 ml/min to 4.5 ml/min, in a total of five experiments pr. series. Due to compression, the flow-rate of air is a more complicated parameter, see section 4.4. We do find that it is constant during the invasion phase, but takes a lower value than predicted by the syringe pump. At this stage we simply introduce the flow-rate of air during the invasion as Q_{nw}^{inv}. This flow-rate

Experiment #	Q_w [*ml/min*]	Q_{nw}^{inv} [*ml/min*]	Ca	t_b [*hours*]
motor200	0.22	0.13	0.0079	9.2
motor100	0.44	0.23	0.015	4.8
motor50	0.91	0.38	0.032	2.6
motor20	2.23	0.66	0.090	1.0
motor10	4.42	1.30	0.17	0.5

Table 4.1: *Characteristic data in a series of five experiments. In columns from left to right: Syringepump setting, wetting fluid flow-rate, non-wetting fluid flow-rate, capillary number and breakthrough time t_b. The capillary numbers were calculated using eq. 2.58 with $Q_{tot} = Q_w$.*

Cross section of porous matrix,	$A = 4.08 \pm 0.04 \, \text{cm}^2$
Length of porous matrix,	$L = 83.1 \pm 0.4 \, \text{cm}$
Porosity,	$\phi = 0.63$
Surface tension,	$\gamma = 0.064 \, \text{N/m}$
Estimate of static contact angle,	$\theta \approx 33°$
Absolute permeability,	$K = 1982 \, \text{Darcy}$
Average glass bead diameter,	$b = 1 \, \text{mm}$
Number of pores estimate,	~ 213600
Viscosity ratio in the order of,	$M = \frac{\mu_{nw}}{\mu_w} \sim 10^{-4}$
Glycerol/water density,	$\rho_w = 1.217 \, \text{g/ml}$

Table 4.2: *Constant parameters from the experiments.*

varied in the range 0.12 ml/min to 1.29 ml/min. In the first series of experiments images of the whole porous matrix were captured, at a resolution of ~ 20 pixels pr. bead. In the second series, a smaller region was imaged at a resolution of ~ 40 pixels pr. bead. Two series of experiments were performed for two reasons, 1) higher resolution was needed to do a proper image analysis, and 2) we wanted to check the consistency between experiments. In table 4.2 some of the important experimental parameters are listed.

The breakthrough time t_b, is less than half of the total duration of an experiment. The fastest and the slowest experiment lasted ~ 2 and ~ 24 hours respectively. Fast and slow experiment, shall here mean high and low flow-rates respectively.

4.2 The displacement structure

In this section we will describe the structure observed in our experiments, from the invasion phase to steady-state. Figure 4.1 and 4.2 show a time series of the slowest and fastest experiment, Ca = 0.0079 and 0.17 respectively.
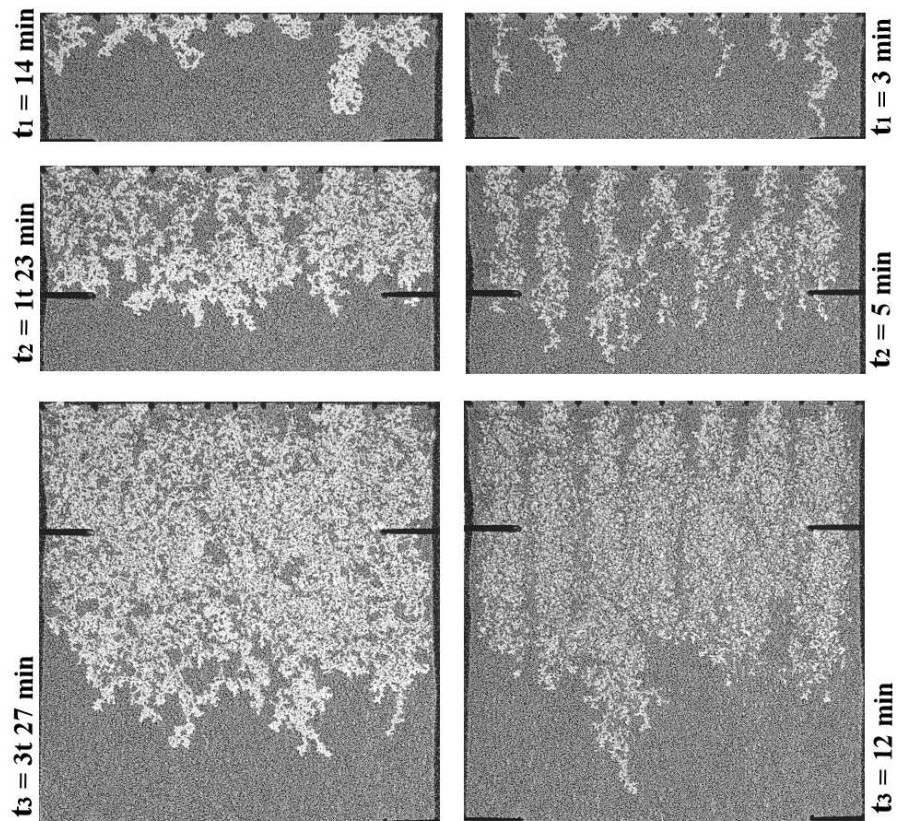
Figure 4.1: *Time series (t_1, t_2 and t_3) of the invasion phase for a Ca $= 0.0079$ (left) and a Ca $= 0.17$ (right) experiment. In both cases the degree of fragmentation and mixing increases with time. The wetting fluid is displaced by several independent non-wetting clusters. In the right column channel flow can be seen. This signature of the boundary conditions is gradually wiped out with time. In the left column virtually no signature effect is observed.*
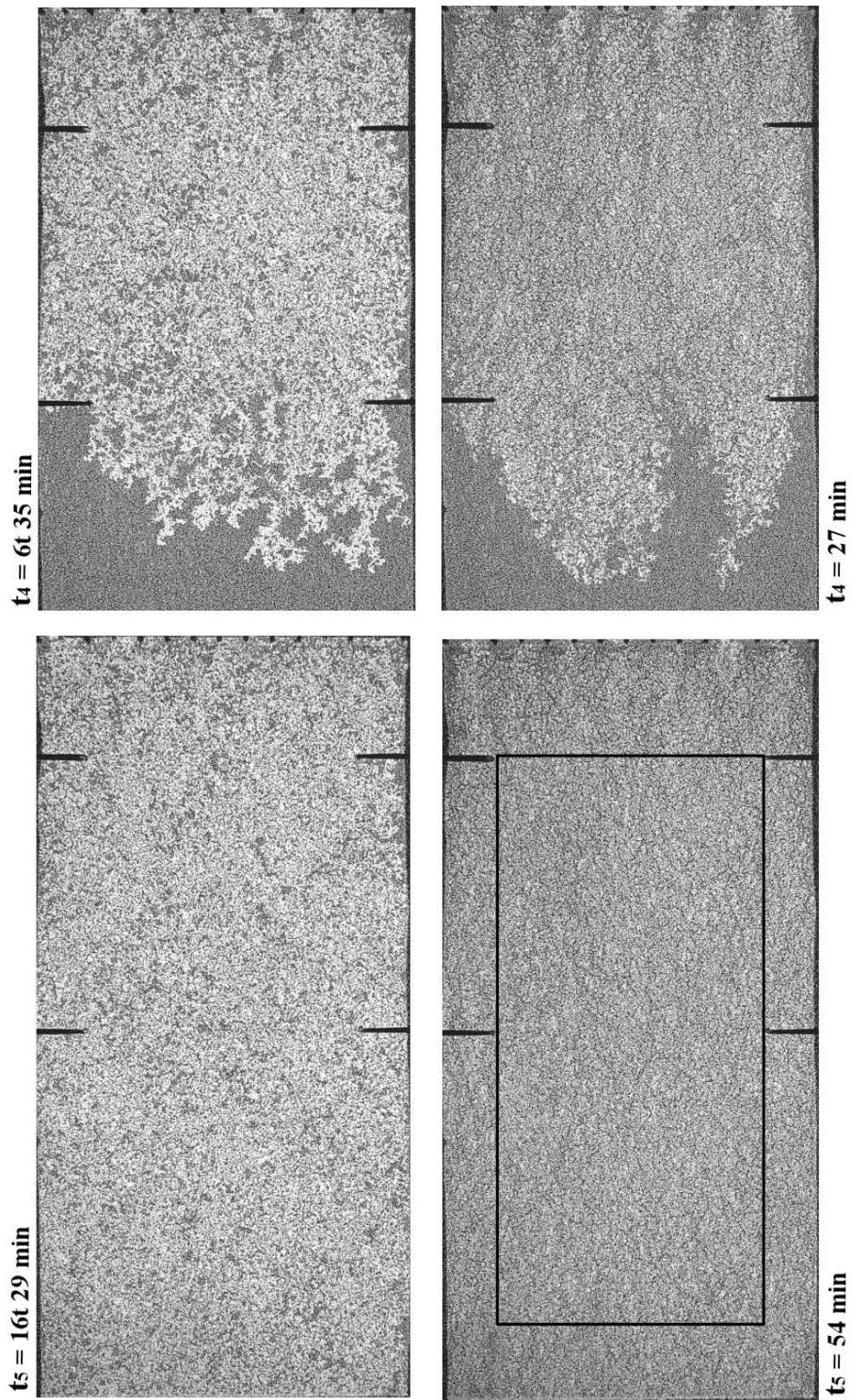
Figure 4.2: *Continuation of figure 4.1. The timestep t_4 shows the middle stage of the invasion phase. The homogenous region dominates the structure in both cases. At t_5 the systems are in steady-state. The whole porous matrix contains a homogenous mix of the two phases. Note that the homogenous region in t_4 is similar to that of later steady-state. The region bound by the rectangle in the bottom right image, shows the area considered during image analysis.*

4.2.1 Initial transients

When air enters the model, in the very first stages of displacement, continuous clusters are observed from all seven inlet nodes. The observed structure have similarities to that of capillary- or viscous fingering, for low and high Ca respectively, as shown in figure 4.3. At the same time, the

Figure 4.3: *The first stage of air invasion. In both images a cropped section from one of the seven air inlet nodes are shown.* **a)** *Invasion cluster at Ca = 0.0079. The structure inside the air cluster resembles that of capillary fingering with trapped clusters of different sizes.* **b)** *Invasion cluster at Ca = 0.17. Almost no trapping of wetting fluid occurs, and the structure is similar to that of early stage viscous fingering.*
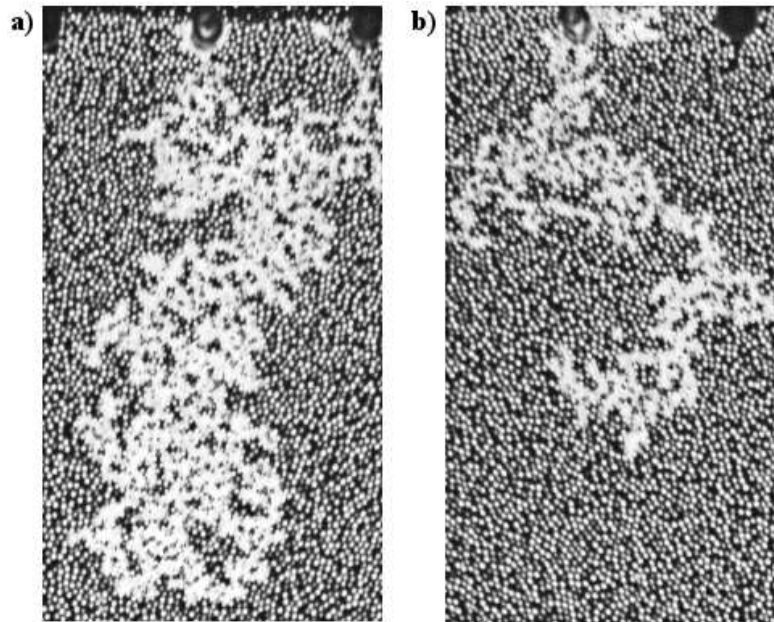
inlet pressure increases while the middle- and outlet pressure were virtually unchanged. This is reasonable, since the permeability will decrease locally at the inlet, whereas the permeability in the middle- and outlet region will remain unchanged. Figure 4.4 shows the pressure development at Ca = 0.17. We defer a more thorough discussion to section 4.3.
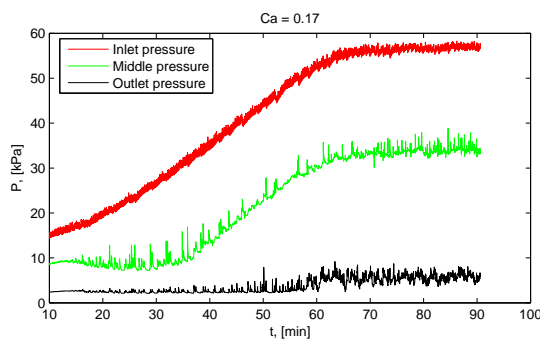
Figure 4.4: *Pressure development $P(t)$ at the inlet, middle and outlet of the porous matrix.*

The air clusters were only connected to the inlet node for a short period of time. As the local pressure increased and the clusters grew in length, the snap off effect became evident. Non-wetting clusters were disconnected and infiltrated by the wetting fluid, and the contours of mixing started to show. This behavior was prominent in all stages of our experiments. Due to the simultaneous flow of invading and defending fluid, there is a competition between drainage and imbibition, (section 2.5). As the invasion progressed, an increase in fragmentation and mixing

of the two phases were observed. The glycerol/water fluid was displaced from the model by numerous mobilized air clusters. The measured inlet pressure also continued to increase. This increase in pressure, is due to the continuous decrease in wetting permeability. Since the non-wetting saturation increases, less flow paths are available to the wetting fluid. The permeability of the wetting phase will additionally depend on the flow dynamics. The non-wetting clusters are either trapped or mobilized. Trapped clusters are seen as obstacles, whereas mobilized clusters must be transported through the porous matrix by the wetting fluid. To transport a non-wetting cluster, capillary barriers must be overcome continuously in multiple migration steps. As the fragmentation increases, the pressure must increase accordingly for the wetting fluid to be able to go round and transport clusters at the same constant flow-rate.

In contrast to the classical flow regimes, the displacement front consists of independent non-wetting clusters surrounded by wetting fluid. Thus, it is not possible to find a connected front of non-wetting fluid. In this respect, we define the position of a point along the front as

$$x_f(y,t),\tag{4.1}$$

where x_f is the distance, at a given position y along the outlet, from y to the first encountered wetting/non-wetting fluid interface, at time t. The *front* shall then mean the line segment (possibly fractal) of points x_f, over the width of the model. By the *front width* we shall mean the standard deviation of the front.

The displacement front and structure during the initial stage of invasion, are shown in figure 4.1 for two experiments. In the right column the flow-rate is high, and entering air clusters are fragmented almost immediately. As more and more air enters the model, the degree of mixing of the two phases increase. At time t_1 and t_2 eight channels are observed, only subjected to flow by the glycerol/water fluid. The remaining seven channels contains flow of both air and glycerol/water. This flow is the signature of the boundary conditions. At $t = t_3$ the channeling flow is less prominent, but can still be seen. During the last stages of invasion, the signature of the boundary conditions can only be seen in a region close to the inlet, as shown at timestep t_4 in figure 4.2. To the left column in figure 4.1 the time series of a low flow-rate experiment is shown. In this case the invasion clusters are larger, and virtually no signature of the boundary conditions can be observed. The clusters can exist over larger length scales as predicted by eq. 2.75, and a more heterogenous structure is observed at the displacement front.
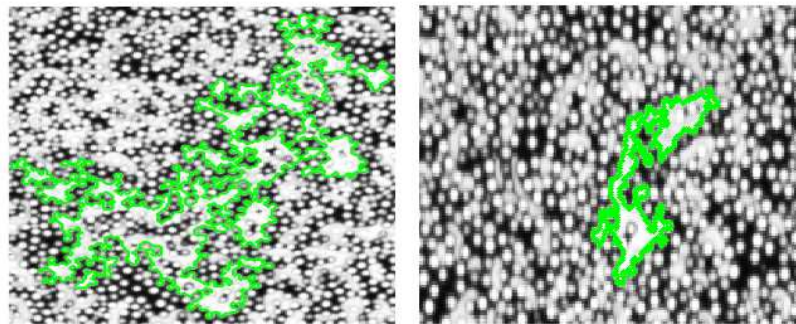
Figure 4.5: *To the left: Largest air cluster in the homogenous region of a Ca = 0.015 experiment. Flow direction is from top to bottom. The shape is branched in between regions of glycerol/water fluid. The length of the cluster in the flow direction in units of beads is l/b = 38. To the right: Similar to the left figure, but Ca = 0.17. The cluster is elongated and considerably smaller, l/b = 15.*

In the early stages of invasion, we emphasized that the degree of fragmentation and mixing of the two fluids increased as air entered the model. However, this behavior did not continue at the same rate in the mid and final stages of the invasion phase. When the front had advanced about half the length of the model, the structure of the air-invaded part could be divided into two

regions. The first region contained the largest air clusters, with little trapping and infiltration of wetting fluid. These clusters were found along the front. Further behind, the clusters were gradually infiltrated and fragmented by the wetting fluid. Thus, the region was heterogenous in the direction of flow. A part of the heterogenous region is shown for a high- and low-Ca experiment in the upper and lower left image of figure 4.6. In the second region, somewhat behind[1] the front, a homogenous mix of air and glycerol/water was found. This is shown in the upper and lower right image of figure 4.6. If we also compare the heterogenous and homogenous region for the two experiments, we note that the heterogenous region is considerably smaller in the high-Ca experiment. That is, in the upper left image one does only have to go a short distance away from the front, before the structure looks very similar to that of the upper right image. This is not the case in the low-Ca experiment. Even though some of the air clusters in the homogenous region were large in size, they had a non-compact, maze-like shape, infiltrated by the glycerol/water fluid. Thus, it is hard to separate one cluster from another by visual inspection. The largest cluster in the homogenous region in a high- and low-Ca experiment is shown in figure 4.5. As discussed in
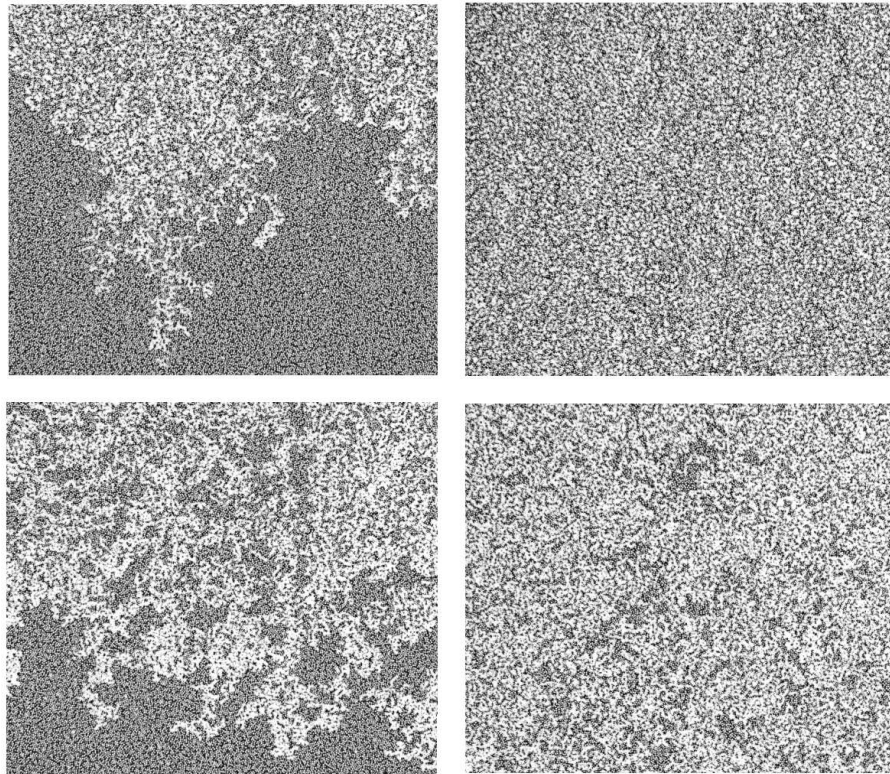
Figure 4.6: *Cropped sections of size* 23 × 23 *cm, from a fast (upper part) and a slow (lower part) experiment.* **Upper left***: Heterogenous region, Ca* = 0.17. *The biggest clusters are found at the front. For fast experiments, homogenous mixing of both fluids are observed very close to the front. Thus, the heterogenous region is small.* **Upper right***: Homogenous region, Ca* = 0.17. *The high degree of mixing is evident.* **Lower left***: Heterogenous region, Ca* = 0.0079. *Compact regions of air and glycerol/water are observed close to the front. More fragmentation and mixing, are observed further behind.* **Lower right***: Homogenous region, Ca* = 0.0079. *Contrary to the upper right image, the non-wetting clusters and the regions of glycerol/water are larger.*

section 2.5, the largest cluster in a high flow-rate experiment will be smaller compared to that of a low flow-rate experiment.

---

[1]There is no well-defined transition between the two regions of the air invaded part of the porous matrix.

We observed visually that the degree of fragmentation and mixing of fluids in the homoge-nous region had stabilized. In fact, the structure was very similar to that of later steady-state, as seen in figure 4.2. This suggests a stabilization also of local permeability. By stabilization we mean only a small variation with respect to time, of the mean time averaged permeability. Time averaging is used because the interfaces at the pore scale change with time as clusters move, co-alesce, get trapped or snapped off continuously. Later analysis showed that already during the mid part of invasion, the saturation, pressure gradient and distribution of clusters in the homoge-nous region were quite close to that of steady-state. It is a just question why the two fluids mix the way they do in the homogenous region, and why the non-wetting clusters are more compact and distinguishable towards the front. We defer this discussion to section 4.2.3.

For each experiment the breakthrough time t_b and steady-state time t_{ss} was measured. t_b is defined as the time difference between the two events of air entering the model from all inlet nodes, and the first cluster of air reaching the model outlet. t_{ss} is defined similarly, but the second event is now the time at which pressure stabilizes and steady-state is reached (see figure 4.4). Figure 4.7 shows t_b and t_{ss} as a function of $Q_w + Q_{nw}^{inv} = Q_{tot}^{inv}$. The superscript ^{inv} is used to mark that the non-wetting flow-rate is different during invasion and steady-state, which is an effect of compressibility. We will return to a discussion of this point in section 4.4. The measured
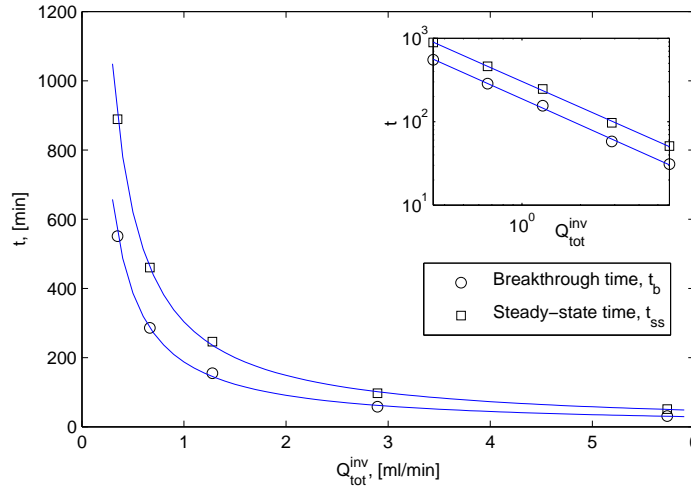
Figure 4.7: *Measured breakthrough time t_b and steady-state time t_{ss} as a function of the total invasion flow-rate Q_{tot}^{inv}. Each set of data points is fitted to a power-law $t_i \propto \left(Q_{tot}^{inv}\right)^{-\alpha}$. This is also shown in the inset. The time difference between breakthrough and steady-state, $t_{ss} - t_b$, from the slowest to the fastest experiment is given by: $(338, 174, 91, 39, 20)$ min respectively. We also note that the relative time difference, $(t_{ss} - t_b)/t_b \approx 0.62$, is constant for all experiments.*

breakthrough and steady-state time were found to follow a power-law of the form,

$$t_b = V_b \left(Q_{tot}^{inv}\right)^{-\alpha_b} \tag{4.2}$$

$$t_{ss} = V_{ss} \left(Q_{tot}^{inv}\right)^{-\alpha_{ss}}, \tag{4.3}$$

where V_b and V_{ss} are pre-factors such that the right hand side of eq. 4.2-4.3 has the unit of time. A fit was made to the data sets in figure 4.7, and it was found that,

$$\alpha_b = \alpha_{ss} = \alpha = 1.03 \pm 0.05. \tag{4.4}$$

It is not obvious that our system, where one of the phases is highly compressible, should have this power-law behavior with $\alpha \sim 1$. However, assume that a simultaneous displacement at

constant flow-rate, using two incompressible fluids has a flat front. In this case, we would expect the front to break through the porous matrix at a time,

$$t_b^* = \frac{L}{u}, \tag{4.5}$$

where L is the length of the porous matrix and u the fluid velocity. Since $u = Q_{tot}/(A\phi)$, eq. 4.5 becomes,

$$t_b^* = LA\phi Q_{tot}^{-1} \tag{4.6}$$

$$= V_{ps}Q_{tot}^{-1}, \tag{4.7}$$

where $V_{ps} = LA\phi$ is the pore-space volume. We note that eq. 4.7 has the same form as eqs. 4.2-4.3, if we assume $\alpha \equiv 1$. Using this assumption, it follows that the pre-factors V_b and V_{ss} are volumes. Their fitted value of the data sets shown in figure 4.7 was found to be,

$$V_b = 187 \pm 16 \text{ ml} \tag{4.8}$$

$$V_{ss} = 303 \pm 17 \text{ ml}. \tag{4.9}$$

$$\tag{4.10}$$

The pore-space volume in our porous matrix is $V_{ps} = 214$ ml, so we have that,

$$V_b < V_{ps} < V_{ss}. \tag{4.11}$$

We conclude that for all experiments, a volume of ~ 187 ml and ~ 303 ml needs to be displaced from the porous matrix in order to reach breakthrough and steady-state respectively. Additionally the time difference between steady-state and breakthrough is given by,

$$t_{ss} - t_b = \frac{V_{ss} - V_b}{Q_{tot}^{inv}}, \tag{4.12}$$

and the relative time difference,

$$\frac{t_{ss} - t_b}{t_b} = \frac{V_{ss} - V_b}{V_b} = 0.62. \tag{4.13}$$

Eq. 4.13 states that the time difference between breakthrough and steady-state, for all experiments, is 38% of the breakthrough time.

4.2.2 Steady-state behavior

Some time after breakthrough, see figure 4.7, all measured pressures reach a plateau. Time averaged pressure, global saturation and various statistical properties reached constant values. Hence the criteria for a dynamical steady-state are met. The displacement structure during steady-state can be seen at timestep t_5 in figure 4.2. The whole porous matrix now consists of a homogenous mix of both fluids.

Regarding clusters, we have so far only considered non-wetting clusters. Some independent wetting clusters do exist, but they are highly outnumbered by the non-wetting clusters. Based on hours of visual observation and image analysis we have found that the wetting fluid percolates[2] the system at all times, not just in steady-state, for all experiments. This is consistent with the observation of Payatakes *et al.* [17, 18], that the wetting fluid percolated through a changing network of connected pathways and also wetting films in steady-state. For fast experiments the wetting saturation is quite high, and it is easily observed that the wetting fluid percolates. In this case, it is a very apt description to say that the non-wetting clusters are embedded in a

---

[2]By a percolating fluid, we shall mean that it has a connected pathway from the inlet to the outlet.

background field of wetting fluid. When it comes to slow experiments the wetting saturation is lower, and due to the larger non-wetting clusters infiltrated by wetting fluid, it is harder to determine the connectivity of the percolating wetting cluster. It is best described as an interchanging network of compact regions connected by thinner channels. The channels are elongated and not more than a pore size wide on average. The wetting fluid in these channels is often observed to bypass glass beads or even larger non-wetting clusters through thin films. Some aspects of the connectivity of the wetting fluid are shown in figure 4.8. A percolating wetting cluster is favored,
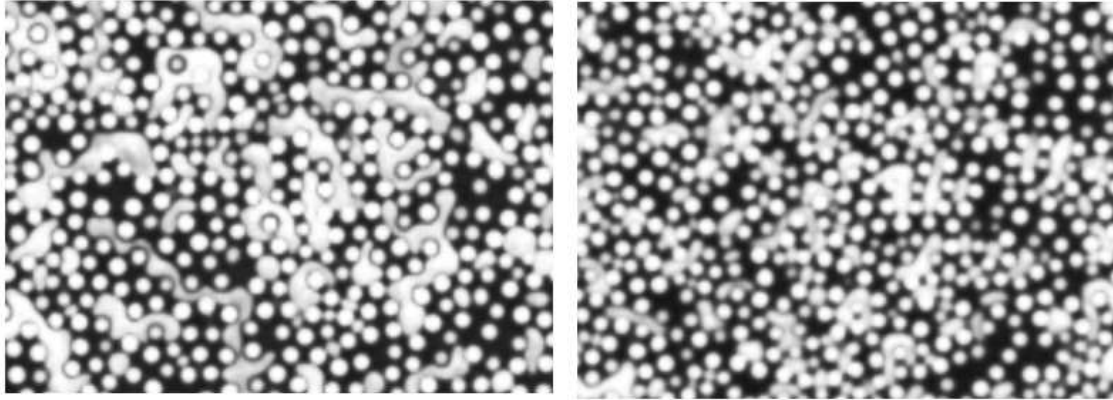

Figure 4.8: *Cropped sections at pore-scale resolution from Ca = 0.015 (left image) and Ca = 0.090 (right image) experiment.* **Left image:** *The compact regions of wetting fluid (black) are connected by thinner channels. The glass beads are bypassed through films of wetting fluids. Notice also the fluid film surrounding some of the darker air (white) clusters.* **Right image:** *Air clusters are in this case much smaller, and wide regions of the glycerol/water fluid are connected over larger distances.*

not only by good wetting conditions, but also as a consequence of the snap off and fragmentation effect. Hence, the low viscosity ratio[3] should contribute to the connectivity of wetting fluid over large distances.

As discussed in section 2.5.4, Payatakes introduced four flow-regimes based on the observed displacement structure in steady-state. In this regard, the flow dynamics observed in our experiments would be best described as *small ganglion dynamics* for high-Ca experiments, and *large ganglion dynamics* for low-Ca experiments. The main difference between these regimes is the average size of moving non-wetting clusters. During steady-state, smaller clusters were usually trapped and only performed sporadic migration steps. Medium and large clusters were observed to be able to move over larger distances before getting either trapped or fragmented. As we have mentioned before, these moving clusters can also mobilize smaller trapped clusters. Thus, the pore scale dynamics will depend on the ability for clusters to coalesce.

There is one important aspect of the dynamics that have not been discussed so far, namely the effect of compressibility. As will become evident shortly, the pressures involved are large (inlet pressure at the order of ~ 0.5 bar during steady-state for the fastest experiment). One effect of compressibility, is the ability for air clusters to either expand or contract. To displace fluid, the air pressure must exceed that of the fluid. It goes without saying that a 60 ml air filled syringe, originally at atmospheric pressure, must be compressed quite a bit[4] to obtain a pressure increase of ~ 0.5 bar. Thus, if we consider an independent air cluster close to the inlet, it will have the possibility to expand as it moves towards lower wetting pressure at the outlet. In this case, the drainage steps will outnumber the imbibition steps so that the cluster volume increases.

Clusters will expand more and more as they move in the direction of flow. One could then assume that the largest clusters were to be found towards the outlet of the model. However,

---

[3]By low we mean $M \ll 1$.

[4]Actually the original volume must be reduced by a factor of $\sim 2/3$.

this does not seem to be the case in our experiments. We find that during steady-state, the non-wetting saturation and distribution of clusters do not change in the direction of flow. This behavior is to be expected for incompressible fluids, but is not obvious for compressible fluids. As of yet, we do not have a definite explanation of why this is so, but it should be kept in mind that the system under consideration is complex and does not consist of just a few clusters, but thousands. Additionally, expansion of clusters is not the only effect of using air. It is also a possibility for air clusters to be compressed. Compression occurs when the imbibition steps outnumber the drainage steps, resulting in a decreased cluster volume. Because of the many different flow processes (snap offs, migration, merging, trapping, expansion, contraction etc.) and the high density of capillary interfaces, the dynamics of different clusters are correlated. The possible correlation between contraction and expansion may cause pure migration or movement of clusters with little volume change. This can be an explanation as to why we do not see any difference in cluster distribution and saturation in the direction of flow.

A phenomena we will refer to as bursts, causes substantial expansion of non-wetting fluid. This is perhaps the most pronounced effect of air compressibility, and it is the topic of the next section.

4.2.3   Bursts of non-wetting fluid

Already during the invasion phase it was frequently observed that some of the air inlet nodes were completely clogged by a dense region of wetting fluid. This is shown in figure 4.9. As air
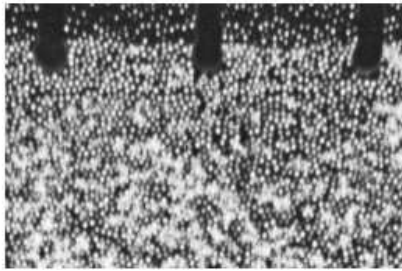

Figure 4.9: *Inlet node of air in between two inlet nodes of fluid. The region of the porous matrix, right in front of the air inlet node, is completely clogged by the glycerol/water mixture. To displace this region, the air must be further compressed to obtain the required pressure.*

was compressed further in the syringe, it started to invade slowly. Both the inlet and air pressure increased at a high rate during this invasion. When the invading air cluster had penetrated the compact region of defending fluid, it was observed to coalesce with the closest independent air cluster. At this point, a series of dramatic events with respect to pressure and displacement took place. During a short time interval, an avalanche of drainage and imbibition displacements was observed. Air propagated rapidly in a more or less straight path from the originating inlet note, and all the way to the displacement front. On its way, the expanding air caused fluid to be displaced not only in the direction of flow, but also considerably towards the sides of the model. At steady-state the avalanches propagated all the way through the model, and compared to the width of the porous matrix, the avalanche width was quite narrow. Following an avalanche was an abrupt decrease in the inlet and air pressure, whereas the middle and outlet pressures had a sudden jump. We will refer to these avalanches of drainage and imbibition as *bursts*.

Burst behavior have been studied in some of the experiments, both during invasion and steady-state, with a high-speed camera. Since a burst is highly dynamic, it is hard to visualize in one image. However, the method of image subtraction may be of assistance. If a region of the porous matrix is imaged over a small time interval, the pixel values of the initial image can be subtracted from those of the final image. The resulting image will reveal information of any changes. If the displacement structure is static during the time interval, pixel values are equal and the subtraction image will be black. Otherwise, changes in dynamics will show up as brighter regions. Figure 4.10 shows a burst during steady-state for two experiments. Bursts are observed regularly throughout an experiment. For each experiment the time differences between bursts
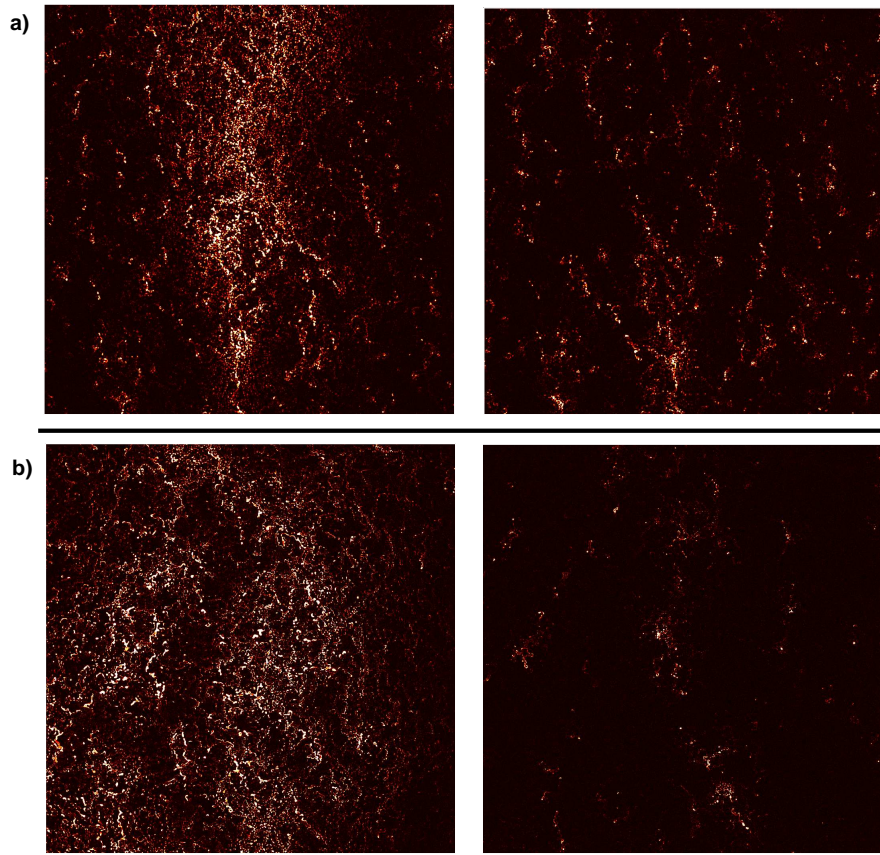
Figure 4.10: *A central region (17 × 17 cm) of the porous matrix is captured during steady state. Brighter regions indicate that displacement has taken place during the specified time interval Δt. Both drainage and imbibition steps are included in the image subtraction. **a)** Ca = 0.090, Δt ≈ 1s. The burst is seen to the left, and passes through the center region in roughly one second. For the sake of comparison, a "normal" displacement for the same Δt is seen to the right. **b)** Ca = 0.032, Δt ≈ 1.5s. Same as in a) but for a slower experiment. The burst (left) is wider and almost every part of the region is affected.*

were measured[5], and an average burst frequency f_{burst} was calculated. This is shown in table 4.3. From the table it follows that roughly 27 bursts occur before steady-state is reached. Based on the

Ca	f_{burst} $[min^{-1}]$	t_{ss} $[min]$	$f_{\text{burst}}t_{\text{ss}}$
0.0079	$\frac{1}{30}$	889	30
0.015	$\frac{1}{13}$	460	35
0.032	$\frac{1}{10}$	246	26
0.090	$\frac{1}{5}$	97	20
0.17	$\frac{1}{2}$	51	25

Table 4.3: *Average burst frequency f_{burst} for the whole system in five different experiments. As an example, for Ca = 0.0079 a burst occurs every 30 min. The frequency should be compared to the steady-state time t_{ss}*

---

[5]Time differences were found from the pressure curves in figure 4.14. Each burst gives a signature in the pressure measurements as will be explained in section 4.3.2.

burst frequency and the occurrence of bursts over the whole width of the model, the dynamics are bound to be affected. From the high speed camera images it was observed that during a burst, thin channels of air, elongated in the direction of flow, connected compressed air clusters over large distances. These channels were only "open" in a second, but within this time frame, there will be a considerable pressure gradient through the interconnected air cluster. This gradient in the non-wetting fluid pressure prevents snap-offs. However, as compressed air is transported to the front, where it expands into regions saturated with fluid, the gradient will decrease rapidly. As the pressure inside the air cluster relaxes, snap-offs "closes" the interconnecting air channels.

Air expansion at the front due to a burst is seen in figure 4.11. This figure serves to give a plausible explanation for the existence of a heterogenous and homogenous region during the invasion
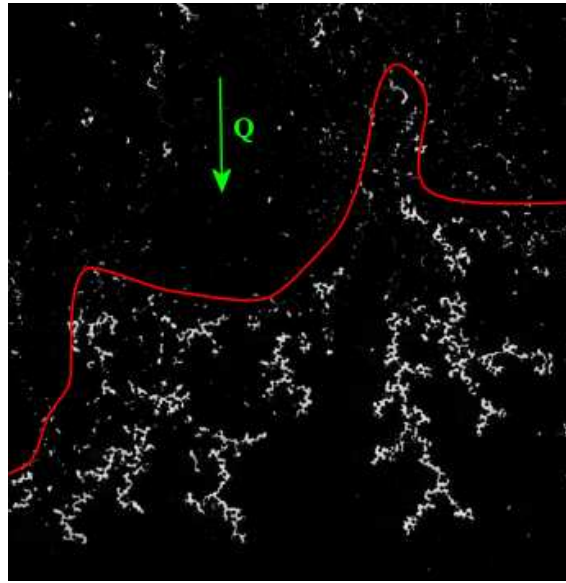

Figure 4.11: *Expansion of air during a burst at the displacement front in a 10×10 cm region for a $Ca = 0.090$ experiment. The solid red line marks the front at time t_0. At t_0 the burst has just reached the front line, and air is free to expand in the region saturated with wetting fluid. The green arrow shows the direction of flow. At time $t_1 = t_0 + 3s$, the burst has ended and the air clusters shown (white) are the result of the expansion. These clusters are considerably larger than those further behind in the homogenous region.*

phase, as discussed in section 4.2.1. When the burst propagates towards the front, wetting fluid is displaced both towards the sides and in the direction of flow, causing a local pressure increase. Thus, a series of correlated displacement events, originating from the burst, will take place and cause more mixing in the region behind the front. When the front is reached, compressed air expands in a lower pressure gradient and the resulting air clusters are larger than further behind. This burst behavior also affects the shape of the front.

In steady-state the burst propagates all the way to the model outlet. This distance ($L = 83$ cm) is large enough to visually observe that the the compressed air actually accelerates towards the outlet. This is consistent with the discussion in section 2.2.4 of compressible multi-phase flow (see figure 2.9). Bursts may also explain why the steady-state saturation and statistical properties do not vary in the direction of flow. It is possible that in a burst, interconnected air clusters release much of their compressed volume so that it is transported directly to the model outlet.

This kind of burst behavior is truly fascinating, and as far as we know, no previous studies have dealt with the phenomena. We have performed some early-stage analysis of pressure jumps during bursts and the time interval between bursts. It would also be interesting to look for any

correlations in the burst paths. That is, if the bursts tend to follow the same path through the porous matrix. This would reveal further information about the dynamics. However, time did not permit to pursue these topics any further.

4.3   Pressure measurements

During an experiment, the pressure was recorded at four locations: In one of the air tubes, at the inlet, at the middle and at the outlet. The detailed mounting and measuring points in the porous matrix are shown in figure 3.4 and figure 3.6 respectively. The sensors measure the local gage pressure in the porous matrix through a 5 mm diameter node. We will refer to these pressures as the air-, inlet-, middle- and outlet pressure. Even though the measurements are local, they reflect on average, the global pressure development fairly well. During steady-state, the pressure in different regions in a cross section orthogonal to the flow, are only separated by capillary fluctuations. Due to the size of our system, the capillary pressure fluctuations are much smaller than the global pressure.

4.3.1   Consistency check

Before the general behavior of the pressure is described, we comment on consistency. In the two series performed, the pressure curves from experiments with the same syringe pump-rate, are easily compared. From figure 4.12, it is apparent that the plateau pressure varies between the two series. The deviations are considerable for the $Ca = 0.17$ and $Ca = 0.090$ experiments. However, we see that the deviations in plateau pressures follow the average temperature difference between similar experiments. Thus, we expect viscosity differences in the wetting fluid to cause the inconsistency. The wetting fluid viscosity as a function of temperature is shown in figure 3.27. The largest variation in temperature between experiments are roughly $\Delta T \approx 2\,^\circ\text{C}$, which cause a difference of $\Delta \mu_w = 14$ cP in the wetting fluid viscosity. As a first order correction to the viscosity differences we use Darcy's law to relate the pressures in the two series of experiments,

$$v_w = \frac{k^e_{w,\#S1}}{\mu_{w,\#S1}} \frac{\Delta P_{\#S1}}{L} = \frac{k^e_{w,\#S2}}{\mu_{w,\#S2}} \frac{\Delta P_{\#S2}}{L}, \tag{4.14}$$

where $\#S1$ and $\#S2$ denotes the two series. The equality holds because the wetting fluid flow-rate is equal in both experiments. Further we assume that $k^e_{w,\#S1} \approx k^e_{w,\#S2}$. Eq. 4.14 then gives,

$$\Delta P_{\#S1} = \frac{\mu_{w,\#S1}}{\mu_{w,\#S2}} \Delta P_{\#S2}. \tag{4.15}$$

Eq. 4.15 offers a correction factor, that may be used to test if the deviations in pressure in the $Ca = 0.17$ and $Ca = 0.090$ experiments are caused by a difference in viscosity. The average temperature (shown bottom right in figure 4.12) for each experiment was measured with the thermistor, and the corresponding wetting fluid viscosity was found from figure 3.27. In figure 4.13, the pressure difference between the inlet and outlet is plotted as a function of time for the two Ca-numbers mentioned above. As can be seen from the figure, the plateaus are considerably closer, and we conclude that the viscosity difference is the main cause of inconsistency in the pressure curves. The deviation in plateau pressure between the two series of experiments, *after* using the correction factor, will be used as an estimate of the error. In the analysis in section 4.3.2 we will only consider the $\#S2$ series of experiments. Further, we also apply eq. 4.15 to all pressure curves within this series, to account for the viscosity differences. This is done by correcting all pressures by the factor $\mu_{\text{ref}}/\mu_{\#S2}$, where $\mu_{\text{ref}}(T = 20^\circ\text{C}) = 116\text{cP}$ is the viscosity of the wetting fluid at 20°C. Eq. 4.15 then becomes,

$$\Delta P = \Delta P_{\#S2,\text{ref}} = \frac{\mu_{\text{ref}}}{\mu_{w,\#S2}} \Delta P_{\#S2}. \tag{4.16}$$
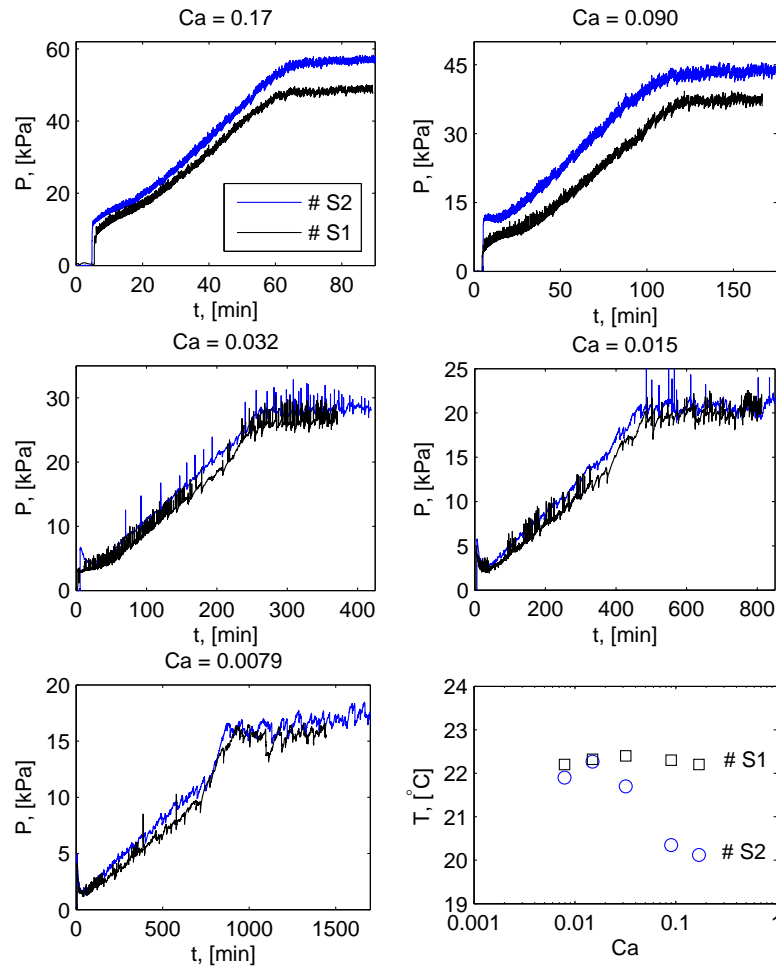
Figure 4.12: *Pressure consistency check between two series of experiments #S1 and #S2. Inlet pressure P as a function of time t. The two pressure curves in each plot are expected to reach the same plateau pressure. The bottom right plot shows the average temperature difference in the porous matrix for each experiment. For Ca = 0.17 and Ca = 0.090 the deviations are considerable. The reason is the temperature difference between the experiments, which causes a difference also in the wetting fluid viscosity.*

Note that the capillary numbers used in the analysis are calculated with the same wetting fluid viscosity μ_{ref}. This consistency check teaches an important lesson; temperature control is important whenever the fluid viscosity depends strongly on temperature.

4.3.2 Pressure development

The pressure has a characteristic behavior for all experiments, as shown in figure 4.14. The abrupt jump followed by a slow decrease initially, is a consequence of the overpressure in the air tubes, used to jump start the experiments as explained in section 3.5.1. As air enters the model and a displacement front is formed, the inlet pressure starts to increase. At this point the middle and

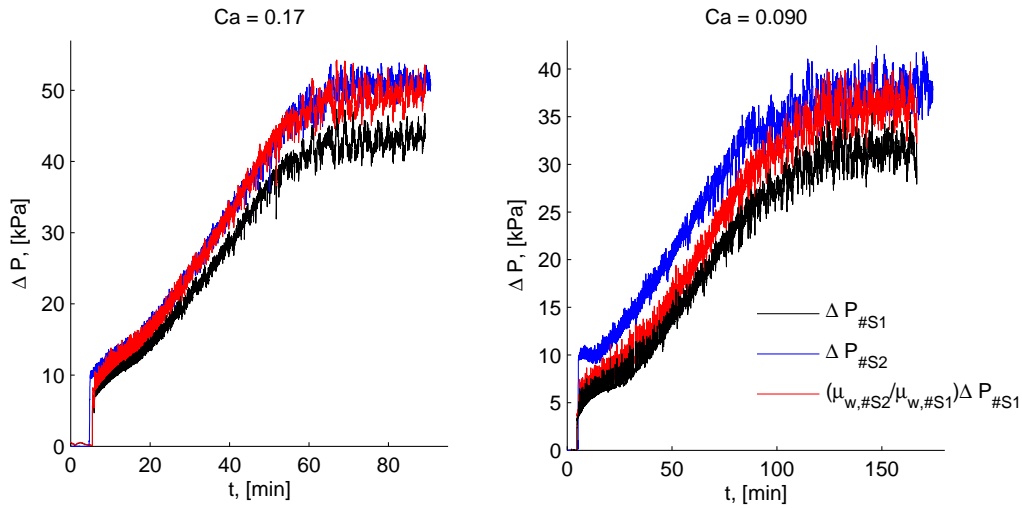**Figure 4.13:** *Pressure difference, $\Delta P = P_{inlet} - P_{outlet}$, as a function of time t, for the capillary numbers $Ca = 0.17$ and $Ca = 0.090$, in the two series of experiments #S1 and #S2. When applying the correction factor of eq. 4.15, the two series are more or less consistent. The temperature difference for both Ca-numbers are roughly, $\Delta T \approx T_{\#S1} - T_{\#S2} = (22.2 - 20.2)°C = 2°C$. This gives a correction factor of $\mu_{w,\#S2}/\mu_{w,\#S1} = 115cP/101cP = 1.14$ to the $\Delta P_{\#S1}$ pressure curves.*

outlet pressures show only a slow increase, and are separated by a single-phase viscous pressure drop. When the displacement front reaches the middle pressure sensor, a significant increase is observed also here. As the front passes by, and the start of the homogenous region reaches the sensor, the slope is very similar to that of the inlet pressure. After breakthrough, at time t_{ss}, the pressures reach different plateaus and a steady-state is obtained. The outlet pressure is observed to make a "jump" to the plateau during the transition from the invasion phase to steady-state. For all experiments the air pressure is slightly larger than the inlet pressure. This is to be expected, since the air and fluid must at least be separated by a capillary pressure difference.

As can be seen from figure 4.14, the pressure curves are not smooth. There are two causes for the fluctuations and spikes observed, 1) capillary fluctuations due to the continuous moving of menisci, and 2) the existence of bursts. The typical capillary pressure in a porous medium with a characteristic pore throat a, is approximated as [34], $P_c \approx 4\gamma/a$. Using the constants from table 4.2, and $a = 1$ mm, the fluctuations due to the many interfaces are of the order, $P_c \approx 256$ Pa. This is considerably less than the measured pressure differences over the model, which are of the order 10^5 Pa. The larger spikes and pressure drops seen in figure 4.14 are due to the bursts. A zoom in of the air-, inlet- and middle pressure curves for the Ca = 0.015 experiment is shown in figure 4.15. When highly compressed air leaves the inlet node and starts to expand during a burst, the pressure will rapidly decrease in the air tube and at the inlet, as shown in event (1) and (3). When the burst passes the middle pressure sensor, the expanding air causes a pressure jump/spike. Note that the spike shown in event (2) in the middle pressure curve does not have a corresponding pressure drop in air and inlet pressure. We believe this to be bursts originating from nodes far away from the location of the inlet and air sensor. The height of each spike caused by a burst, in the middle pressure curve, has been measured for the experiments. From the collected statistics, the mean spike height ΔP_{burst} was calculated. Spike height vs. Ca is shown in figure 4.16. We see that the pressure difference in a spike is in the range $(1.6, 3.4) \times 10^3$ Pa.
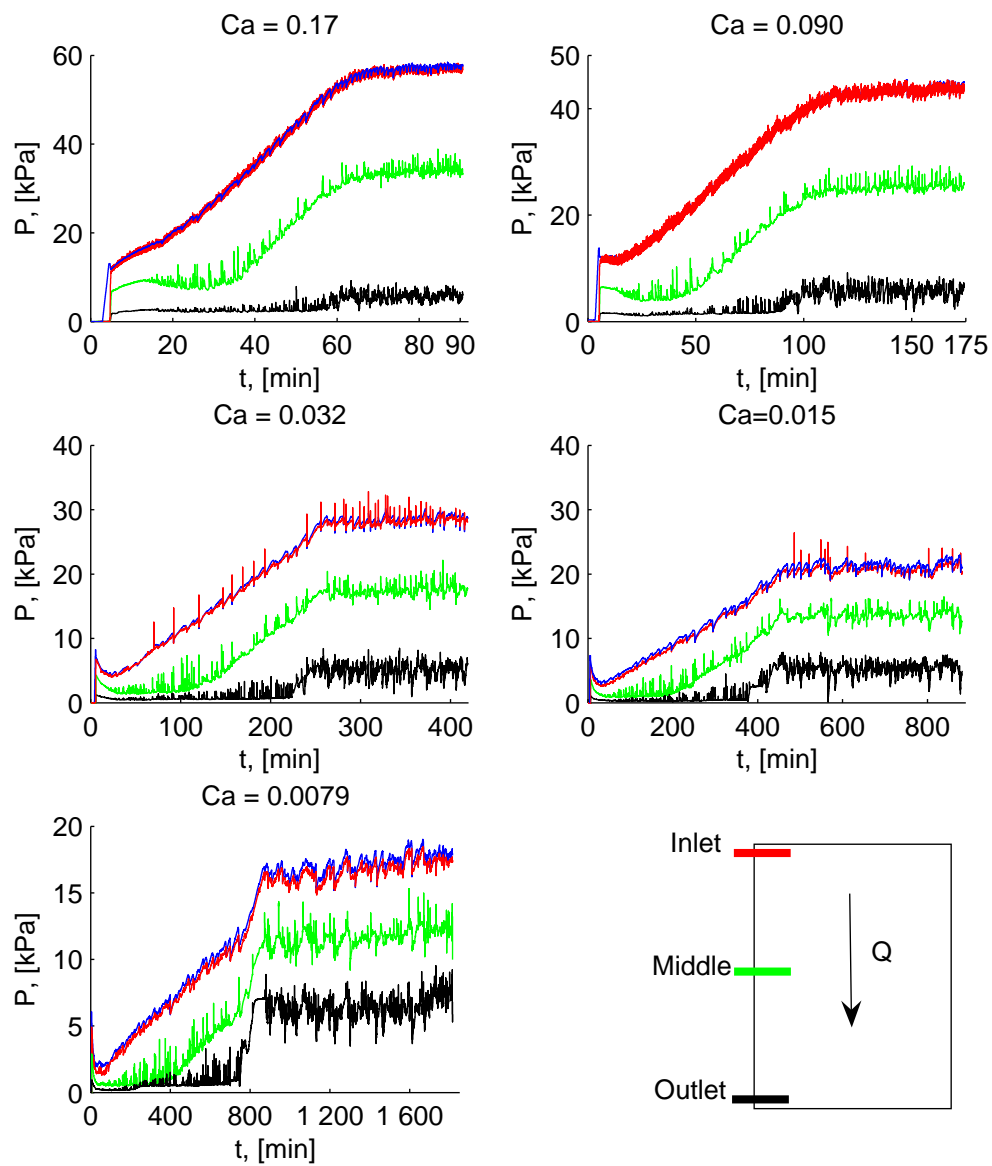
Figure 4.14: *Pressure P for all five experiments as a function of time t. The bottom right schematic figure, shows the sensor location in the porous matrix. The air pressure sensor (blue) is located in a tube outside the matrix. The pressure development has the same behavior for all experiments. When the invasion front reaches the sensor, pressure increases until a plateau is reached in steady-state.*
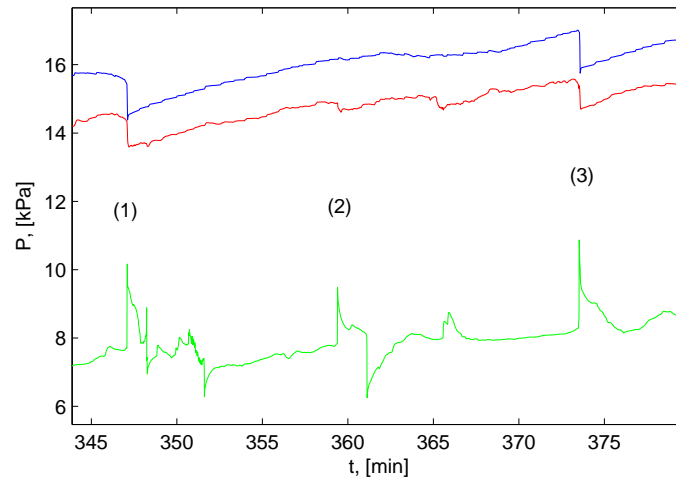
Figure 4.15: *Air, inlet and middle pressure in a $Ca = 0.015$ experiment, some time during the invasion phase. Three events (1), (2) and (3) are marked. The events correspond to bursts propagating through the porous matrix. After the burst has "left" the inlet node, the air and inlet pressure drops. A short instant later when the burst reaches the middle pressure sensor, a jump is observed.*
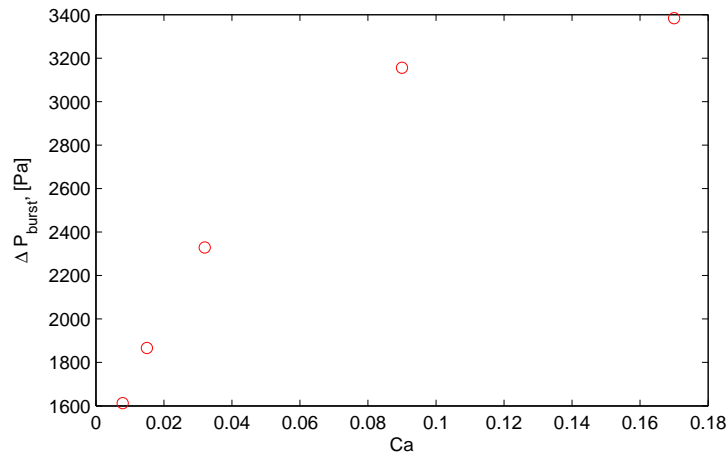
Figure 4.16: *Average pressure jump, caused by bursts, at the middle pressure sensor ΔP_{burst} as a function of the Ca-number.*

In section 4.2.1 we discussed the invasion structure, and that it could be divided into two regions; one heterogenous region along the front, and a homogenous region further behind. We argued that since the degree of mixing and fragmentation had stabilized in the homogenous region, we would expect stabilization also of the permeability. This is verified by the pressure measurements. Figure 4.17 shows the pressure differences $\Delta P_{I,O}$ and $\Delta P_{I,M}$, between the inlet/outlet and inlet/middle respectively. It can be seen from the figure that $\Delta P_{I,M}$ reaches a plateau relatively early, long before steady-state time. This plateau is maintained throughout the experiment. Each of the three points shown in every plot of figure 4.17, is associated with an image of the displacement structure at this time. The middle point corresponds to the time at which the pressure in the middle sensor starts to increase significantly. The point to the left shows the time when the pressure of the middle sensor increased only slowly. The right point shows the time at which the middle pressure increased at a slope very close to that of the inlet pressure. The corresponding images are shown in figure 4.18. In the first image column the node of the pressure sensor is completely surrounded by wetting fluid. In the second column the air has just reached the node of the sensor, and finally in the third image column the node is surrounded by a homogenous region of air and glycerol/water. At this time and throughout, we conclude on the basis of the generalized Darcy equations, that the relative permeability of both air and glycerol/water should be stable in the homogenous region between the middle and inlet sensor.
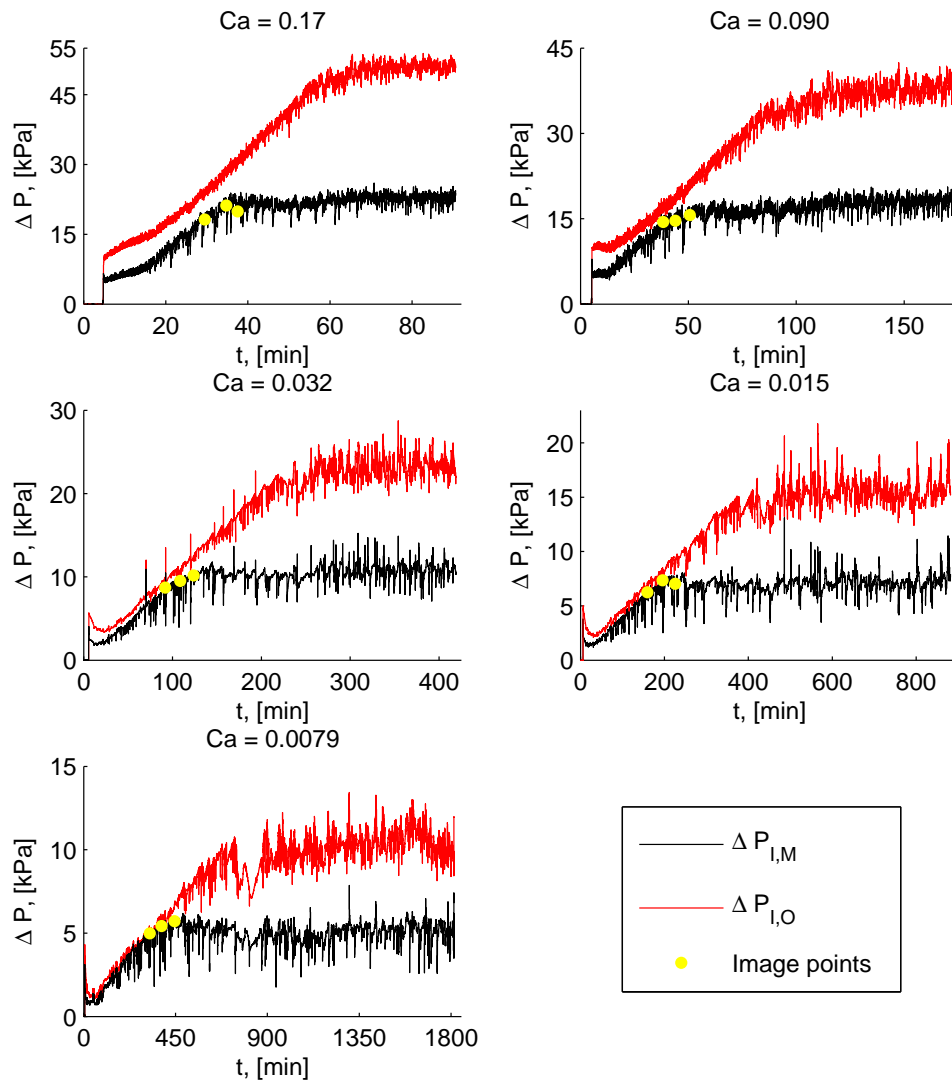
Figure 4.17: *Pressure differences $\Delta P_{I,O}$ and $\Delta P_{I,M}$, between the inlet/outlet and inlet/middle respectively as functions of time t. The three points in every graph of $\Delta P_{I,M}(t)$, corresponds to a time series of the displacement structure. These images are shown in figure 4.18. Note that the plateau of the $\Delta P_{I,M}(t)$ curve is reached long before steady-state time. Steady-state time is the time at which $\Delta P_{I,O}$ reaches its plateau.*
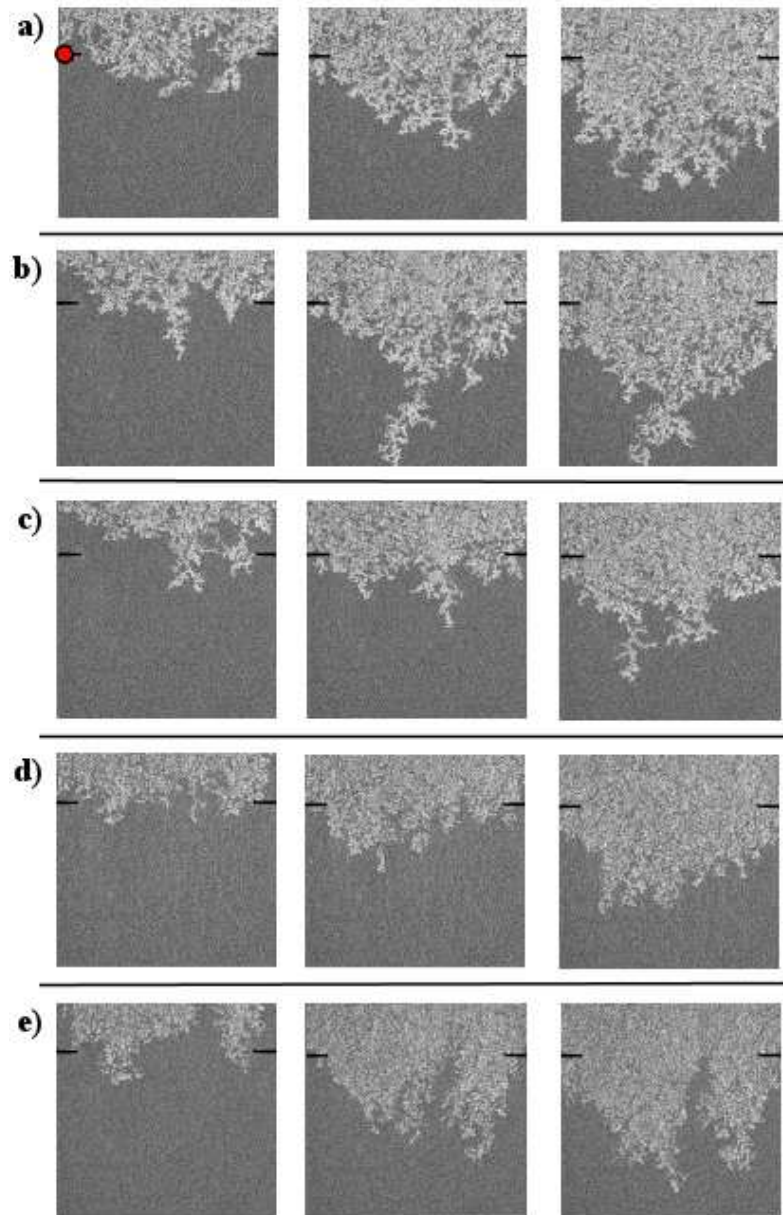
Figure 4.18: *Time series corresponding to the points in figure 4.17.* **a)** *Ca = 0.0079. The circle indicates the position for the middle pressure sensor.* **b)** *Ca = 0.015.* **c)** *Ca = 0.032.* **d)** *Ca = 0.090.* **e)** *Ca = 0.17. Note that in all experiments the most advanced part of the front is found towards the middle of the porous matrix.*

For all experiments, the time averaged plateau values of $\Delta P_{I,O}$ were measured. We refer to these values as ΔP_{ss}. Figure 4.19 shows the measured values as a function of the wetting fluid flow-rate Q_w. It is found that the steady-state pressure difference is a power-law in Q_w
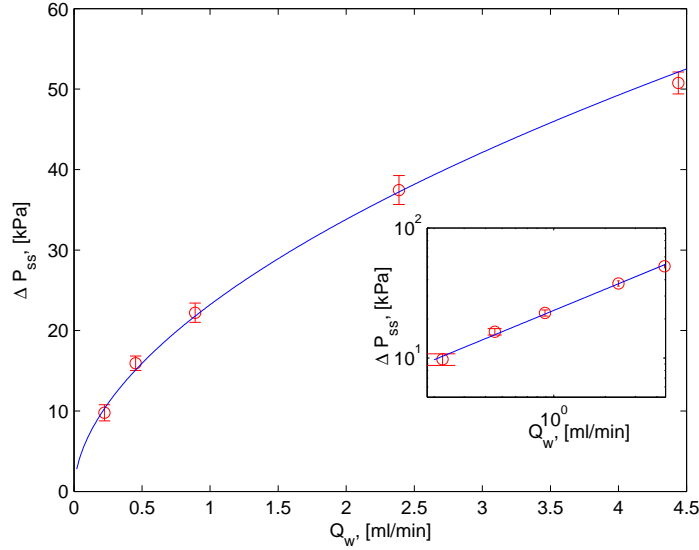
Figure 4.19: *The time averaged pressure difference over the model during steady-state ΔP_{ss} as a function of the wetting fluid flow-rate. The error bars stems from the variation in temperature between different experiments. The measured points are seen to follow a power-law in Q_w. This is shown in the inset.*

$$\Delta P_{ss} \propto Q_w^{\beta}, \tag{4.17}$$

with the exponent

$$\beta = 0.54 \pm 0.06. \tag{4.18}$$

This behavior is not obvious, but it is interesting, since ΔP_{ss} now can be calculated from the tuning parameter Q_w. An exponent $\beta \neq 1$ is consistent with the findings of Knudsen *et al.* [24] for steady-state simulations with $M = 1$.

4.4   Compressibility of air and flowrates

The compressibility of air increase the complexity of the system further. Here we try to explain and account for some of the effects.

Our model is only open to atmospheric pressure through the outlet reservoir. The reservoir mass of wetting fluid is measured continuously during an experiment. Through the fluid density, the produced output volume of wetting fluid V_{out} is calculated. Provided that the pore space inside the matrix is constant, it follows from mass conservation that the volumetric flow-rate of incompressible fluids is equal at the inlet and outlet. With eight syringes used for the wetting fluid and fifteen in total, an equal and constant pumping rate for every syringe gives,

$$Q_w = 8Q_0 = \frac{dV_{\text{out},8}}{dt} \tag{4.19}$$

$$Q_{15} = 15Q_0 = \frac{dV_{\text{out},15}}{dt}, \tag{4.20}$$

where Q_0 is the constant flow-rate of a single syringe. The wetting fluid flow-rate used in the experiments Q_w, corresponds to the time derivative of the output volume $V_{out,8}$ when eight syringes are used under single phase incompressible flow. When all fifteen syringes are used the flow-rate Q_{15} is found accordingly.

In our model we use seven air filled syringes, all displaced at the same constant speed as the glycerol/water syringes. Figure 4.20 shows the produced output volume V_{out} as a function of time t for all experiments. There is an initial transient, resulting from the jump start of the experiments, as described in section 3.5.1. After this transient, during the invasion phase, the volume increases linearly with the slope Q_{tot}^{inv}. Some time after breakthrough there is a crossover and the volume starts to increases linearly with the slope Q_{ss}. The subscript $_{ss}$ indicates that we are in the steady state regime. The crossover at breakthrough is obvious since we measure wetting fluid mass. When both air and fluid are produced at the outlet, the mass increase pr. unit time will decrease. Also indicated in figure 4.20 is the slope in the incompressible limit, $15Q_0$.

There are several things to notice about the graphs in figure 4.20. The difference between the
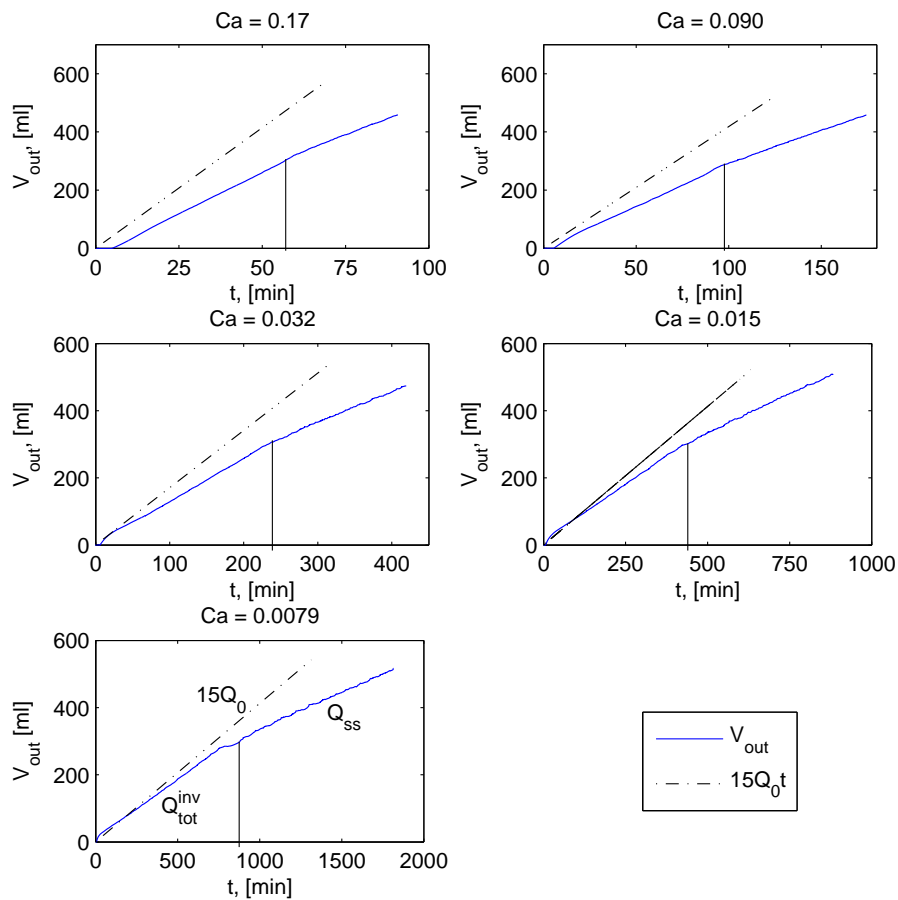
Figure 4.20: *Produced output volume V_{out} of the wetting fluid as a function of time t. Wetting fluid mass is the measured quantity, and so $V_{out} = m_{out}/\rho_w$. For each experiment, the expected output volume for incompressible fluids $15Q_0t$ is also plotted (dash dotted line). After the initial transient, the volume increases with a slope Q_{tot}^{inv}. When steady-state is reached, air is also produced at the outlet and a crossover is observed with a slope Q_{ss}. The crossovers are indicated by the vertical lines.*

Ca	Q_w [ml/min]	Q_{nw}^{inv} [ml/min]	Q_{ss} [ml/min]	Q_{tot}^{inv} [ml/min]	$15Q_0$ [ml/min]
0.0079	0.22	0.13	0.22	0.35	0.41
0.015	0.44	0.23	0.44	0.67	0.83
0.032	0.91	0.38	0.91	1.29	1.71
0.090	2.23	0.66	2.18	2.90	4.18
0.17	4.42	1.30	4.36	5.73	8.29

Table 4.4: *In columns from left to right: Capillary number Ca, wetting fluid flow-rate Q_w, invading non-wetting fluid flow-rate Q_{nw}^{inv}, wetting fluid steady-state flow-rate Q_{ss}, total invasion flow-rate Q_{tot}^{inv}, incompressible limit flow-rate from all syringes $15Q_0$. The difference between Q_w and Q_{ss} for the Ca = 0.090 and Ca = 0.17 experiment, is within the limits of uncertainty.*

slopes Q_{tot}^{inv} and $15Q_0$ is direct evidence of compressibility. A difference is to be expected due to the high pressure differences, but it is not obvious that the slope Q_{tot}^{inv} is constant. Since the wetting fluid flows continuously through the model, it follows that its contribution to the total flow rate is Q_w. For all experiments performed, we find that during the invasion phase:

$$Q_{tot}^{inv} = Q_w + Q_{nw}^{inv}. \tag{4.21}$$

It follows from eq. 4.21 that the amount of produced output volume pr unit time due to injection of compressed air Q_{nw}^{inv} is constant. That is, constant on average since bursts contributes to fluctuations on smaller timescales. When steady-state is reached we would expect,

$$Q_w = Q_{ss}. \tag{4.22}$$

Eq. 4.22 states that the pre-selected wetting fluid flow-rate should equal the measured slope of V_{out} during steady-state. Table 4.4 shows characteristic flow-rates for all experiments. Q_w and $15Q_0$ have been calculated from eq. 4.19-4.20 during single phase flow of the water/glycerol mixture. Q_{tot}^{inv} and Q_{ss} are found from the slopes of figure 4.20. The values of Q_{nw}^{inv} are then found from eq. 4.21. Table 4.4 shows that Q_w and Q_{ss} are in good agreement with eq. 4.22.

So why is the compressed flow-rate of air during invasion constant? We believe it is because of two reasons, 1) the air pressure increases almost linearly during invasion (see figure 4.14), and 2) expansion of independent air-clusters and bursts only contribute to the displacement of glycerol/water fluid by a small amount. In this case air will only produce output volume of fluid as long as it is connected to the inlet node. To test the last statement, we set out to estimate Q_{nw}^{inv} from the air-pressure curves of figure 4.14 and the corresponding change in volume of air in a syringe. The ideal gas law is given by

$$PV = NkT, \tag{4.23}$$

where P is pressure, V volume, N the number of molecules, k the Boltzmann's constant and T temperature. If we assume T and N to be constant, it follows that,

$$\frac{dP}{dV} = -\frac{NkT}{V^2} \tag{4.24}$$

$$VdP = -NkT\frac{dV}{V} \tag{4.25}$$

$$NkT\frac{dP}{P} = -NkT\frac{dV}{V} \tag{4.26}$$

$$\frac{dP}{P} = -\frac{dV}{V}. \tag{4.27}$$

Eq. 4.27 states that the relative pressure change equals the negative relative volume change. Figure 4.21 shows a highly simplified version of a syringe and tube, filled with air and connected

to the inlet of the porous matrix. The syringe piston is displaced at a constant speed v_s by the syringe pump. The spring represents the presence of wetting fluid. We imagine at some time that the volume of air in the syringe/tube system is V_0. At this time the wetting fluid has completely clogged the region in front of the inlet node. Some time later the total air volume is given by $V_1 + \delta V$, where δV is the amount of wetting fluid displaced by the compressed air. During
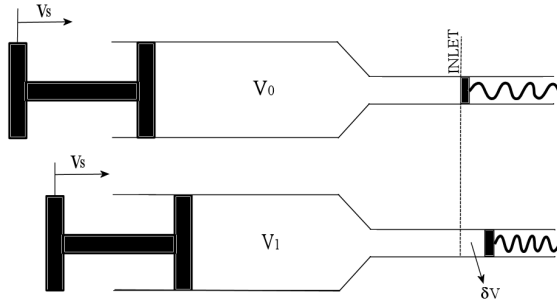

Figure 4.21: *Syringe and tube filled with air connected to the inlet. The syringe piston is displaced at the same constant speed v_s at all times. The presence of wetting fluid is indicated by the spring. At some time the air volume is given by V_0. Some time later the air volume is given by $V_1 + \delta V$, where δV is the amount of air volume that has entered the porous matrix.*

an experiment the remaining volume of air in the syringe/tube system is known at all times. We want to apply eq. 4.27 to calculate the volume δV of displaced wetting fluid during a time interval δt. However, for eq. 4.27 to apply the number of air molecules N must be conserved. This means that the time interval δt must be small enough so that the invading air cluster is not snapped off from the inlet. On the other hand, δt must be large enough so that the corresponding difference in air pressure is not affected by fluctuations. This was solved by making a linear fit to the air-pressure curves of figure 4.14, that reflected the overall pressure increase. Using eq. 4.27 we get,

$$\frac{V_0 - (V_1 + \delta V)}{V_0} = -\frac{P_0 - P_1}{P_0} \tag{4.28}$$

$$\delta V = \left(1 - \frac{P_1 - P_0}{P_0}\right) V_0 - V_1, \tag{4.29}$$

where $P_0(t_0)$ and $P_1(t_1)$ are the difference in air pressure in the time interval $\delta t = t_1 - t_0$, found from measurements. The air volume in the syringe/tube system, $V_0(t_0)$ and $V_1(t_1)$ is found from the syringe pumping rate, and the initial volume at the start of the experiment,

$$V_{\text{init}} = V_{\text{syringe}} + V_{\text{tube}} \tag{4.30}$$

$$V_{\text{init}} = 60.0 \text{ ml} + 12.7 \text{ ml} = 72.7 \text{ ml}. \tag{4.31}$$

$$V_i(t_i) = V_{\text{init}} - Q_0 t_i. \tag{4.32}$$

The compressed flow-rate of air during invasion is then estimated by,

$$Q_{nw}^* \approx 7 \frac{\delta V}{\delta t}. \tag{4.33}$$

The factor 7 enters because seven syringes of air are used in the experiments. The estimates are summarized in table 4.5. By comparison with Q_{nw}^{inv} it is apparent that the estimates are quite good,

Q_{nw}^{inv} [ml/min]	0.13	0.23	0.38	0.66	1.30
Q_{nw}^* [ml/min]	0.13	0.25	0.45	0.78	1.55

Table 4.5: *Comparison of estimated values Q_{nw}^* of the compressed air flow-rate during invasion, with the measured values Q_{nw}^{inv}.*

though there are some deviations for the fast experiments.

During steady-state the air pressure fluctuates around a constant value. At this time, the air is compressed enough to enter the porous matrix at the same flow-rate as the wetting fluid. Measured at the inlet, the flow-rate of air would be $Q_{nw} = 7Q_0$. The air is however decompressed as it passes through the model. Steady-state conditions demand that the amount of air-mass that enters the model pr. unit time equals the amount of air-mass that leaves the model pr.unit time. Thus, the flow-rate of air must increase towards the outlet. This is difficult to observe during normal displacement, but it is easily seen during bursts.

So at steady-state the volumetric flow-rate of fluid is constant, while the flow-rate of air varies across the model, lowest at the inlet, highest at the outlet. During steady-state we define the total flow-rate as,

$$Q_{\text{tot}} = Q_w + Q_{nw} = 15Q_0, \tag{4.34}$$

where Q_{nw} is the flow-rate of air as it enters the model during steady-state.

4.5 Saturation

As we recall from section 2.5.4 the saturation of the phases are important parameters that affect the flow structure. In an experimental situation it is not an easy task to obtain values of saturation with a high degree of accuracy. The wetting and non-wetting saturation are only measured indirectly in our experiments, and must be found either from image analysis or from the measured output volume. In this section we study how local saturation depends on position and time, before we turn to a discussion of how the global saturation during steady-state changes between experiments.

In a porous medium with a pore-space volume $V_{ps} = \phi LA$, the wetting and non wetting saturation are given by,

$$S_w = \frac{V_w}{V_{ps}}, \quad S_{nw} = \frac{V_{nw}}{V_{ps}} \tag{4.35}$$

$$S_w + S_{nw} = 1 \tag{4.36}$$

where V_w and V_{nw} are the volumes of wetting and non-wetting fluid respectively.

4.5.1 Position and time dependence

To see how non-wetting saturation depends on space and time, image analysis is used. The region of the porous matrix under consideration is indicated in the lower right image of figure 4.2. The position dependence is studied in the direction of flow, by summing up grayscale intensity values in small boxes as shown in figure 4.22. The average intensity in these boxes will reflect the local saturation. Recall from section 3.3 that grayscale intensities are integers in the range $[0, 255]$. Within each box, glass beads and one of the fluids are always present, whereas the other fluid may be present. Thus, glass beads and air will give the highest intensity value, glass beads and glycerol/water the lowest and glass beads plus both phases an intermediate value. The method of using grayscale intensities from raw images is preferred over thresholded black and white images, due to accuracy. The drawback with this method is that S_w and S_{nw} cannot be found without proper calibration. That is, to determine the functions,

$$S_{nw} = S_{nw}(I), \quad S_w = 1 - S_{nw}(I), \tag{4.37}$$

where I is the intensity. However, our purpose at this point is mainly to investigate how the saturation *changes* with respect to position and time.

To get reliable results, the effect of a varying background intensity must be accounted for. As explained in section 3.2 we put much time into reducing this effect, but a small intensity gradient,
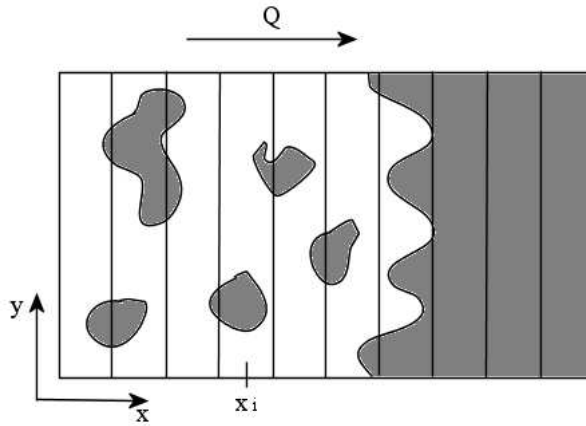
Figure 4.22: *Schematic illustration of the bound region in figure 4.2. The direction of flow is indicated. Image intensity as a function of position x_i is found by summing up the image grayscale values within each box. The box size in x-direction is set to 1 cm, and each box contains roughly 3150 pores.*

constant in time, is still present. We propose the following method to improve accuracy: assume that the intensity I in the box at position x_i at time t can be written,

$$I(x_i, t) = \zeta(x_i) \left(C_b + c_w S_w^{\text{loc}}(x_i, t) + c_{nw} S_{nw}^{\text{loc}}(x_i, t) \right), \tag{4.38}$$

where $\zeta(x_i)$ is a position dependent factor due to a varying background illumination. C_b is the intensity contribution of the glass beads. We expect this to be a constant, if the boxes are large enough to contain roughly the same number of glass beads. $S_w^{\text{loc}}(x_i, t)$ is the local wetting saturation in the box at position x_i at time t. c_w is a constant so that the product $c_w S_w^{\text{loc}}(x_i, t)$ gives the intensity contribution of the wetting fluid. The contribution of the non-wetting fluid is defined similarly. In order to use eq. 4.38 as a measure of the saturation, it is clear that only S_w^{loc} and S_{nw}^{loc} can depend on position and time. This is solved by including the intensity I_0 of a *background image* in the calculations. This background is just an image of the porous matrix saturated with the wetting fluid. For the background image, $S_w^{\text{loc}}(x_i, t) = 1$, and the intensity becomes,

$$I_0(x_i, t) = \zeta(x_i) \left(C_b + c_w \right). \tag{4.39}$$

To avoid the effect of the background gradient, we use the following equation,

$$I'(x_i, t) = \frac{I - I_0}{I_0} = \frac{1}{C_b + c_w} \left(C_b + c_w S_w^{\text{loc}}(x_i, t) + c_{nw} S_{nw}^{\text{loc}}(x_i, t) - C_b - c_w \right) \tag{4.40}$$

$$= \frac{1}{C_b + c_w} \left(c_w (1 - S_{nw}^{\text{loc}}(x_i, t)) + c_{nw} S_{nw}^{\text{loc}}(x_i, t) - c_w \right) \tag{4.41}$$

$$= \frac{c_{nw} - c_w}{C_b + c_w} S_{nw}^{\text{loc}}(x_i, t) \tag{4.42}$$

$$I'(x_i, t) \propto S_{nw}^{\text{loc}}(x_i, t). \tag{4.43}$$

The Matlab script used to find the intensity in eq. 4.43 is included in appendix B.2. Figure 4.23 shows the intensity I' of each box in position x_i at time t for all experiments. The interval of t ranges from when the front reaches the imaged region shown in figure 4.2, to some time out in the steady-state regime. Initially the non-wetting saturation is zero because the imaged region saturated with wetting fluid. As the invasion front passes by, the saturation in boxes of larger and larger values of x will reach a plateau value. Finally, when the front has left the imaged region, a plateau saturation is observed for all values of x. Several things should be noted about this figure. For the three lowest Ca-numbers, the non-wetting saturation in the homogenous region of the invasion structure, reaches a plateau value very close to that of later steady-state. This happens way before the invasion structure leaves the imaged region, and thus long before steady-state time t_{ss}. For the two highest Ca-numbers, the non-wetting saturation of the homogenous region,

reaches a maximum during the invasion phase. When the front leaves the imaged region and steady-state is reached, the saturation slowly decreases to the later steady-state value. Note also the dip in the plateau of the Ca $=$ 0.17 and Ca $=$ 0.090 experiment for low x-values during steady-state. As of yet, we cannot explain this behavior. Since this is the region closest to the inlet (about 10 cm), it may be that the boundary conditions are somehow responsible for the dip in non-wetting saturation.

The behavior of the saturation discussed above is interesting, because if the saturation of the mixed region during invasion can be measured, one has a very good estimate of the later steady-state saturation. Conversely, the steady-state saturation can be used to estimate that of the mixed region during invasion.

When it comes to position dependence, the non-wetting saturation in the homogenous region during invasion fluctuates around a constant value. This is also found during steady-state. However, it is apparent from figure 4.23 that the fluctuations increase with the capillary number. We do not find an average increase in the non-wetting saturation with increasing x. Thus, we conclude that the expansion of air through the model does not cause a larger air volume towards the outlet.

4.5.2 Steady-state, global saturation

We now turn to a description of how the global wetting saturation S_w is calculated from the produced output volume of fluid, shown in figure 4.20. The principle behind these calculations are simple. Initially, the porous matrix is saturated with wetting fluid,

$$S_w = \frac{V_w}{V_{ps}} = 1, \tag{4.44}$$

where V_w is the volume of wetting fluid inside the porous matrix and V_{ps} the pore-space volume. If the volume of wetting fluid that goes into and out of the porous matrix is known at all times, the difference $\Delta V_{O,I}$ can be used to find the saturation. Using eq. 4.44 we get,

$$S_w(t) = \frac{V_{ps} - \Delta V_{O,I}}{V_{ps}} \tag{4.45}$$

$$= \frac{V_{ps} - (V_{\text{out}}(t) - V_{\text{in}}(t))}{V_{ps}} \tag{4.46}$$

$$= 1 - \underbrace{\frac{V_{\text{out}}(t) - V_{\text{in}}(t)}{V_{ps}}}_{S_{nw}}, \tag{4.47}$$

where V_{in} is the injected fluid volume and V_{out} is the produced output volume. When air enters the porous matrix, more fluid volume goes out than in, and V_w must decrease. However, there are some experimental difficulties in the procedure of finding $V_w(t)$. V_{out} is measured directly, whereas V_{in} is given as,

$$V_{\text{in}}(t) = 8Q_0(t) + V_0, \quad \text{for} \quad t \geq t_0, \tag{4.48}$$

where Q_0 is the flow-rate from one syringe and t_0 is the time at which air enters the porous matrix. The meaning of V_0 will be explained shortly. The reason for the restriction $t \geq t_0$ is due to the initial volume of fluid in the air tubes, as explained in section 3.5.1. When the syringe pump is started, the air tubes are closed off from the porous matrix. This causes air pressure to increase, and prevents backflow. However, when the three-way vents are opened, wetting fluid will enter the matrix from all fifteen inlet nodes. We have no control over the flow-rate of wetting fluid from the air tubes during this time. The only contribution from the seven air tubes to $V_{\text{in}}(t)$ is the initial volume V_0 of wetting fluid. If air enter the porous matrix from all inlet nodes at the
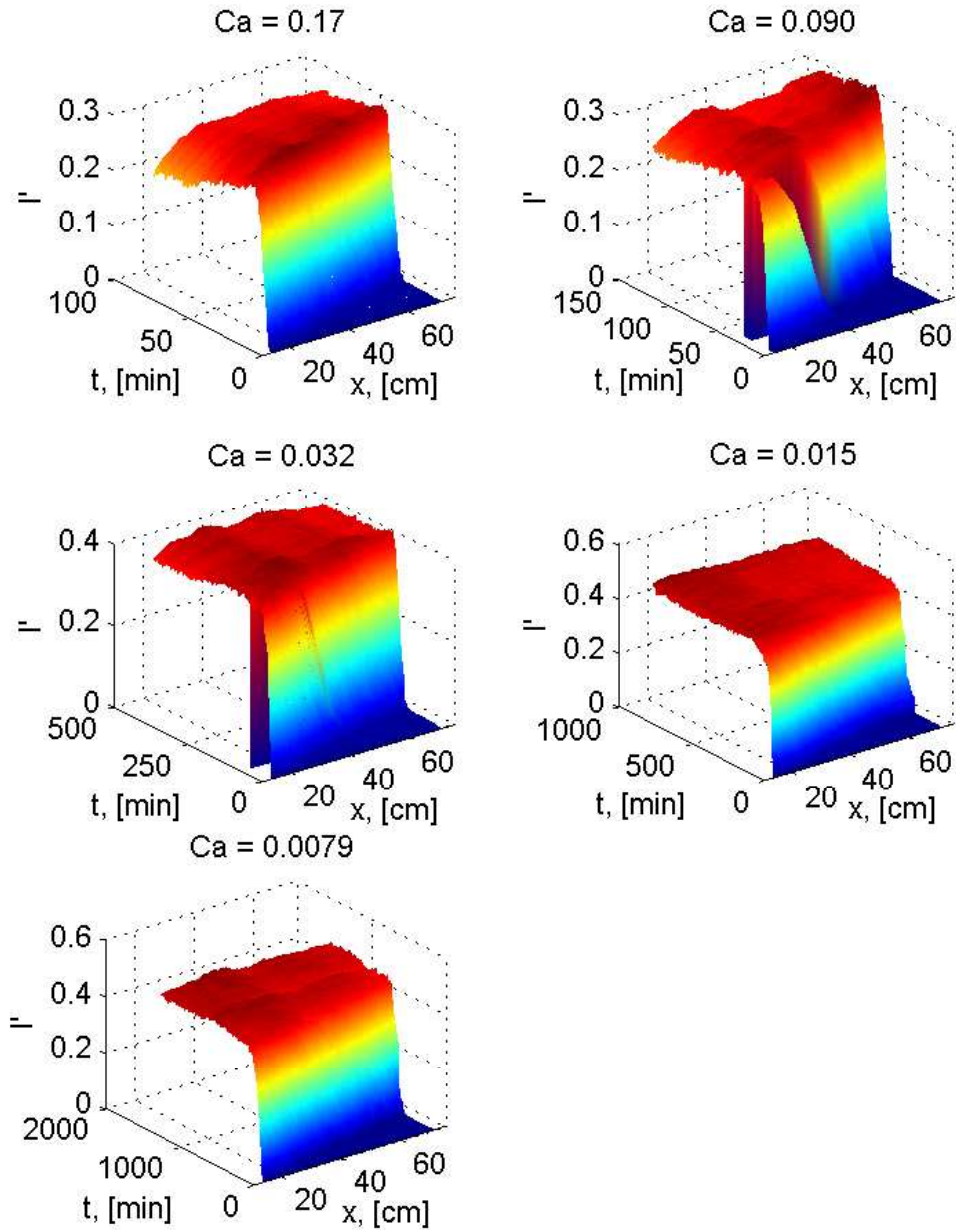
Figure 4.23: *Intensity $I' \propto S_{nw}^{loc}(x_i, t)$ as a function of time t and position x in the direction of flow. Five different experiments are shown. The surfaces have been smoothed to make the global behavior more transparent. The gap seen in the Ca = 0.090 and Ca = 0.032 experiment is due to removal of images not suitable for analysis.*

same time, V_0 is found from the produced output volume,

$$V_0 = V_{\text{out}}(t_0) - 8Q_0 t_0. \tag{4.49}$$

The assumption that air enters the porous matrix at the same time from all nodes, gives rise to the largest source of error in these calculations. We have defined t_0 as the time at which air is observed to enter the model from all seven inlet nodes. On average, this happens about 1.5 min after air is seen to enter from the first inlet node[6]. This means that V_0 and hence $S_w(t)$ will be overestimated. Fortunately the saturation can be estimated also from image analysis. It is our hope that the use of independent methods will reveal information of the whereabouts of S_w and S_{nw}. Figure 4.24 shows the calculated saturation of wetting fluid as a function of time
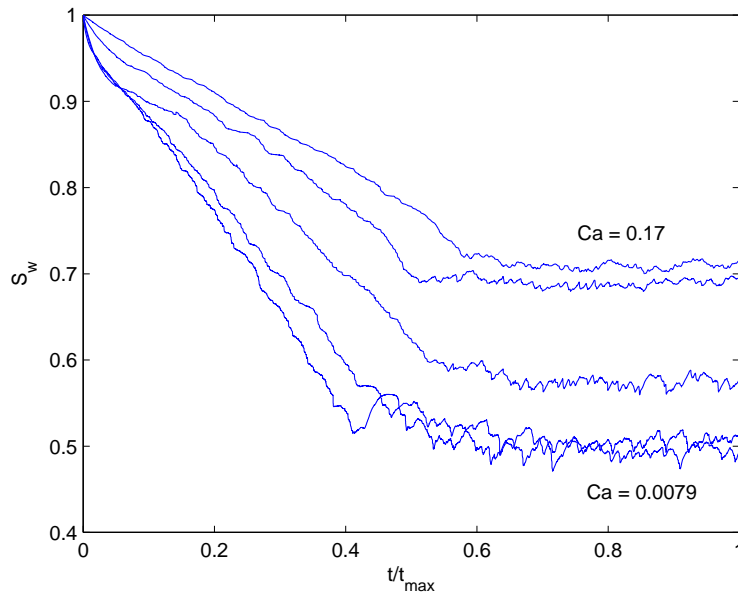

Figure 4.24: *Saturation of wetting fluid S_w calculated from eq. 4.47. To get a reasonable view for all Ca-numbers, the time t is normalized by the duration time of each experiment, t_{max}. Consistent with observations, S_w decreases with the Ca-number.*

for all Ca-numbers. The behavior is consistent with observations. First of all there is a region in the saturation curves, for all experiments, where S_w decreases almost linearly. This is to be expected since Q_w and Q_{nw}^{inv} are constant during the invasion phase. When steady-state is reached saturation stabilizes and fluctuates around a mean value. The highest saturation of wetting fluid is found in the fastest experiment and a decrease is observed with decreasing Ca-numbers. This was also observed visually during experiments. Note that the steady-state saturations of the two highest and two lowest Ca-numbers are quite close. In fact, it is hard to separate the Ca = 0.0079 and Ca = 0.015 cases. We believe that the saturation is different in these two experiments, but it may be only by a small amount.

In section 4.5.1 the image intensity $I'(x_i, t)$ was introduced and from eq. 4.43 it is seen that the intensity is proportional to $S_{nw}^{loc}(x_i, t)$. To see how the global saturation changes with time, we apply eq. 4.43, not in a small box, but for the whole imaged region of the porous matrix. Even though the proportionality factor between I' and S_{nw} is unknown, we believe this to be the most accurate method to determine the functional form of saturation with respect to flow-rate. Figure 4.25 a) shows the non-wetting fluid saturation S_{nw} calculated from eq. 4.47 and the intensity $I' \propto S_{nw}$. It is interesting to note that the plateaus of I' has the same behavior as the saturation calculated from measurements. We see that the saturations of the Ca = 0.0079 and Ca = 0.015

---

[6]We have tried to minimize this effect as much as possible, by ensuring that all tubes connected to air filled syringes are of equal lengths and diameters. A difference in tube volume will cause a different initial pressure, and hence the volume of wetting fluid in each air tube will be displaced at a different rate.
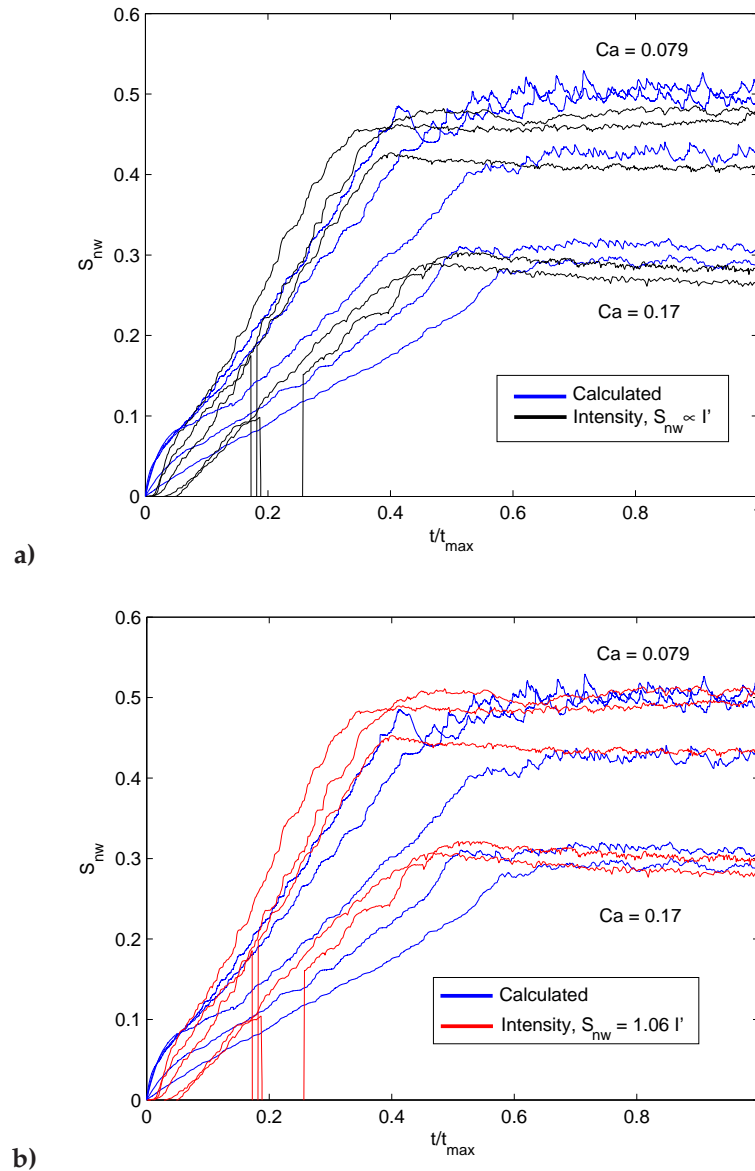
Figure 4.25: *Non-wetting fluid saturation S_{nw} for all Ca-numbers. To get a reasonable view of all curves, the time t is normalized by the duration time of each experiment, t_{max}. In each figure, two sets of curves are shown. One set of saturation curves (blue) has been calculated (eq. 4.47) from the measured output volume, and the other set is intensity (red/black) curves $S_{nw} \propto I'$ found from eq. 4.43, through image analysis. The sudden drop in some of the intensity curves has no physical meaning, it is simply due to the removal of images unsuitable for analysis. **a)** The difference in plateau values in both sets of curves displays the same behavior. **b)** For $S_{nw} = 1.06 I'$, the plateaus of both sets of curves are consistent.*

experiment are in fact separated by a small amount. We conclude the following from this figure. The difference in saturation values between experiments, calculated from the measured output volume, are consistent with the behavior of the image intensity I'. This indicates that the relative change in saturation between each Ca- number is in the vicinity of the real value. In figure 4.25 b) we have tried to find the proportionality constant of eq. 4.43, based on the calculated values of non-wetting fluid saturation. For a factor 1.06 the plateaus of the two sets of curves are more or less consistent.
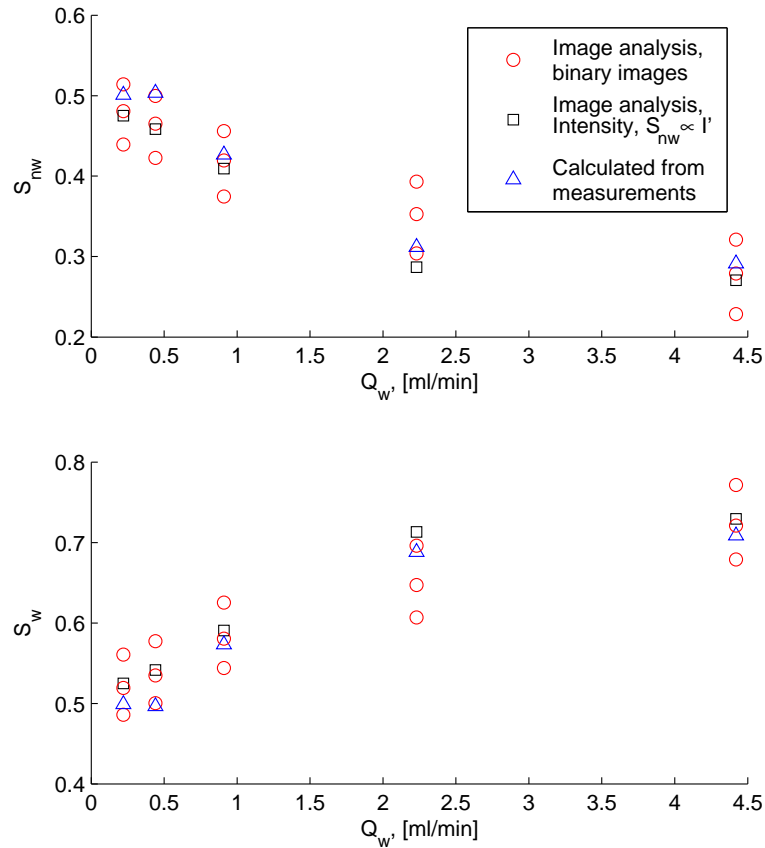
Figure 4.26: *Steady-state, non-wetting S_{nw} and wetting S_w saturation as a function of flow-rate Q_w. Three methods have been applied to find the global saturation: Calculation from measurements (eq. 4.47), analysis of the raw image intensity I' (eq. 4.43) and analysis of binary images (eq. 4.50). It is evident that the saturations found from binary images depends highly on the threshold. However all methods predict the same behavior.*

There is also a second method of image analysis that can be applied to find an estimate of the actual saturation. Instead of using the grayscale images to find the intensity, they can be thresholded and converted to binary images. The saturations are then estimated as,

$$S_w \approx \frac{N_w}{N_{\text{tot}}\phi} \tag{4.50}$$

$$S_{nw} \approx \frac{N_{nw}}{N_{\text{tot}}\phi}, \tag{4.51}$$

where ϕ is the porosity and N_{tot} is the total number of pixels in an image. N_w and N_{nw} is the number of wetting and non-wetting pixels respectively. Since the glass beads will be counted as non-wetting pixels after thresholding, it is common to find S_w from the analysis, and from this value obtain S_{nw} from eq. 4.36. In our experiments, all results obtained through image analysis will depend on the selected threshold value as discussed in section 3.3.2. Due to the large amount of interfaces only a small change in threshold value may change the resulting binary image. There simply is no "correct" value to be found. However, through visual inspection we have been able to identify an interval in which the threshold value must be set. Outside this interval, the binary image does not represent the original raw image very well.

To calculate the saturation in steady-state from eq. 4.50, three threshold values were chosen, $(121, 130, 140)$. The Matlab script used is found in appendix B.2. For each threshold value the time averaged saturation over 100 steady-state images was found. This is shown in figure 4.26, together with time averaged steady-state saturations found from measurements (eq. 4.47) and the raw image intensity (eq. 4.43). We emphasize again that the intensity is only proportional to the non-wetting saturation. The saturations are plotted as functions of Q_w. Note that the flow-rate of air Q_{nw}, is dependent on Q_w through eq. 4.34. An increase in Q_w means an increase also of Q_{nw}. If we consider the non-wetting fluid saturation in figure 4.26, it decreases in the range $(0.5, 0.3)$ with increasing flow-rate. It is not surprising that the saturation between the two slowest experiments only differ by a small amount, since the flow-rates are quite close. It is more interesting that the saturation only shows a small decrease between the two fastest experiments. For a non-zero flow-rate of non-wetting fluid, S_{nw} can never become zero, hence a lower limit is reached. It may be the contours of this lower limit that is observed for the two fastest experiments.

In the range of S_{nw} explored, we did not observe any dramatic change in the displacement structure. During steady-state there was a homogenous mixing of both phases. When the flow-rate was tuned, the size of the non-wetting clusters changed, but the largest cluster in all experiments was always much smaller than the system size. As discussed in section 2.5.4 Ramstad *et al.* [8] found that above a critical non-wetting saturation $S_c \sim 0.69$, the largest non-wetting cluster percolated the system during steady-state. Note that in all our experiments $S_{nw} < S_c$. The pair of fluids used by Ramstad *et al.* had equal viscosities and were incompressible. We are very far from a viscosity match, and air cannot be considered incompressible; nevertheless it would be interesting to tune the flow-rates in such a way that higher values of S_{nw} could be explored.

4.6   Cluster analysis

We have previously discussed that the dynamics are characterized by transportation of small and fragmented non-wetting clusters of air. In this section we study how different properties of these clusters are distributed in the porous matrix. Cluster distributions in steady-state have been the main topic, but some analysis have been performed also during invasion. The difficulties of thresholding do give rise to some uncertainty, but make no mistake, there are highly interesting results in this section.

4.6.1   Computational method

All image statistics are collected from binary images. The importance of thresholding was briefly reviewed in the previous section, and have been thoroughly discussed in section 3.3.2. To get reliable results, it is essential to study how the statistical properties are affected by choosing different threshold values. Particularly we study the size of non-wetting clusters. Throughout this chapter, the cluster size s will be measured in number-of-pixels where,

$$[s] = \# \text{ pixels} \tag{4.52}$$

$$1 \text{ pixel} = 0.037 \text{ mm}^2. \tag{4.53}$$

We also need to introduce the threshold value, an integer in the grayscale range,

$$\text{threshold value} = \chi \in [0, 255]. \tag{4.54}$$

The lower cutoff-size $s_{\min}$ in our system is the bead size. On average, 25 pixels are needed to cover a glass bead, hence

$$s_{\min} = 25. \tag{4.55}$$

Non-wetting fluid clusters of size $s \leq s_{\min}$ cannot be distinguished from beads, and so we have no information of how clusters are distributed at this length scale. After the raw image is thresholded, a routine found in Appendix B.1 is used to remove both clusters $s \leq s_{\min}$ and all clusters at the boundary in the region of interest. Boundary clusters are removed, because we have no information of their actual size. The region of interest is a cropped part of the full image, as shown bottom right in figure 4.2. The method of logarithmic binning is used to obtain the histogram of the remaining cluster sizes. From this histogram, the probability distribution $P(s)$ is found, as explained in appendix A. The probability to draw a cluster of size s is then given as $P(s)ds$. During steady-state, the reorganization of clusters are statistically invariant. Since we also study a large system, the statistics are very good.

For a selected value of χ, it possible by visual inspection to see how the binary image reflects the connectivity of clusters in the raw image. On this basis we have found that,

$$190 \leq \chi \leq 210. \tag{4.56}$$

Figure 4.27 shows the χ dependence of $P(s)$ for all Ca-numbers during steady-state. As argued in section 3.3.2, images from all experiments are thresholded at the same value. We will not discuss the physical meaning of $P(s)$ in figure 4.27 at this point; we in this case only interested in the effects of varying χ. This effect is more or less the same for all Ca-numbers. For the lowest threshold value, $\chi = 190$, we find the highest[7] probability of medium and large clusters, consequently the lowest probability[8] for the smallest clusters. This is reasonable, since $\chi = 190$ gives the highest number of grayscale intensity values that will be counted as white (set equal to one in a binary image), and hence the cluster connectivity is at a maximum. As the threshold is tuned towards the upper limit of eq. 4.56, we see a systematical change of $P(s)$ for all Ca-numbers. At $\chi = 210$, the probabilities of the smallest clusters have the highest values, and due to normalization the medium and largest clusters have the lowest values. The most critical effect of tuning χ, is the corresponding difference in the size of the largest clusters. These clusters are associated with a characteristic length scale in our system, and should obviously not depend on χ. However, the cluster distribution does not change its shape drastically when tuning χ in the interval of eq. 4.56, and it seems that P(s) is offset by an equal amount for each Ca-number. Based on thorough visual inspection, we have chosen to use $\chi = 205$, in the following analysis.

---

[7] By highest we mean, with respect to the P(s) curves of other values of χ.
[8] The probability change of the smallest clusters are not easily seen in the log-log plots of figure 4.27.
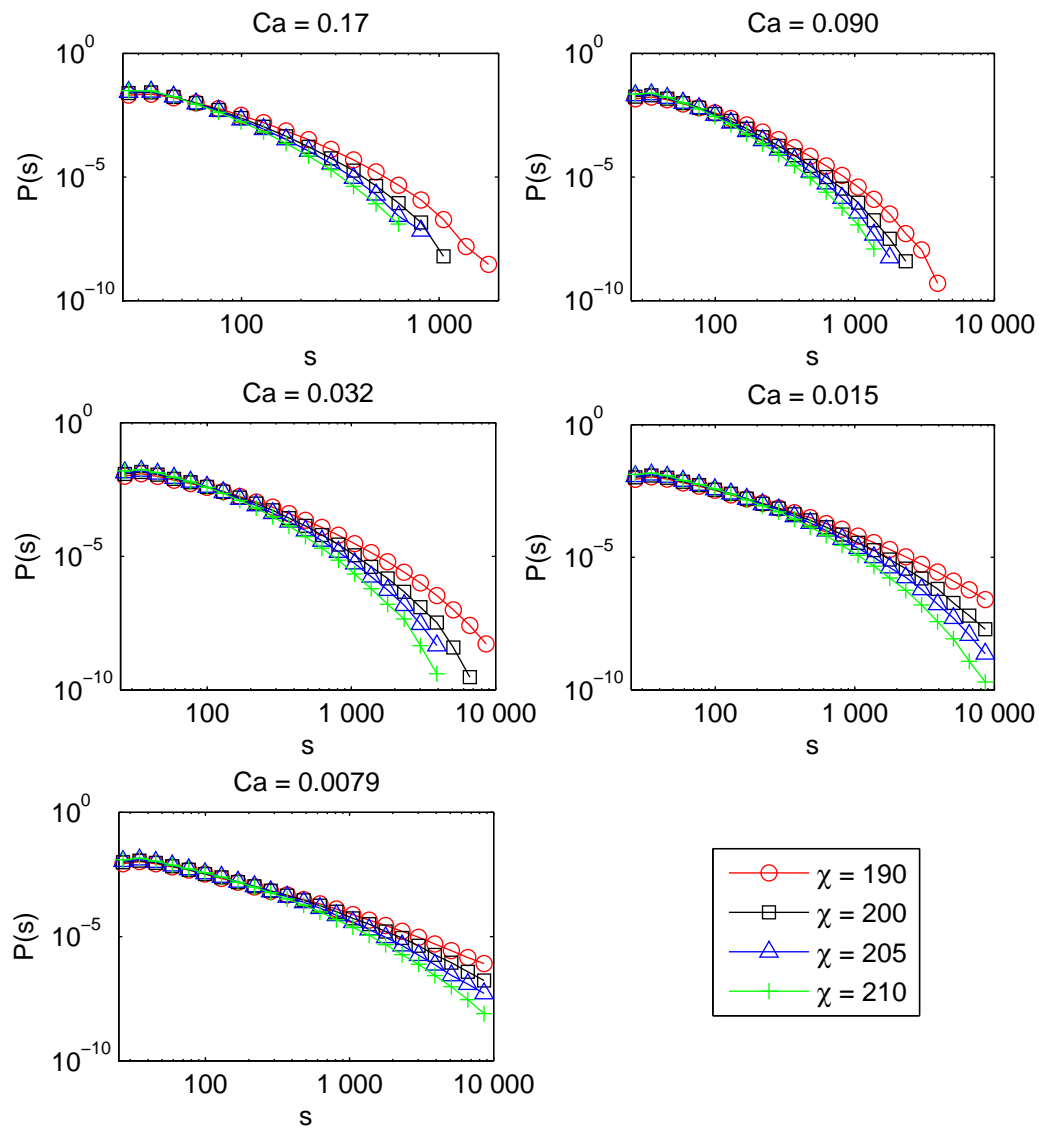
Figure 4.27: *Probability distributions $P(s)$ for all experiments. For each Ca-number, $P(s)$ is computed for four different threshold values of χ. The size of the largest clusters are seen to decrease with increasing χ. Based on visual inspection of the binary images, we believe the best threshold value within the interval to be $\chi = 205$.*
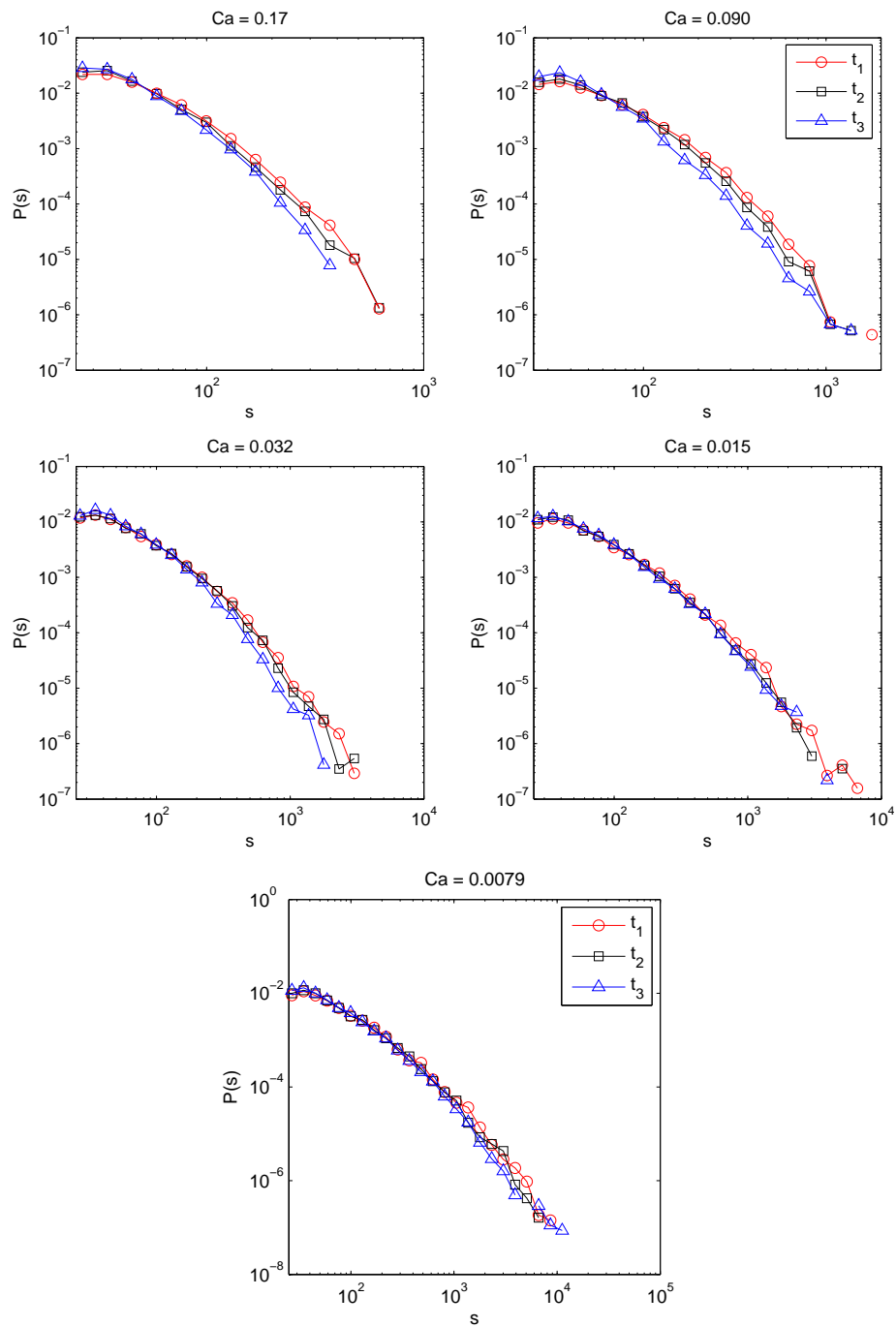
Figure 4.28: *Probability distribution of non-wetting clusters $P(s)$. For each Ca-number, the distribution is calculated from the region of interest shown in figure 4.29 in the timesteps $t_1 < t_2 < t_3$. For all experiments the behavior of $P(s)$ during steady-state (t_3) is very close to that at breakthrough (t_2) and midway invasion (t_1). A cutoff is evident in all timesteps and Ca-numbers.*

4.6.2   Cluster size distributions

We have previously discussed the similarities between the homogenous region during invasion and the global structure found in steady-state. The change in cluster sizes during this transition

will be the final contribution to this discussion. For each Ca-number the non-wetting cluster size distribution was computed in three timesteps: When the least advanced parts of the front had reached the middle pressure sensor t_1, at breakthrough t_2 and late steady-state t_3. The imaged region used in all timesteps is shown in figure 4.29, whereas the resulting probability distribu-

Figure 4.29: *The region of interest ROI, used to study the change in cluster size distribution $P(s)$ during the transition to steady-state. The middle pressure sensor is located at the bottom nozzle closest to the outlet.*

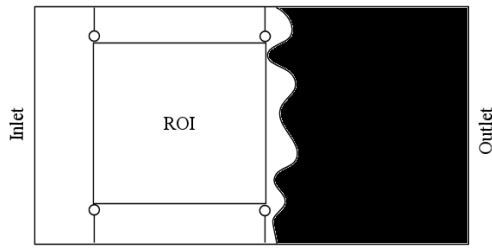tions are shown in figure 4.28. From the latter figure we see that there is a clear cutoff present for all Ca-numbers. A spanning cluster would have a typical size of $s_L \sim 10^6$. Thus, it is evident that all clusters are small compared to the system size. We will study this cutoff shortly, but first we turn to a description of the transition to steady-state. Note that for the three highest Ca-numbers in figure 4.28, the number of medium and large cluster sizes decreases with time, whereas the number of smaller clusters increase with time. We do not believe that this behavior is a statistical artifact, since it suggests that the fragmentation of non-wetting clusters increases slowly with time. Slowly, since at t_1 the distribution is already very close to that of later steady state, t_3. For the two lowest Ca-numbers the curves are almost inseparable, meaning that the reorganization of clusters are statistically invariant already midway through the invasion phase.
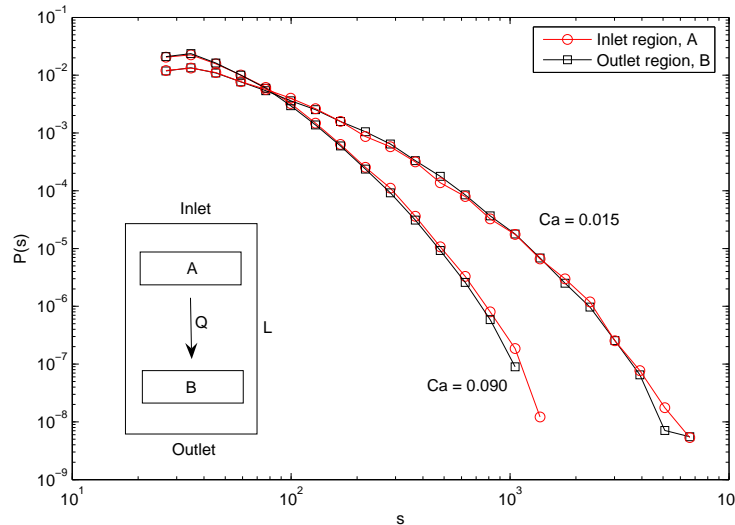
Figure 4.30: *Non-wetting cluster size distribution $P(s)$, for Ca = 0.090 and Ca = 0.015. For each Ca-number a region A close to the inlet and B close to the outlet has been considered. The width of A and B in the direction of flow is 13cm. Total length of the model is $L = 83cm$. Each distribution is a time average over 100 images during steady-state. It is evident that the clusters are distributed equally in the direction of flow. This behavior is found to apply for all Ca-numbers considered in the experiments.*

This invariance is interesting, especially when considering that the flow-rate of air during invasion is lower than in steady-state. In section 4.4 we argued that $Q_{nw}^{\text{inv}} < Q_{nw} \approx 7Q_0$. The discussion above then indicates that the statistical properties are only affected by a small amount

when the flow-rate of air increases. If so, it is reasonable to believe that the tuning parameter of the viscous background field Q_w, controls the dynamics of the system.

Relative permeabilities are usually measured under steady-state conditions and then applied to predict the behavior of transient displacements. Payatakes states in [17] that this is highly questionable. Generally this is a just statement. It is not obvious that flow parameters measured in steady-state would reflect the behavior of transient regimes. However, when it comes to our experiments in particular, we have throughout this chapter presented experimental evidence that steady-state measurements do reflect the behavior of the invasion phase. This have been shown for pressure differences, saturations and cluster size distributions.
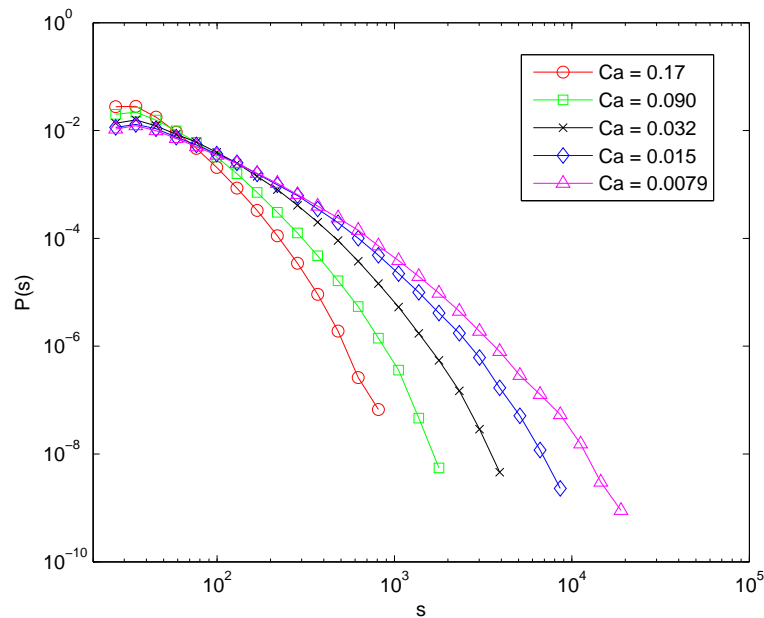

Figure 4.31: *Non-wetting cluster size distribution $P(s)$ for all Ca-numbers during steady-state. Each distribution shown is a time average of the distributions from all available images ($\sim$200 pr. experiment). A cutoff, which increases with Ca, is evident.*

We have previously discussed that the compressibility of air did not cause the saturation of non-wetting fluid to increase in the direction of flow. The question is whether this invariance is found in the statistical properties. The answer is no. Figure 4.30 shows the non-wetting cluster distributions during steady-state, from two regions in the porous matrix. Each distribution is a time average over 100 images. For the two Ca-numbers considered, it is evident that clusters are distributed equally in the direction of flow. The same behavior is also found for the remaining Ca-numbers (not shown). We conclude that the probability of finding a cluster of size s for a given Ca-number does not change in the direction of flow, which is what we would expect for two incompressible fluids.

Figure 4.31 shows the steady-state distributions of non-wetting clusters for all Ca-numbers investigated. The imaged region considered is shown bottom right in figure 4.2, and each distribution is the resulting time average from all images available. To get a good time average, the clusters in each image should be uncorrelated, as to represent different realizations. However no error is made if this is not the case. In the sets used to find the probability distributions, both correlated and uncorrelated images occurred, but it is clear from the smooth curves in figure 4.31 that the statistical basis is good. The dynamics of our system is reflected in the steady-state dis-

tributions. First of all the non-wetting clusters are small compared to the system size. For each experiment the cluster size s is found in the following range,

$$s_{\min} < s \leq s^*, \tag{4.57}$$

where $s_{\min}$ is at the size of a bead, and s^* is roughly the largest cluster in each experiment. For all experiments,

$$s^* \ll s_L, \tag{4.58}$$

where $s_L \sim 10^6$ is the size of a cluster that would span the system. The cutoffs seen in figure 4.31 dominates every distribution, and no power-law behavior is observed. This indicate that a characteristic length scale, smaller than the system size L, is present. For the lowest Ca-number, and hence the lowest flow-rate Q_w, the largest clusters are found. As the flow-rate increases, clusters decrease in size and the probability to find smaller clusters increase. This is consistent with the discussion of cluster dynamics in sections (4.2.2-4.2.1). Another interesting observation of the steady-state distributions is the existence of a crossing point for $s \approx 70$. All curves go through this point, meaning that the probability of finding a cluster at this size is independent of the flow-rate. Since all distributions are monotonically decreasing and cut off at different sizes, they must cross in order obtain normalization. However it is not obvious that every curve should cross in such a way that one is able to define a crossing point. We are not sure whether this crossing point has any physical interpretation.

In percolation theory[9], the cluster size distribution can be written,

$$P_{\mathrm{perc}}(s) \propto s^{-\tau} f(s/s_\xi), \tag{4.59}$$

where the exponent $\tau = 2.058$ for 2D percolation, and $f(s/s_\xi)$ is a cutoff function that decays faster than any power of s for $s/s_\xi \gg 1$ and is constant for $s/s_\xi \ll 1$. The cutoff cluster size s_ξ, depends on the correlation length ξ. We do not se any power-law dependence in our cluster size distributions, but the cutoff behavior is similar. An interesting feature of eq. 4.59 is that distributions for different values of s_ξ can be made to *collapse*. If the substitution $u = s/s_\xi$ is made in eq. 4.59, we get,

$$P_{\mathrm{perc}}(s) \propto s_\xi^{-\tau} u^{-\tau} f(u) \tag{4.60}$$

$$s_\xi^\tau P_{\mathrm{perc}}(s) \propto u^{-\tau} f(u) = g(u), \tag{4.61}$$

where $g(u)$ is called the *scaling function* of P_{perc}. By a collapse we mean that if $s_\xi^\tau P_{\mathrm{perc}}$ is plotted against s/s_ξ for different values of s_ξ, the curves will fall onto one single curve $g(u)$. The scaling function can then be used to predict the behavior of $P_{\mathrm{perc}}(s)$ for any s_ξ. This is very useful in general, when the probability distribution is known only numerically for a few cutoff cluster sizes. It is a common approach in physics to collapse measurements with scaling behavior. If a collapse can be found on the basis of a few data sets, one is often able to generalize and extract new information. In the discussion of section 2.5.1 we argued that due to snap-offs the length, in the direction of flow, of the largest non-wetting clusters was controlled by an upper length scale l_c (eqs. 2.74-2.76),

$$l_c = \frac{\Delta P_{D,I}}{|\nabla P_w|} \tag{4.62}$$

$$l_c = \frac{k_w^r K A}{\mu_w Q_w} \Delta P_{D,I} \tag{4.63}$$

$$l_c \propto Q_w^{-1}. \tag{4.64}$$

The above equations is based on the generalized Darcy equations, and predicts that the length of the largest clusters is inversely proportional to the wetting fluid flow-rate. From observations

---

[9]The unfamiliar reader is referred to the book by Stauffer & Aharony [47]

it seemed that clusters were in general longer in the direction of flow than in the transverse direction. As a hypothesis, we assumed that the length of the largest clusters s^*, in the transverse direction was constant, implying,

$$s^* \propto dl_c \qquad\qquad (4.65)$$

$$s^* \propto Q_w^{-1}, \qquad\qquad (4.66)$$

where d is the constant length of s^* in the direction perpendicular to the flow. Using this assumption, the cutoff cluster size s^* is also inversely proportional to the wetting fluid flow-rate. On this basis we tried to obtain a data collapse of the cluster size distributions in figure 4.31. This was not an immediate success, but the *cumulative* distribution $P(s' > s)$ of non-wetting clusters during steady-state proved useful. A treatment of cumulative distributions is given in appendix A. $P(s' > s)$ gives the probability to pick a random cluster $s' > s$, and is given by,

$$P(s' > s) = \int_s^{s^*} P(\bar{s})d\bar{s}, \qquad\qquad (4.67)$$

where $\bar{s}$ is just an integration variable. From eq. 4.67 it follows that,

$$P(s) = -\frac{dP(s' > s)}{ds}. \qquad\qquad (4.68)$$

Figure 4.32 shows the cumulative distribution of non-wetting clusters for all Ca-numbers during steady-state. They are computed in the same manner as $P(s)$. In this figure the cutoffs are even more pronounced. It was found that the re scaling, $s^*P(s' > s)$ vs. s/s^* produced a very good
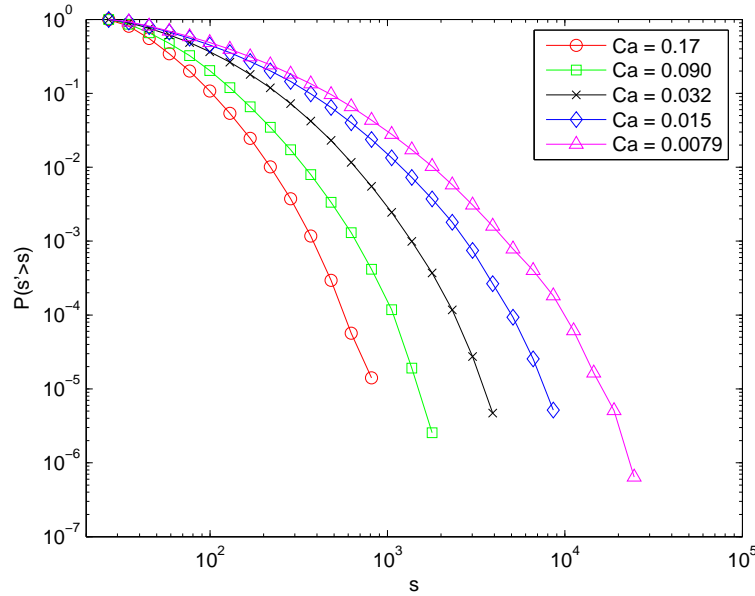
Figure 4.32: *Cumulative distribution $P(s' > s)$ for all Ca-numbers during steady-state. Each distribution shown is a time average of the distributions from all available images ($\sim$200 pr. experiment). A cutoff, which increases with Ca, is evident.*

collapse of the distributions. This is shown in figure 4.33. The general cumulative distribution function can then be written as,

$$P(s' > s) = \frac{1}{s^*}h(s/s^*), \qquad\qquad (4.69)$$
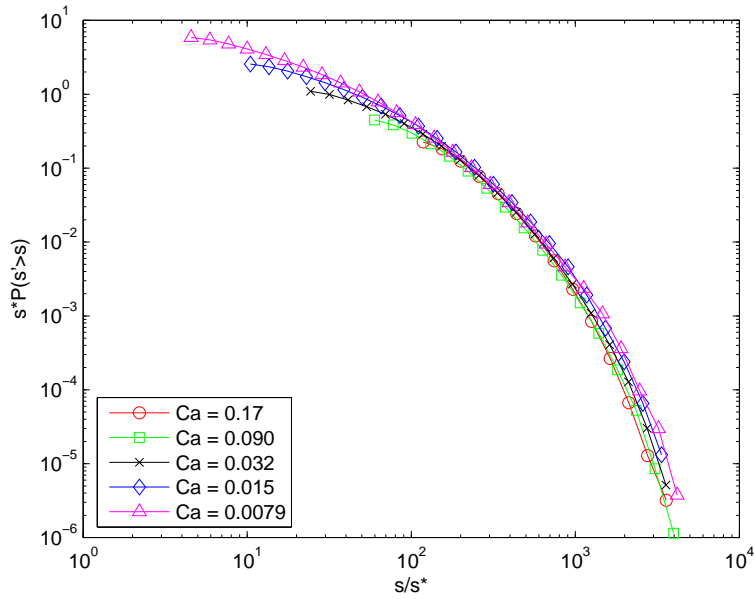
Figure 4.33: *Data collapse of the cumulative cluster distributions for all Ca-numbers. This is obtained with the re scaling $s^*P(s' > s)$ and s/s^*. The collapsed curve is the function $h(s/s^*)$ of eq. 4.69. Note that $s^* \propto Q_w^{-1}$.*
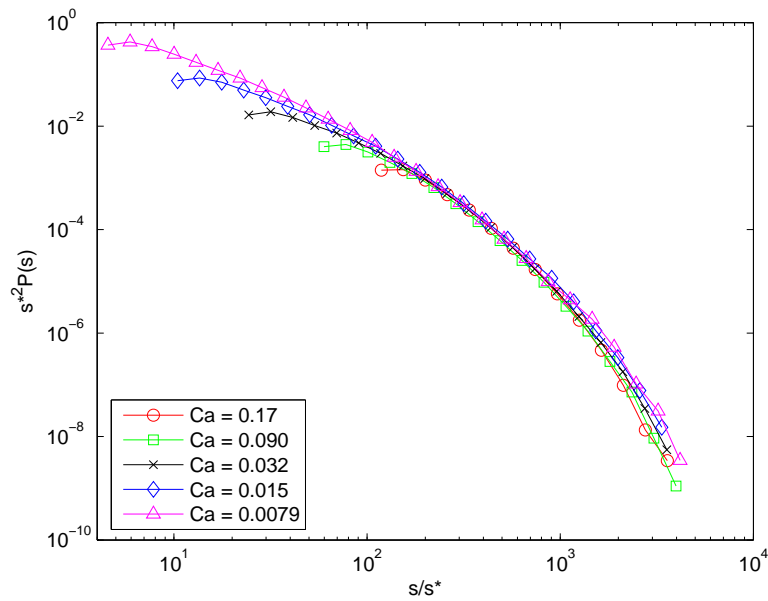
Figure 4.34: *Collapsed non-wetting cluster size distributions $s^{*2}P(s)$ vs. s/s^*, for all Ca-numbers during steady-state. The collapsed curve is the function $H(s/s^*)$ of eq. 4.72. Note that $s^* \propto Q_w^{-1}$.*

where $h(s/s^*)$ is a function which decays faster than any power of s for $s/s^* \gg 1$. Eq. 4.69 can

then be used to find $P(s)$ by eq. 4.68,

$$P(s) = -\frac{1}{s^*}\frac{dh(s/s^*)}{ds}\frac{d}{ds}\frac{s}{s^*} \tag{4.70}$$

$$= \frac{1}{s^{*2}}\left(-\frac{dh(s/s^*)}{ds}\right) \tag{4.71}$$

$$P(s) = s^{*-2}H(s/s^*), \tag{4.72}$$

where $H(s/s^*)$ contains a cutoff function so that $P(s) \to 0$ when $s/s^* \gg 1$. From eq. 4.72 we would expect a collapse of the non-wetting cluster size distributions, for the re scaling $s^{*2}P(s)$ vs. s/s^*. This is shown in figure 4.34. It is evident from the figure that the collapse is very good, apart from a crossover for the smallest clusters. It is not clear what causes this crossover, but for a large range of cluster sizes, we have found that the wetting fluid flow-rate Q_w controls the non-wetting cluster-size distribution,

$$P(s) \propto Q_w^2 H(sQ_w). \tag{4.73}$$

This result is interesting, because we are now able to predict the cluster size distribution for other values of Q_w, yet unexplored. However, at present time we cannot give a satisfactory physical explanation for this behavior of $P(s)$.

We postulated earlier that the length of the cutoff clusters were constant in the direction transverse to the flow and found that $s^* \propto Q_w^{-1}$. Recent discoveries indicate that the latter finding holds true, but the postulate itself seems a bit too hasty. To study how the lengths of each

Figure 4.35: *The porous matrix is shown, and the direction of flow is parallel to the y-axis. A bounding box is the smallest rectangle that can contain the cluster. During image analysis, a bounding box is fitted to each non-wetting cluster. The two sides of the rectangle, l_x and l_y is always oriented parallel to the x- and y-axis respectively. Note that l_y is parallel to the direction of flow.*
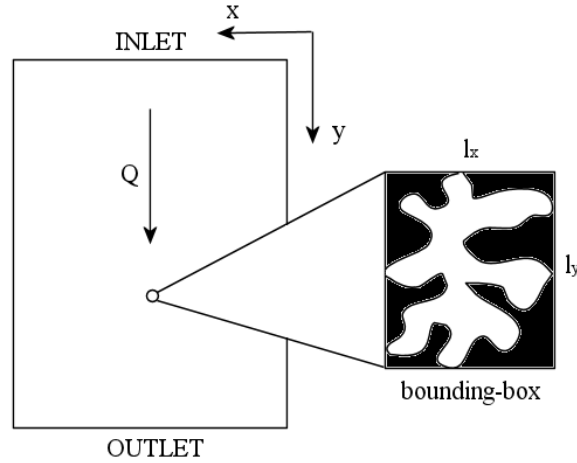
cluster, parallel and transverse to the direction of flow, was distributed we used the method of $bounding - boxes$. This method consists in fitting the smallest rectangle to each non-wetting cluster, as shown in figure 4.35. The routine is provided in Matlab and has been included in our image analysis script, found in appendix B.1. According to figure 4.35, we denote the box length in the y-direction as l_y and in the x-direction as l_x. All lengths l are given in number of pixels where,

$$[l] = \text{\#pixels} \tag{4.74}$$

$$1\text{pixel} = 0.193 \text{ mm} \tag{4.75}$$

The distribution $P(l_y)$ gives the probability density of a bounding box with length l_y in the y-direction, and similarly $P(l_x)$ gives the probability density of a bounding box with a length l_x in the x-direction. Figure 4.36 shows the distributions $P(l_y)$ and $P(l_x)$ in both directions for all Ca-numbers during steady-state. Note that the two first data points correspond to widths $l < 4$. This

is below the bead diameter $b = 6$, and hence gives strong restrictions on the cluster size. It is very unlikely that a cluster with a width $l_x < 4$ has a length more than a couple of bead diameters $l_y \leq 2b$. On the other hand, clusters must be above $s_{\min} = 25$, since clusters below this size are counted as beads and removed from the binary image before collecting the statistics. Visual observation suggests that these clusters originate from bursts. From the third data point and out, the distributions of figure 4.36 are actually very similar in shape to those shown in figure 4.31. Unfortunately one cannot say anything from this figure about how l_y and l_x are distributed for the cutoff clusters in particular, since clusters of all sizes have been included in the distributions. Figure 4.36 does however indicate that for all Ca-numbers and lengths $l > 15$, clusters are only slightly longer in the y-direction, compared to the x-direction. This implies that clusters can also extend considerably in the x-direction. Based on the similarity between the distributed lengths in both directions, it seems unreasonable for cutoff clusters to have a characteristic length scale $l_y^* \propto Q_w^{-1}$, while the corresponding length l_x^* should be constant and hence independent of Q_w. This is supported by the collapse of *both* $P(l_y)$ and $P(l_x)$ by the re scaling, $l_i^{*2} P(l_i)$ vs. l_i / l_i^* where,
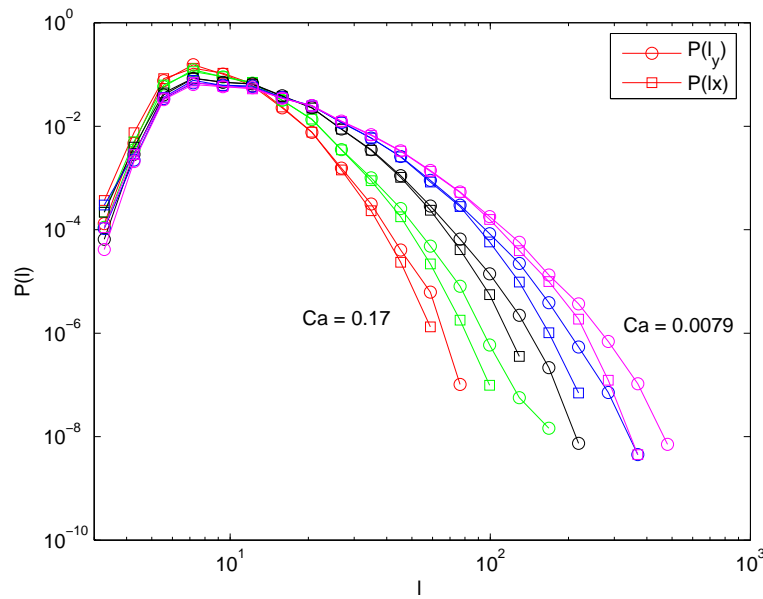
Figure 4.36: *Bounding box distributions $P(l_y)$ and $P(l_x)$ for all Ca-numbers during steady-state. We se that for lengths $l > 15$, clusters are slightly larger in the direction of flow, but the two distributions are otherwise very similar. The same behavior is found for all Ca-numbers. Besides the two data points for the lowest l-values, these distributions have the same shape as the cluster size distributions seen in figure 4.31.*

$$l_x^* \propto l_y^* \propto Q_w^{-\frac{1}{2}}. \tag{4.76}$$

Thus, the cutoff clusters are associated with characteristic length scales l_y^* and l_x^*, both inversely proportional to the square root of Q_w. The probability distributions can be written,

$$P(l_x) \propto Q_w G(l_x Q_w^{\frac{1}{2}}) \tag{4.77}$$

$$P(l_y) \propto Q_w G(l_y Q_w^{\frac{1}{2}}), \tag{4.78}$$

where $G(l_i Q_w^{\frac{1}{2}})$ contains a cutoff function so that $P(l_i) \to 0$ when $l_i Q_w^{\frac{1}{2}} \gg 1$. From eq. 4.76 we
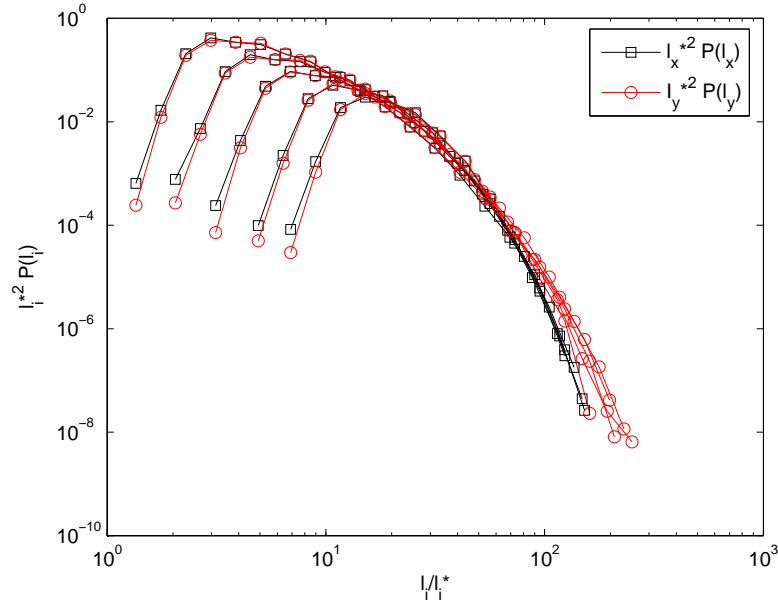
Figure 4.37: *Data collapse is obtained for all Ca-numbers for both $P(l_x)$ and $P(l_y)$ by the re scaling $l_i^{*2}P(l_i)$ vs. l_i/l_i^*. It is found that $l_i^* \propto Q_w^{-\frac{1}{2}}$. Note that there is a crossover for the smallest cluster lengths.*

find that,

$$s^* \propto l_x^* l_y^* \propto Q_w^{-1}. \tag{4.79}$$

The following explanation is proposed for the behavior of l_y^*, which is the cutoff length scale in the direction of flow. It was found in section 4.3.2 that the pressure difference over the model during steady state followed a power law of the form (eq. 4.17),

$$\Delta P_{ss} \propto Q_w^{\beta}, \tag{4.80}$$

where $\beta = 0.54 \pm 0.06$. Assuming a constant pressure gradient over the model, and $\beta = 1/2$ we get,

$$|\nabla P_{ss}| = \frac{\Delta P_{ss}}{L} \propto Q_w^{\frac{1}{2}}. \tag{4.81}$$

Instead of using the generalized Darcy law in eq. 4.62, to find the flow-rate dependence of the critical length scale, we use eq. 4.81,

$$l_y^* = \frac{\Delta P_{D,I}}{|\nabla P_{ss}|} \tag{4.82}$$

$$l_y^* \propto Q_w^{-\frac{1}{2}}. \tag{4.83}$$

This is consistent with the found scaling of $P(l_y)$. It is not clear why the same flow-rate dependence is found in l_x^*, transverse to the direction of flow. We will have to leave this discussion with some open questions, but our findings suggest further verification by a thorough analysis and additional experiments. The results presented above have been discovered very recently, and the time frame for this project has only permitted a mere presentation.

4.7   Simulation comparison

When studying flow in porous media, it can be very fruitful to compare experiments with numerical simulations. Experiments have the advantage of always reflecting reality, but it is not always possible to obtain reliable measurements of every property. In simulations on the other hand, everything is measurable, but what you measure need not always to reflect reality. If correspondence is found by comparison, the combination can give greater insight of the problem at hand.

We reviewed in section 2.5.4 that simultaneous steady-state flow has been studied numerically by Knudsen *et al.* [25] and Ramstad *et. al* [8]. A network model with biperiodic boundary conditions was used. This is best visualized as a mapping of the two-dimensional network onto the surface of a three-dimensional torus. In this way fluids flow in a continuous loop, so as to inflect the behavior deep inside a reservoir. Experimentally, these boundary conditions cannot be achieved. Instead, Ramstad [48] has recently modified the network simulator to mimic our boundary conditions. Wetting and non-wetting fluid are injected from every other inlet node. The corresponding outlet is the entire end-side of the network and has a fixed pressure equal to zero. Any fluid configuration that reaches the outlet is made "disappear", which in our case corresponds to fluid leaving the outlet and entering the reservoir. The network is considered to be embedded onto a cylinder surface, and thus have periodic boundary conditions in the direction normal to the flow.

The network consists of 128×128 nodes and has a physical size of 18×18 cm. Each node is the connecting point of four tubes, oriented at an angle $45°$ to the direction of flow. All of the fluid volumes are contained in the tubes. The randomness of a real porous medium is incorporated by assigning different tube lengths d_{ij} and radii r. The four lengths d_{ij} of each node is chosen randomly within 30% of the lattice constant $d = 2$mm, and the radii are chosen from a flat distribution $r \in (0.1d, 0.1d + 0.3d_{ij})$. With respect to the comparison, tube radii, which again govern the threshold pressures for drainage and imbibition, must be chosen so that it reflects the corresponding experimental distributions. This last point needs further work on our part. In the simulations, viscosity ratio, surface tension and flow-rates are selected according to the experimental values, and fluids are considered incompressible.

The simulations are ongoing, and reported to be somewhat time consuming due to the low viscosity ratio ($M \sim 10^{-4}$). At this stage only preliminary results exists. Figure 4.38 shows four snapshots during the invasion phase from simulations at $Q_w^{\mathrm{sim}} = 0.4$ ml/min, and the corresponding experiment at $Q_w = 0.44$ ml/min with Ca $= 0.015$. The simulation/experiment comparison of these snapshots are very promising. The characteristic mixing and fragmentation are evident. The initial channeling of both phases are broken up as the invasion progresses. It seems that the width of the front displays similarities in the two last snapshots. However, this may change at a later stage in the experiments, when bursts start to affect the dynamics. Due to incompressibility, bursts are not observed in the simulations. Figure 4.39 shows a comparison of the non-wetting cluster size distributions between the simulation and experiment described above. The displacement structure is at the last stages of invasion in the simulation, whereas steady-state has been reached in the experiment. The reason for the difference is simply that we do not have any data as of yet from steady state. However, the comparison reveals a cutoff in both cases, and the shape of the two distributions is also quite similar. This is promising with respect to further investigation of the scaling relations presented in section 4.6.2.

In addition to cluster size distributions, the effect of viscosity changes are of interest. This is of course much easier to study in simulations. Preliminary analysis of simulations indicate that the structure does not change significantly if the non-wetting viscosity is increased say by a factor of 100, giving a ratio $M \sim 10^{-2}$. Pressure development and the dependence on flow-rate should also be considered. We find experimentally that the pressure difference over the model during steady-state is a power-law in the wetting fluid flow-rate, with an exponent different from unity.

In section 4.5 we emphasized that the experimental determination of saturation was difficult. Three methods was used, all with some uncertainty, but consistency was found. Saturation is however easily determined in the simulations. By comparison we hope to confirm the found

experimental curve $S_{nw}(Q_w)$.
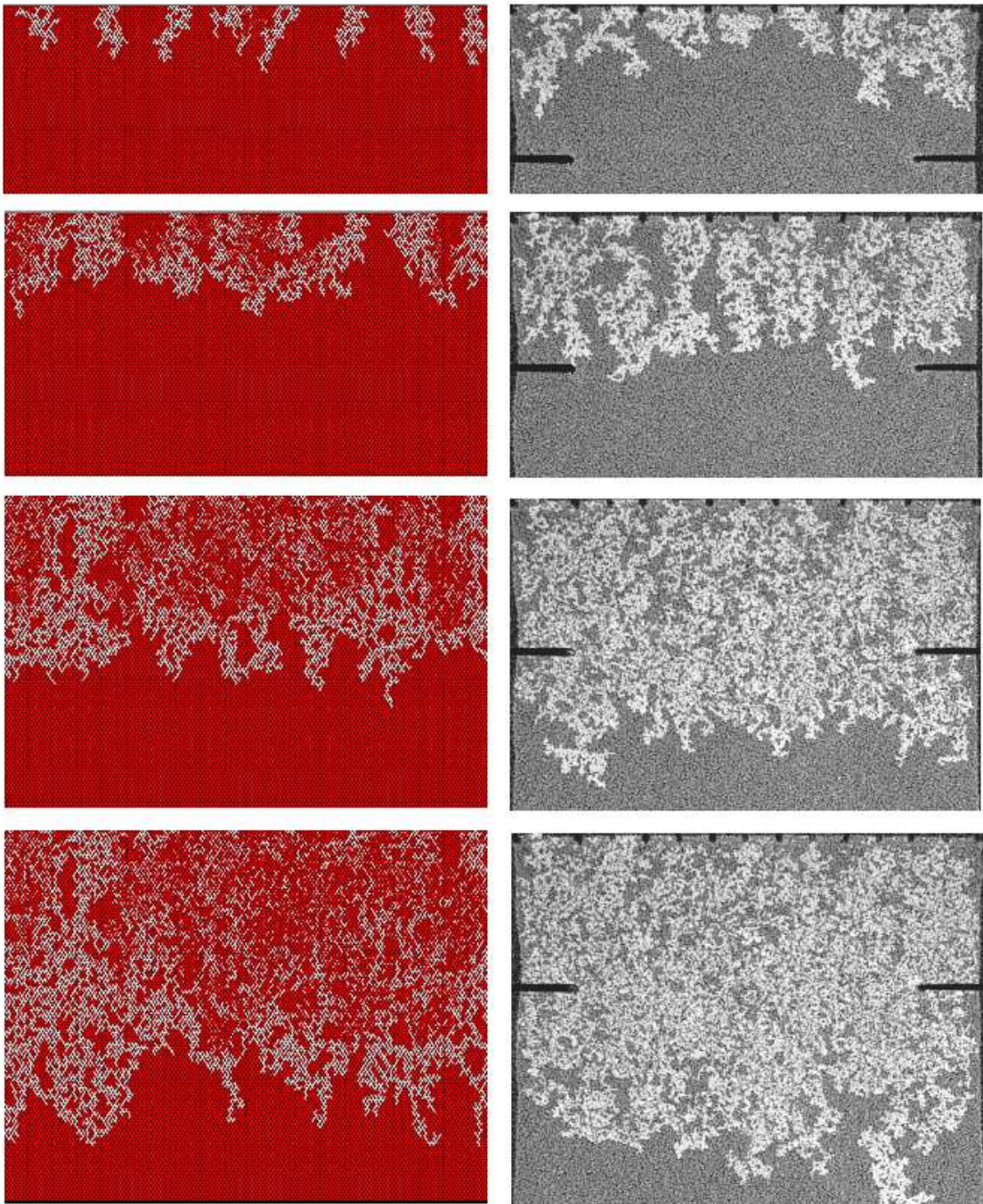
Figure 4.38: *Snapshots of the invasion phase during simultaneous flow, simulation (left column) and experiment (right column). The simulation is performed by Ramstad [48]. Wetting (red) and non-wetting (white) fluid are injected from every other inlet node. The total wetting fluid flow-rate is $Q_w^{sim} = 0.4$ ml/min. The simulation is compared to one of our experiments at wetting fluid flow-rate $Q_w = 0.44$ ml/min. The similarity in displacement structure is evident.*
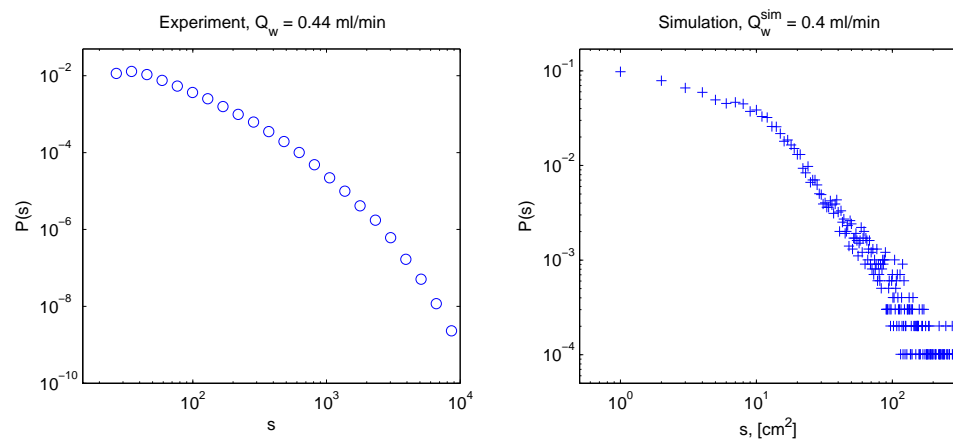
Figure 4.39: *Non-wetting cluster size distributions $P(s)$.* **Right:** *From simulation [48], $Q_w^{sim} = 0.4$ ml/min, during the last stages of the invasion phase. The cluster size is in units of cm². **Left:** From experiment, $Ca = 0.015$ and $Q_w = 0.44$ ml/min, during steady-state. The cluster size s is in pixel units. The two distributions should not be compared by the axis values. This comparison in included to show that the cutoff behavior is found both in experiments and simulations. Additionally the shape of the two distributions shows similarities.*

4.8   Concluding remarks

Simultaneous two-phase flow in porous media has been studied experimentally, in a large quasi two-dimensional laboratory model of roughly 214000 pores. Both the invasion phase and steady-state have been considered. Steady-state flow is a more realistic description of the situation deep inside natural reservoirs, than pure transient regimes.

In all experiments the combination of glycerol/water and air have been used as the pair of wetting and non-wetting fluid respectively. Analysis has been performed on the basis of digital imaging of displacement structures, pressure measurements and balance readings of produced output volume of wetting fluid. The improvement of the lightbox, used to illuminate the porous matrix, has been crucial in order to do a meaningful analysis of the imaged structure.

The observed displacement structure is utterly more complex than what is found in the transient regimes of capillary or viscous fingering. Due to the simultaneous flow of high viscous wetting fluid, clusters of low viscous non-wetting fluid will be snapped off from the inlet nodes. The competition of both drainage and imbibition causes fragmentation of the non-wetting fluid, and the dynamics are characterized by the movement and mixing of discreet non-wetting clusters in a background field of wetting fluid. Initially the fragmentation and mixing of fluids increases, but are seen to stabilize when the most advanced parts of the front has reached roughly halfway through the model. At this point the invasion structure consists of a heterogenous region at the front and a homogenous region further behind, similar to that of later steady-state. When the tuning parameter Q_w, was increased, we observed no drastic change in the dynamics, but the moving non-wetting clusters decreased in size. The wetting fluid was observed to percolate the model at all times, through an interchanging network of connected pathways.

The invasion structure reached breakthrough at a characteristic time t_b, and the system reached steady state at a later time t_{ss}. Both t_b and t_{ss} followed a power-law in Q_{tot}^{inv} with the same exponent $\alpha \approx 1$. For all experiments we found that the time difference between breakthrough and steady-state was 38% of the breakthrough time.

We have found that both the pressure difference, saturation and statistical properties in the homogenous region during invasion is very close to what is found in steady-state. This is an important result, because it shows similarities between a transient and steady regime, which is far from obvious. Additionally, since the flow-rate of air during invasion is lower than in steady-state, these similarities indicate that it is the flow-rate of the wetting fluid that governs the dynamics. This point should be verified by more experiments where the flow rates of both phases can be tuned independently.

The most pronounced effect of air compressibility, is the observed burst behavior. Through a high-speed camera we have been able to study some of these highly dynamic events. The width of the front is affected by bursts. Through open channels of air, connected for a short time over larger distances, compressed volume of air is transported to the front where it expands in regions saturated with wetting fluid. During steady-state, bursts progress all the way through the model, which cause a "short circuit" between the inlet and outlet pressure. We believe that a substantial amount of air volume is transported to the outlet during a burst. No extensive analysis of burst behavior was performed during this work, since it is a full study in its own respect.

For the pressure development, we find that the pressure difference over the model in steady-state is given by, $\Delta P_{ss} \propto Q_w^{\beta}$, where $\beta \approx 0.54$. The exponent β is different from unity, which is the predicted value by Darcy's law. $\beta \neq 1$ is consistent with the findings of Knudsen *et al.* [24] for steady-state simulations with $M = 1$.

The probability distribution of non-wetting clusters exhibits a cutoff in all stages of the experiments. No power-behavior is found, and the cutoff cluster size scales with the tuning parameter, $s^* \propto Q_w^{-1}$. Further, the characteristic length scale of s^* in the direction of flow, is found to scale as, $l_y^* \propto Q_w^{-\frac{1}{2}}$. This is consistent with the flow-rate dependence of the measured pressure difference during steady-state. From the behavior of s^* we were able to produce a data collapse of the probability distributions, $P(s) = Q_w^2 H(Q_w s)$. At present time we cannot give a satisfactory physical interpretation of this relation. Further investigation is warranted. Ramstad *et al.* [8] found for

$M = 1$, a critical saturation $S_c \approx 0.69$ for the non-wetting fluid to produce a spanning cluster. Below this value, the cluster size distributions were dominated by a cutoff. This is consistent with our experiments, since for the range of flow-rates used, $S_{nw}(Q_w) < S_c$. Experiments should be performed with the intension of exploring this critical value.

Appendix A

Probability distributions and logarithmic binning

A random variable X is said to be continuous if it is defined for any value between given limits. The probability that X lies in the interval $x < X < x + dx$, is given by,

$$\Pr(x < X < x + dx) = f_X(x)dx, \tag{A.1}$$

where $f_X(x)$ is called the *probability density function* (PDF) of the variable X. The PDF is also referred to as the probability distribution. The sum of probabilities of all possible outcomes should always equal unity. Hence the probability distribution must obey the normalization condition,

$$\int_{-\infty}^{\infty} f_X(x)dx = 1. \tag{A.2}$$

It is also customary to introduce the *cumulative probability function* of the random variable X,

$$F_X(x) = \Pr(X \leq x) = \int_{-\infty}^{x} f_X(x')dx', \tag{A.3}$$

This function gives the probability that the random variable $X \leq x$. From eq. A.3 it follows that,

$$f_X(x) = \frac{dF_X(x)}{dx}. \tag{A.4}$$

When a random variable is sampled N times in an experiment, we get a set of measurements,

$$S_X = \{X_1, X_2, X_3, ..., X_N\}. \tag{A.5}$$

The PDF is found from S_X, by normalizing each bin in the resulting histogram by the number of samples and the respective bin width,

$$f_X(x_i) = \frac{N_i}{N\Delta x_i}. \tag{A.6}$$

In eq. A.6 N_i is the number of samples in S_X that lies within the interval $[x_i, x_{i+1}]$. The width of each histogram bin is given by $\Delta x_i = x_{i+1} - x_i$. For discrete variables, the normalization condition becomes,

$$\sum_i f_X(x_i)\Delta x_i = \frac{1}{N}\sum_i N_i = 1. \tag{A.7}$$

In the calculation of most PDF's, the bin width Δx_i is constant. However, care should be taken if the range of S_X varies over several decades, and the counts N_i is expected to vary in an exponential manner. If all bins have a constant width, some will contain zero or only a few counts, whereas others may contain thousands. It is thus hard to obtain the full shape of the PDF without averaging the distributions from multiple sets $S_{X,i}$.

PDF's with the behavior described above have been encountered numerous times throughout this work, so we will devote some space to the description of how to calculate such functions. The method is called *logarithmic binning*. It is assumed in the following, that the PDF in question is a decreasing function of x. In logarithmic binning the bin sizes of the histogram Δx_i are increased exponentially,

$$x_i = c^i \tag{A.8}$$

$$\Delta x_i = c^{i+1} - c^i \tag{A.9}$$

$$\Delta x_i = c^i(c - 1), \tag{A.10}$$

where c is a suitable constant. In this way we get a better average, since the number of counts at large x_i will increase due to the wider bins. The PDF is then found from eq. A.6.

Another approach to logarithmic binning is to take the logarithm of all the measurements $S_{\log X}$, and calculate the logarithmic PDF,

$$f_{\log X}(\log x_i) = \frac{N_i}{N\Delta \log x_i}. \tag{A.11}$$

In this case $\Delta \log x_i$ is constant, which again implies that x_i varies exponentially in the form of eq. A.8. Note that $f_{\log X}(\log x_i) \neq f_X(x_i)$. Combining eq. A.6 and eq. A.11 gives,

$$f_X(x_i)\Delta x_i = f_{\log X}(\log x_i)\Delta \log x_i. \tag{A.12}$$

When we go to the continuous limit we find,

$$f_X(x)dx = f_{\log X}(\log x)d \log x \tag{A.13}$$

$$f_X(x) = f_{\log X}(\log x)\frac{d \log x}{dx} \tag{A.14}$$

$$f_X(x) = x^{-1}f_{\log X}(\log x). \tag{A.15}$$

A well known family of PDF's is the *power-law* distributions,

$$f_X(x) \propto x^\alpha, \tag{A.16}$$

where α is called the power-law exponent. If the cumulative distribution also follows a similar power law,

$$F_X(x) \propto x^\beta, \tag{A.17}$$

the exponents are related by eq. A.4 trough,

$$\beta = \alpha + 1. \tag{A.18}$$

Using eq. A.15-A.16 we get,

$$f_{\log X}(\log x) \propto x^{\alpha+1} = x^\beta, \tag{A.19}$$

thus the logarithmic PDF is proportional to the cumulative distribution function in this case.

Appendix B

Matlab scripts

Sections B.1-B.2 includes the most important Matlab scripts used during image analysis. The scripts are not thoroughly commented, but they should be possible to follow by the details given in the text. In sections B.3-B.4 the scripts for IP and DLA are listed. In all sections the main script is listed first, followed by various sub-functions.

B.1   Cluster analysis

The script `imanalysis.m` computes the steady-state time averaged:

- Cluster size distribution.

- Eccentricity distribution for each cluster size, of the best fitted ellipse.

- Orientation distribution for each cluster size, of the best fitted ellipse.

- Bounding box distribution for each cluster.

The sub function `clustremoval.m` removes clusters of a specified size and all clusters connected to the boarder. `clusterdist.m` computes distributions according to the specified binning. `logbins.m` generates a logarithmic binned histogram. `hist3d.m` generates a three-dimensional histogram with logarithmic binning along one axis.

imanalysis.m

```
1  clear clust eccen orient bbx bby satair satfluid;
2  clust = 0; eccen = 0; orient = 0; bbx = 0; bby =0;
3
4  mincluster = 25; connectivity = 4;
5
6
7  k=1; % Counting variable
8
9  in1 = input('Enter original image path: ','s');
10 in2 = input('Enter threshold level, [0−255]: ');
11 in3 = input('Enter image start number: ');
12 in5 = input('Enter image stop number: ');
13 in4 = [215,1705,1,3000];% New images high−res
14 % in4 = [221,1233,462,2298]; % Old images low−res
15
16 Lx=in4(2)−in4(1)+1; Ly=in4(4)−in4(3)+1;
17
```

```
18
19  for(n=in3:in5)
20      path = strcat(in1,'image0',int2str(n),'.tif');
21      org = imread(path,'tif');
22
23      org = org(in4(3):in4(4),in4(1):in4(2));
24      org = im2bw(org,gray(255),in2/255);
25
26  display(strcat('-= Now processing: ','image',int2str(n),'.tif',' =-'))
27
28      [org,num0,satair(n-in3+1)] = clustremoval(org,mincluster,connectivity,Lx,Ly);
29      [L1,num1] = bwlabel(org,connectivity);
30      stats = regionprops(L1,'Area','BoundingBox','Orientation','Eccentricity');
31
32      % Compute relevant image properties
33
34      sizes = [stats.Area];
35      [x,nsp] = clusterdist(num1,sizes,40,1.3);
36
37      eccentricity = [stats.Eccentricity];
38      [pose,edist] = hist3d([sizes;eccentricity]',40,1.3,1);
39
40      orientation = [stats.Orientation];
41      [poso,odist] = hist3d([sizes;orientation]',40,1.3,90);
42
43      tmp = [stats.BoundingBox];
44      xw = tmp(3:4:end);
45      yw = tmp(4:4:end);
46      [x,bbdisty]=clusterdist(length(yw),yw,40,1.3);
47      [x,bbdistx]=clusterdist(length(xw),xw,40,1.3);
48
49
50      % Save data for time averaging
51      if(k==1)
52          clust = [x',nsp'];
53          eccen = edist;
54          orient = odist;
55          bbx = bbdistx;
56          bby = bbdisty;
57          k=0;
58      else
59          clust = [clust,nsp'];
60          eccen = eccen+edist;
61          orient = orient+odist;
62          bbx = bbx+bbdistx;
63          bby = bby+bbdisty;
64      end
65
66  end
67
68  % Time average
69  if((in5-in3+1)>1)
70      mnsp = sum(clust(:,2:end)')./(in5-in3+1);
71  else
```

```
72      mnsp = nsp;
73  end
74
75  meccen= eccen./(in5−in3+1);
76  morient= orient./(in5−in3+1);
77  mbbx = bbx./(in5−in3+1);
78  mbby = bby./(in5−in3+1);
79
80  % Write to file
81
82  dlmwrite('f:\nsp.dat', [clust(:,1),mnsp'],'delimiter', '\t',...
83          'precision', '%.10f', 'newline', 'pc');
84  dlmwrite('f:\eccen.dat', [pose,meccen],'delimiter', '\t',...
85          'precision', '%.10f', 'newline', 'pc');
86  dlmwrite('f:\orient.dat', [poso,morient],'delimiter', '\t',...
87          'precision', '%.10f', 'newline', 'pc');
88  dlmwrite('f:\boundingb.dat', [x',mbbx',mbby'],'delimiter', '\t',...
89          'precision', '%.10f', 'newline', 'pc');
```

clustremoval.m

```
1   % Removes bead and boarder clusters and returns bw−image
2   % + number of clusters
3
4   function [L1,num0] = clustremoval(A0,mincluster,connectivity,Lx,Ly)
5
6   [L1,num0] = bwlabel(A0,connectivity);
7   stats = regionprops(L1,'Area','PixelList');
8
9   idx = find([stats.Area]>mincluster);
10  L1 = ismember(L1,idx);
11
12  % Grab labels of boarder clusters
13
14  k = 0;
15
16  for(y = [1,length(L1(:,1))])
17      for(x = 1:length(L1(1,:)))
18          if(L1(y,x)~=0)
19              k = k+1;
20              bind(k) = L1(y,x);
21          end
22      end
23  end
24
25
26  for(x = [1,length(L1(1,:))])
27      for(y = 1:length(L1(:,1)))
28          if(L1(y,x)~=0)
29              k = k+1;
30              bind(k) = L1(y,x);
31          end
32      end
33  end
```

```matlab
34
35  % Remove clusters
36  bind  = unique(bind);
37
38  for(n=1:length(bind))
39          ID=[stats(bind(n)).PixelList];
40      for(i=1:length(ID(:,1)))
41          L1(ID(i,2),ID(i,1))=0;
42      end
43  end
```

<div align="center">clusterdist.m</div>

```matlab
1   % Cluster distribution
2
3   function [x,nsp,dx] = clusterdist(num,A,npowers,baseint)
4
5   [H,x,dx] = logbins(A,npowers,baseint);
6   nsp = H(1:end−1)./(num.*dx);
```

<div align="center">logbins.m</div>

```matlab
1   % Logarithmic binning
2
3   function [H,x,dx] = logbins(histinput,npowerbin,logbinsize)
4
5   % Generating the bin vector
6   for i = 1:(npowerbin+1)
7       binlim(i) = logbinsize.^(i−1);
8   end
9
10  H = histc(histinput,binlim);
11
12  % Probability density
13  for i = 1:(length(H)−1)
14      % Center of each bin
15      x(i) = binlim(i)+(0.5.*(binlim(i+1)−binlim(i)));
16      % Length of each bin
17      dx(i) = binlim(i+1)−binlim(i);
18  end
```

<div align="center">hist3d.m</div>

```matlab
1   % 3D−logarithmic binning.
2
3   function [pos,edist] = hist3d(histinput,npowerbin,logbinsize,linlim)
4
5   for i = 1:(npowerbin+1)
6       binlim(i,1) = logbinsize.^(i−1);
7       binlim(i,2) = linlim.*(i−1)/(npowerbin);
8   end
9   edges{1} = binlim(:,1);
10  edges{2} = binlim(:,2);
11  [N,pos] = hist3(histinput, 'Edges', edges);
```

```
12
13 % Normalization factor of each bin
14 for i = 1:(length(N(:,1))-1)
15       % Length of each bin
16          dL(i,1) = binlim(i+1,1)-binlim(i,1);
17 end
18
19 dL(:,2) = binlim(2,2)-binlim(1,2);
20
21 for (i = 1:length(N(:,1))-1)
22     dA(i,1:length(N(:,1))-1) = dL(i,1).*dL(1,2);
23 end
24
25 % Calculate the distribution
26 edist = N(1:end-1,1:end-1)./(sum(sum(N(1:end-1,1:end-1))).*dA);
27
28 % x and y ticks
29 pos = [pos{2}(1:end-1);pos{1}(1:end-1)]';
```

B.2   Saturation analysis

The script `saturation.m` computes saturation from intensity and binary images, according to eq. 4.43 and eq. 4.50 in section 4.5. `negativebw.m` performs the binary transformation $0 \rightarrow 1$ and $1 \rightarrow 0$. `rtaverage.m` computes the running time average of the given input data and average constant. This is used to smooth noisy functions.

saturation.m

```
1 % This function computes saturation from binary images (satfluidbw),
2 % relative intensity difference (satfluid) and smoothed (satfluidmean)
3 % as a function of position. The global intensity (ssglobal) is also
4 % computed.
5
6 function [satfluidbw,satfluid,satfluidmean,ssglobal] = saturation
7
8 mincluster = 25;
9 connectivity = 4;
10
11 k=1; % Counting variable
12
13 in1 = input('Enter original image path: ','s');
14 in2 = input('Enter threshold level, [0-255]: ');
15 in3 = input('Enter image start number: ');
16 in4 = [215,1705,1,3000]; % New images high-res
17 % in4 = [221,1233,462,2298]; % Old images low-res
18 in5 = input('Enter image stop number: ');
19 in6 = input('Enter background image number: ','s');
20
21 Lx = in4(2)-in4(1)+1;
22 Ly = in4(4)-in4(3)+1;
23
24 step = 40; % Sets the length of the box in direction of flow
25
```

```matlab
26 % Reads the background image
27 back = imread(strcat(in1,'image000',in6,'.tif'),'tif');
28 back = back(in4(3):in4(4),in4(1):in4(2));
29
30 for(n = in3:in5)
31     if(n<10)
32         path = strcat(in1,'image','000',int2str(n),'.tif');
33     elseif(n<100)
34         path = strcat(in1,'image','00',int2str(n),'.tif');
35     elseif(n<1000)
36         path = strcat(in1,'image','0',int2str(n),'.tif');
37     else
38         path = strcat(in1,'image',int2str(n),'.tif');
39     end
40
41     org = imread(path,'tif');
42     org = org(in4(3):in4(4),in4(1):in4(2));
43
44
45 display(strcat('-= Now processing: ','image0',int2str(n),'.tif',' =-'))
46
47     % Global intensity
48     ssglobal(n-in3+1) = (sum(sum(org))-sum(sum(back)))./sum(sum(back));
49
50     % Intensity as a function of position
51     satfluid(n-in3+1,1) = (sum(sum(org(1:step,:))) -...
52         sum(sum(back(1:step,:)))))./sum(sum(back(1:step,:)));
53     i = 2;
54     for(j = step+1:step:Ly-step)
55         satfluid(n-in3+1,i) = (sum(sum(org(j:j+step,:))) -...
56             sum(sum(back(j:j+step,:)))))./sum(sum(back(j:j+step,:)));
57         i=i+1;
58     end
59     satfluid(n-in3+1,i) = (sum(sum(org(Ly-step:Ly,:))) -...
60         sum(sum(back(Ly-step:Ly,:)))))./sum(sum(back(Ly-step:Ly,:)));
61
62
63     % Smoothing (running time average) of saturation values
64     satfluidmean(n-in3+1,:) = rtaverage(satfluid(n-in3+1,:),10);
65
66
67     % Saturation from binary images.
68
69     % negativebw performs the 0's->1's and 1's->0's transformation.
70     neg = negativebw(im2bw(org,gray(255),in2/255));
71     satfluidbw(n-in3+1) = sum(sum(neg))./(Ly.*Lx*0.63);
72     clear org;
73 end
```

---

negativebw.m

```matlab
1 % Performs the 0's->1's and 1's->0's transformation
2 % in a binary matrix.
3
```

```
4  function  [IM]  =  negativebw (IM)
5
6  Ly  =  length (IM( : , 1 ) ) ;
7  Lx  =  length (IM( 1 , : ) ) ;
8
9  for ( i  =  1:Ly )
10       for ( j  =  1:Lx )
11           if (IM( i , j )==1)
12               IM( i , j )=0;
13           else
14               IM( i , j )=1;
15           end
16       end
17  end
```

rtaverage.m

```
1  % Running  time  average ,  input  [ data  vector ,  tau ]
2
3  function  T  =  rtaverage (R, tau )
4  kmax  =  length (R)−tau ;
5
6  for  k  =  1:kmax
7      T( k )  =  sum (R( k : ( k+tau ) ) ) . / ( tau +1);
8  end
```

B.3   The invasion percolation algorithm, IP

The IP algorithm of section 2.4.2 is implemented in the main script `invperc.m`. The sub function `front.m` tests if the input site belongs to the invasion front.

invperc.m

```
1  % Invasion  percolation  with  trapping
2
3  clear  all
4
5  global  Lx ;
6  global  Ly ;
7  Lx  =  40;   % Defines  the  size  of  the  lattice .
8  Ly  =  80+1;
9
10  pt  =  rand (Ly , Lx ) ; % Underlaying  probability  matrix  of
11                   % the  lattice  (IM) ,  dim: Ly  x  Lx .
12  global  IM;
13
14  IM  =  ones (Ly , Lx ) . ∗ 2; % Initialization  of  the  lattice
15                   % IM( i , j )=2
16  t =1;
17  tend  =  1; % Number  of  " time−steps " .
18  k  =  1; % Counting  index  for  front  propagation .
19  q  =  1; % Counting  index  for  image  writing .
20
```

```
21 % Initial step. The invader starts from a "point" or a channel
22
23 % IM(Ly,50)=1; % Point IP
24 IM(Ly,1:Lx)=1; % Channel IP
25
26 % Finds the indices of the largest element in a given row in pt,
27 % and invades (=1) the corresponding element in IM
28 IM(Ly−1,find(pt(Ly−1,1:Lx)==max(pt(Ly−1,1:Lx)))) = 1;
29
30 while tend==1
31
32     if max(IM(2,1:end))==1
33         break
34     end
35
36     % Check if there are trapped clusters
37     IM=bwlabel(IM−1,4); % Labels defending clusters, by setting
38                         % invader sites = 0.
39     IM=IM+1; % Keeps the labeling, and puts the invader sites = 1.
40
41 for i = 1:Ly
42     s = sort(IM(i,1:end)); % Sorts the i'th row in ascending order.
43     if s(1)==1 % Tests if the i'th row contains an invader site.
44         for j = 1:Lx
45             bin = front(i−1,j); % If the i'th row contains an invader site,
46                                 % all the elements in the (i−1)'th row are
47                                 % being tested in the function front.m to
48                                 % see if they are part of the front.
49             if bin==1
50                 % pfront is the front matrix where the first column
51                 % contains the probability and the second and third
52                 % columns contain the corresponding indices for this front
53                 % site.
54                 pfront(k,1) = pt(i−1,j);  % Probability.
55                 pfront(k,2) = i−1;        % y−coordinate.
56                 pfront(k,3) = j;          % x−coordinate.
57                 k = k+1;
58             end
59         end
60     end
61 end
62
63 % Finds the row−index of the largest probability in pfront,
64 % and invades (=1) the corresponding element in IM
65 e = find(pfront(1:end,1)==max(pfront(1:end,1)));
66 IM(pfront(e,2),pfront(e,3)) = 1;
67 clear pfront
68 k = 1;
69
70 % Put invader sites = 1, and defending sites = 0.
71 for i = 1:Ly
72     for j = 1:Lx
73         if IM(i,j)~=1
74             IM(i,j)=0;
```

```
75              end
76          end
77  end
78
79  % The following lines saves the image for each iteration.
80  if ((t/100)==q)
81      pic = label2rgb(IM(2:end,1:end));
82      number = int2str(q);
83      picloc = strcat('f:\',number,'.tif');
84      imwrite(pic,picloc,'tif');
85      q = q+1
86  end
87  t = t+1
88  end
```

<div align="center">front.m</div>

```
1   % Returns bin = 1 if the site is part of the front,
2   % otherwise bin = 0.
3
4   function [bin] = front(a,b)
5
6   global IM
7   global Lx
8   global Ly
9
10  % The site is part of the front if one of the neighboring sites
11  % is an invader.
12  if IM(a,b)~=IM(1,1) % Takes trapped clusters into account. If the site
13                      % tested is not part of the large defending cluster it
14                      % should not be counted as a front site.
15      bin=0;
16  elseif (b+1)==(Lx+1)
17      if (IM(a+1,b)==1)||(IM(a-1,b)==1)||(IM(a,b-1)==1)
18          bin = 1;
19      else
20          bin = 0;
21      end
22  elseif (b-1)==(1-1)
23      if (IM(a+1,b)==1)||(IM(a-1,b)==1)||(IM(a,b+1)==1)
24          bin = 1;
25      else
26          bin = 0;
27      end
28  elseif (a+1)==(Ly+1)
29      if (IM(a-1,b)==1)||(IM(a,b+1)==1)||(IM(a,b-1)==1)
30          bin = 1;
31      else
32          bin = 0;
33      end
34  elseif (a-1)==(1-1)
35      if (IM(a+1,b)==1)||(IM(a,b+1)==1)||(IM(a,b-1)==1)
36          bin = 1;
37      else
```

```matlab
38           bin = 0;
39       end
40  else
41       if (IM(a+1,b)==1)||(IM(a-1,b)==1)||(IM(a,b+1)==1)||(IM(a,b-1)==1)
42           bin = 1;
43       else
44           bin = 0;
45       end
46  end
```

B.4   Diffusion limited aggregation, DLA

The DLA algorithm of section 2.4.3 is implemented in the main script difflimagg.m. The sub
function dlafront.m tests if the random walker neighbors an invaded site. randomwalk.m per-
forms one step in a random walk.

difflimagg.m

```matlab
1  % DLA algorithm, brute force
2
3  global Lx
4  global Ly
5  Lx=400;
6  Ly=800;
7
8  global i
9  global j
10 global DLA
11 DLA=zeros(Ly,Lx);
12 DLA(Ly,Lx/2)=1; % Plants the seed.
13
14 tstart=1;
15 tend=160000; % Number of timesteps.
16
17 for(t = tstart:tend)
18     t % Displays the VERY slow progression.
19
20     % Draw a random site along the top line.
21     startv = [0,rand(1,Lx-2),0];
22     start = find(startv==max(startv));
23     i = 1;
24     j = start;
25
26     % Performs one step in a random walk.
27     randomwalk;
28
29     if (j+1)==(Lx+1)||(j-1)== 0
30         if (j+1)==(Lx+1)
31                 j=j-1;
32         else
33                 j=j+1;
34         end
35     end
```

```
36
37      % If the random walker neighbors an invaded site
38      % it sticks.
39      if dlafront==1
40          DLA(i,j)=1;
41          break;
42      end
43
44      % The following lines saves the image if t is a
45      % multiple of 100.
46      if ((t/100)==q)
47          pic = DLA;
48          number = int2str(t);
49          picloc = strcat('~kentt/Master/DLA400by800/',number,'.tif')
50          imwrite(pic,picloc,'tif');
51          q = q+1;
52      end
53 end
```

---

dlafront.m

```
1  % DLA–front: Tests if the walker neighbors an invaded site.
2
3  function [bin] = dlafront
4
5  global DLA
6  global Lx
7  global Ly
8  global i
9  global j
10
11 if (i==Ly&&j==Lx/2)
12     bin = 1;
13 elseif (i-1)==0&&(j-1)==0
14     if (DLA(i+1,j)==1)||(DLA(i,j+1)==1)
15         bin = 1;
16     else
17         bin = 0;
18     end
19 elseif (i-1)==0&&(j+1)==(Lx+1)
20     if (DLA(i+1,j)==1)||(DLA(i,j-1)==1)
21         bin = 1;
22     else
23         bin = 0;
24     end
25 elseif (j-1)==(1-1)
26     if ((DLA(i+1,j)==1)||(DLA(i-1,j)==1)||(DLA(i,j+1)==1))
27         bin = 1;
28     else
29         bin = 0;
30     end
31 elseif (j+1)==(Lx+1)
32     if (DLA(i+1,j)==1)||(DLA(i-1,j)==1)||(DLA(i,j-1)==1)
33         bin = 1;
```

```matlab
34      else
35          bin = 0;
36      end
37  elseif (i-1)==(1-1)
38      if ((DLA(i+1,j)==1)||(DLA(i,j-1)==1)||(DLA(i,j+1)==1))
39          bin = 1;
40      else
41          bin = 0;
42      end
43  elseif (i+1)==(Ly+1)
44      if (DLA(i-1,j)==1)||(DLA(i,j+1)==1)||(DLA(i,j-1)==1)
45          bin = 1;
46      else
47          bin = 0;
48      end
49  else
50      if (DLA(i+1,j)==1)||(DLA(i-1,j)==1)||(DLA(i,j+1)==1)||(DLA(i,j-1)==1)
51          bin = 1;
52      else
53          bin = 0;
54      end
55  end
```

randomwalk.m

```matlab
1  % The random walker. ("A drunkards walk" - T.E)
2
3  function randomwalk
4
5  global i
6  global j
7  global Ly
8
9  h = rand;
10
11 if i==1
12     if h>=(0/3)&&h<(1/3)
13         i = i+1;
14     elseif h>=(1/3)&&h<(2/3)
15         j = j+1;
16     else
17         j = j-1;
18     end
19
20 elseif i==Ly
21     if h>=(0/3)&&h<(1/3)
22         i = i-1;
23     elseif h>=(1/3)&&h<(2/3)
24         j = j+1;
25     else
26         j = j-1;
27     end
28
29 else
```

```
30      if h>=(0/4)&&h<(1/4)
31          i = i+1;
32      elseif h>=(1/4)&&h<(2/4)
33          i = i-1;
34      elseif h>=(2/4)&&h<(3/4)
35          j = j+1;
36      else
37          j = j-1;
38      end
39 end
```

Bibliography

[1] K. J. Måløy, J. Feder and T. Jøssang (1985), *Viscous Fingering Fractals in Porous Media*, Phys. Rev. Lett, **55** 2688.

[2] L. Furuberg, K. J. Måløy and J. Feder (1995), *Intermittent behavior in slow drainage*, Phys. Rev. E, **53** 966.

[3] O. I. Frette, K. J. Måløy and J. Schmittbuhl (1997), *Immiscible displacement of viscosity-matched fluids in two-dimensional porous media*, Phys. Rev. E, **55** 2969.

[4] Y. Méheust, G. Løvoll, K. J. Måløy and J. Schmittbuhl (2002) *Interface scaling in a two-dimensional porous medium under combined viscous, gravity, and capillary effects*, Phys. Rev. E, **66** 051603.

[5] V. Frette (1993), *Visualization and analysis of two-phase flows in 3-D porous media.*, Dr.Scient thesis Dept. of Physics University of Oslo.

[6] O. I. Frette (1995), *Immiscible displacements in 2d porous media with a viscosity contrast equal to 1*, Cand. Scient thesis Dept. of Physics University of Oslo.

[7] D. Pnueli and C. Gutfinger (1992), *Fluid mechanics*.

[8] T. Ramstad and A. Hansen (2006), *Cluster evolution in steady-state two-phase flow in porous media*, Phys. Rev. E, **73** 026306.

[9] P. van Meurs and C. van der Poel (1958), Trans. Am. Inst. Min. Metall. Pet. Eng. **213** 103.

[10] V. Frette, K. J. Måløy, F. Boger, J. Feder, T. Jøssang and P. Meakin (1990), *Diffusion-limited-aggregation-like displacement structures in a three-dimensional porous medium*, Phys. Rev. A, **42** 3432.

[11] Pixelink (2004), *PL-A780 FireWire 6.6 MegaPixel Camera SYSTEM GUIDE*, `http://www.pixelink.com/support_downloads.asp?pID=39`, **Doucment No:** 04646-01.

[12] R. M. Haralick and L. G. Shapiro (1992), *Computer and Robot Vision, Volume I*, Addison-Wesley, 28-48.

[13] F. A. L. Dullien (1991), *Porous Media, Fluid Transport and Pore Structure, 2nd Edition*, 119-121.

[14] D. F. Young, B. R. Munson and T. H. Okiishi (1997), *A Brief Introduction to Fluid Mechanics*.

[15] W. A. Adamson (1982), *Physical chemistry of surfaces*, John Wiley and Sons, New York.

[16] J. Feder (1995), *Flow in porous media*, Lecture notes.

[17] D. G. Avraam and A. C. Payatakes (1995), *Flow regimes and relative permeabilities during steady-state two-phase flow in porous media*, J. Fluid Mech., **293** 207-236.

[18] D. G. Avraam, G. B. Kolonis, T. C. Roumeliotis, G. N. Constantinides and A. C. Payatakes (1994), *Steady-state two-phase flow through planar and nonplanar model porous media*, Transport in Porous Media, **16** 75-101.

[19] L. D. Landau & E. M. Lifshitz (1987), *Fluid Mechanics, 2nd Edition*, 45.

[20] A. E. Scheidegger (1974), *The physics of flow through porous media, Third Edition*, University of Toronto Press.

[21] C. M. Marle (1981), *Multiphase Flow in Porous Media*, Graham & Trotman Ltd.

[22] A. De Ville (1995), *On the Properties of Compressible Gas Flow in a Porous Media*, Transport in Porous Media, **22** 287-306.

[23] G. Løvoll, Y. Meheust, R. Toussaint, J. Schmittbuhl & K. J. Måløy (2004), *Growth activity during fingering in a porous Hele-Shaw cell*, Phys. Rev. E, **70** 026301.

[24] H. A. Knudsen & A. Hansen (2002), *Relation between pressure and fractional flow in two-phase flow in porous media*, Phys. Rev. E, **65** 056310.

[25] H. A. Knudsen (2002), *A numerical study of steady-state two-phase flow in porous media*, Dr. Ing. thesis Dept. of Physics, NTNU.

[26] A. C. Payatakes & M. Dias (1984), *Immiscible Microdisplacement and Ganglion Dynamics in Porous Media*, Reviews in Chemical Engineering, **2** 93-116.

[27] R. Lenormand, C. Zarcone & A. Sarr (1983), *Mechanisms of the displacement of one fluid by another in a network of capillary ducts*, J. Fluid. Mech., **135** 337-353.

[28] D. Wilkinson & J. F. Willemsen (1983), *Invasion percolation: A new form of percolation theory*, J. Phys. A, **16** 3365-3376.

[29] K. J. Måløy, L. Furuberg, J. Feder & T. Jøssang (1991), *Dynamics of Slow Drainage in Porous Media*, Phys. Rev. Lett., **68** 2161-2164.

[30] P. G. Saffman & G. Taylor (1958), *The penetration of a fluid into a medium of Hele-Shaw cell containing a more viscous liquid*, Proc. Soc. London, **245** 312-329.

[31] L. Paterson (1984), *Diffusion-limited Aggregation and Two-fluid Displacements in Porous Media*, Phys. Rev. Lett., **52** 1621-1624.

[32] J. Feder (1988), *Fractals*, Plenum Press, New York.

[33] R. Lenormand, E. Touboul & C. Zarcone (1988), *Numerical models and experiments on immiscible displacements in porous media*, J. Fluid. Mech., **189** 165-187.

[34] H. Auradou, K. J. Måløy, J. Schmittbuhl, A. Hansen & D. Bideau (1999), *Competition between correlated buoyancy and uncorrelated capillary effects during drainage*, Phys. Rev. E, **60** 7224-7234.

[35] R. Lenormand & C. Zarcone (1985), *Invasion percolation in an etched network: Measurment of a fractal dimension*, Phys. Rev. Lett., **54** 2226-2229.

[36] A. Vedvik, G. Wagner, U. Oxaal, J. Feder, P. Meakin & T. Jøssang (1997), *Fragmentation Transition for Invasion Percolation in Hydraulic Gradients*, Phys. Rev. Lett., **80** 3065-3068.

[37] E. Aker (1996), *A Simulation Model for Two-Phase Flow in Porous Media*, Cand.Scient thesis Dept. of Physics University of Oslo.

[38] G. N. Constantinides & A. C. Payatakes (1996), *Network Simulation of Steady-State Two-Phase Flow in Consolidated Porous Media*, AIChE Journal, **42** 369-382.

[39] H. Auradou, K. J. Måløy, J. Schmittbuhl & A. Hansen (2001), *Drainage in a Rough Gouge-Filled Fracture*, Transport in Porous Media, **50** 267-305.

[40] M. Cieplak & M. O. Robbins (1988), *Dynamical Transition in Quasistatic Fluid Invasion in Porous Media*, Phys. Rev. Lett., **60** 2042-2045.

[41] M. Cieplak & M. O. Robbins (1989), *Influence of contact angle on quasistatic fluid invasion of porous media*, Phys. Rev. B, **41** 11508-11521.

[42] M. Cieplak & M. O. Robbins (1991), *Fluid wetting properties and the invasion of square networks*, Phys. Rev. B, **45** 7762-7767.

[43] J. Schmittbuhl, A. Hansen, H. Auradou & K. J. Måløy (1999), *Geometry and dynamics of invasion percolation with correlated buoyancy*, Phys. Rev. E, **61** 3985-3995.

[44] K. M. Ng & A. C. Payatakes (1980), *Stochastic Simulation of the Motion, Breakup and Stranding of Oil Ganglia in Water-Wet Granular Porous Media During Immiscible Displacement*, AIChE Journal, **26** 419-429.

[45] E. Aker, K. J. Måløy, A. Hansen, G. G. Batrouni (1998), *A two-dimensional network simulator for two-phase flow in porous media*, Transport in Porous Media, **32** 163-186.

[46] The Engineering Tool Box (2002), *Air Properies*, `http://www.engineeringtoolbox.com/air-properties-d_156.html`

[47] D. Stauffer & A. Aharony (1994), *Introduction to Percolation Theory*, CRC Press.

[48] T. Ramstad (2007), *Simulation results for mixed flow model*, (unpublished).

[49] K. T. Tallakstad (2007), *LabVIEW instrumentation package*, `http://folk.uio.no/kentt/instrumentation.zip`